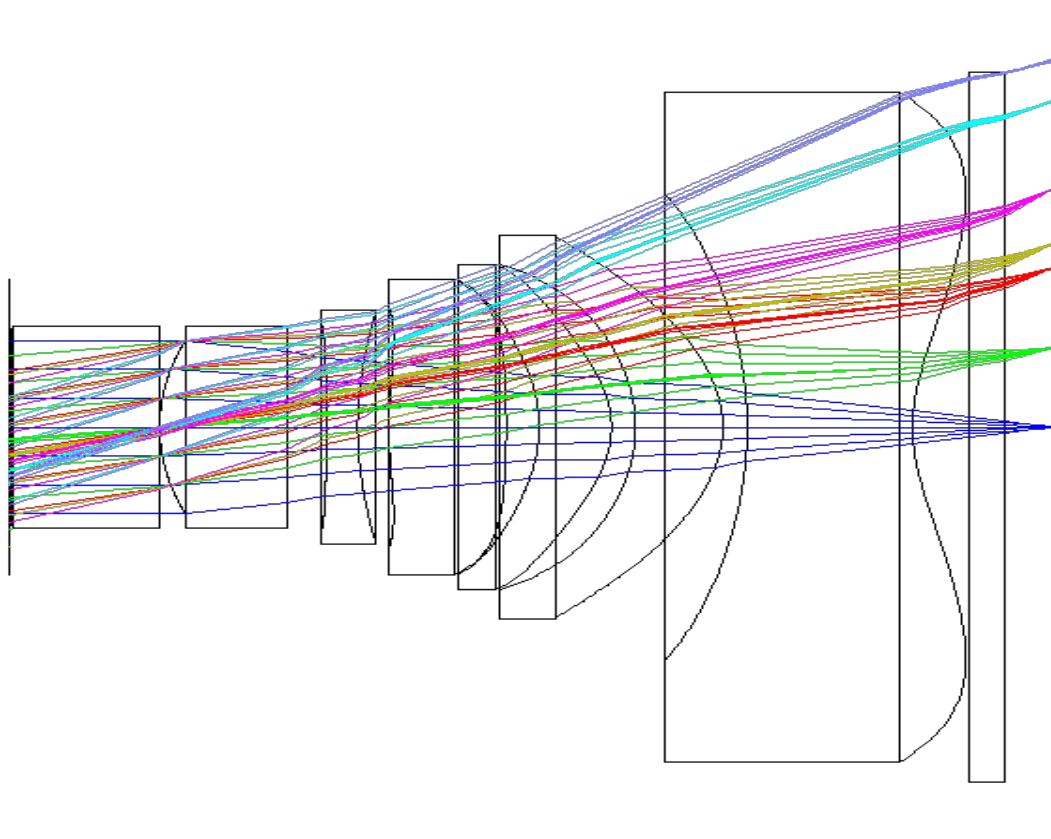


Mahmoud Ahmed Farghaly Abdelmeguid

Modeling and design of piezoelectrically actuated MEMS tunable lenses





Mahmoud Ahmed Farghaly Abdelmeguid

**Modeling and design of piezoelectrically
actuated MEMS tunable lenses**

A PhD dissertation in
Applied micro- and nanosystems

© Mahmoud Ahmed Farghaly Abdelmeguid, 2020

Faculty of Technology, Natural Sciences and Maritime Studies
University of South-Eastern Norway
Horten, 2020

Doctoral dissertations at the University of South-Eastern Norway no. 76

ISSN: 2535-5244 (print)

ISSN: 2535-5252 (online)

ISBN 978-82-7860-447-2 (print)

ISBN 978-82-7860-443-4 (online)



This publication is licensed with a Creative Commons license. You may copy and redistribute the material in any medium or format. You must give appropriate credit, provide a link to the license, and indicate if changes were made. Complete license

terms at <https://creativecommons.org/licenses/by-nc-sa/4.0/deed.en>

Print: University of South-Eastern Norway

The PhD thesis of Mahmoud A. Farghaly titled as "**Modeling and design of piezoelectrically actuated MEMS tunable lenses**" is approved by

Einar Halvorsen

Professor, HSN

Muhammad Nadeem Akram

Professor, HSN

To
My Family

Preface

This PhD thesis tackles the problem of designing piezoelectrically actuated MEMS tunable lenses using energy principles. Throughout the thesis, different models are proposed to reach decent accuracies for both the electromechanical and optical performances. The proposed models are progressive in their complexity. First, the linear regime has been considered and then the nonlinear regime. Based on the gained understanding of the models, design insights become obvious and have been used to push further more than the current design.

This PhD thesis has been conducted as a part of the project '*beat the human eye*' under the (Grant no. 235210) from the Research Council of Norway (Norges forskningsr rdet). In addition, a part of the numerical calculations have been performed as a part of (Grant no. NN9344K) from the Norwegian Metacenter for High Performance Computing (NOTUR). The thesis models the Piezoelectrically actuated MEMS tunable lenses through having numerical models implemented in MATLAB to calculate the lens performance with low number of degrees-of-freedom and in less time when compared to FEM programs. This effectively reduces, for lens-system designers, the overall time needed to simulate the lens in an optimization scheme when considering large combinations of material parameters and residual stresses in different layers. As an example with one variables combination, a static simulation in FEM for the lens takes 1.5 min and a dynamic analysis takes roughly 1 hour. Then, the displacement profiles are to be numer-

ically processed and exported in a form suitable for an optical program (Zemax) to simulate the lens or combine it with a fixed-focal-length lens system. The proposed models are proven to reduce the time to 1.3 seconds for static simulations and roughly few minutes for dynamic simulations. Implementing the models in MATLAB eases calling Zemax through a Dynamic Data Exchange (DDE) and automate the whole simulation chain. Moreover, if the the variational formulation is modified as needed, the proposed models have the potential to model other piezoelectric actuators such as pumps.

Finally, a notification for the readers is that this thesis directly dives into addressing the search problem and proposing solutions. Thus, the readers are expected to be familiar with basics of piezoelectric materials and frequency analysis of optical systems. If not, I recommend the readers to refer to chapters (4, 5 and 10) from [1] and chapters 1-6 from [2].

Acknowledgments

All thanks to Allah the Almighty that the presented work in this thesis has turned into reality. My sincere gratitude goes to everyone who has supported me during this journey.

I would like to express my sincere thanks for my supervisors Prof. Einar Halvorsen and Prof. Muhammad Nadeem Akram on their relentless guidance and support throughout my PhD study. I am deeply indebted to them for their supervision, patience and our weekly fruitful technical discussions. I would like to thank Prof. Ulrik Hanke as well for our discussion on the reduced-order models, and my fellow PhD researcher Cuong Hung Nguyen on our fruitful discussion. As well, I would like to thank Vladimir Kartashov from PoLight AS on supplying me with the experimental measurement used in verifying the nonlinear model.

A note of thanks dedicated to the University of South-Eastern Norway (HSN, previously HBV) for offering me this generous research fellowship under which this research work has been conducted. Sincere thanks also goes to the administration of the department of Microsystems at USN.

Last but not least, I thank PoLight AS's team for the scientific discussion and continuous support in our meetings throughout the project.

Abstract

Autofocus is a crucial feature in cameras, especially when photographing objects at different distances and having them in sharp focus without any quality loss in the captured image. Over the last decade, several research efforts have been made to incorporate tunable focus for mobile-device cameras using micro-scale components. Qualitatively, this would enable miniaturized cameras with lower power consumption, much faster response in scanning focus range and higher reliability. The microelectromechanical-systems-(MEMS)-based tunable focus lenses are promising alternatives as autofocus mechanisms when compared to the conventional macro-scale approaches such as the Voice Coil Motor (VCM) [3] or ultrasonic motor [4]. Moreover, such MEMS autofocus lenses would achieve higher resolution smartphone cameras without having any moving parts within the camera housing, which consumes power during focus adjustment and causes a loss in the Field-of-View (FoV) as for the VCM.

The research reported in this thesis is to construct a modeling framework for the piezoelectrically actuated MEMS tunable lenses on the electromechanical domain by finding an approximation for the lens displacement, and using it afterwards in the optical domain to find the lens' optical performance. Given the modeling framework, two design concepts have been proposed. The first one is to achieve larger lens apertures while having a tradeoff between focal length and RMS-wavefront error (RMSWFE), while the second is to increase lens' tunable

range of focal lengths by controlling layers' stresses during fabrication.

To approximate the lens displacement, we have used Hamilton's principle to deduce a variational formulation that can be easily solved in MATLAB [5]. This has resulted in taking less calculation time than the time is taken by finite element method (FEM) programs such as COMSOL [6]. The proposed displacement ansatz (weighted Gegenbauer polynomials) to approximate the lens displacement, has been chosen because they can be mathematically expressed in terms of Zernike polynomials. Those polynomials are suitable for representing the lens' wavefront when it comes to optical performance, which allows an exact mapping of the lens displacement profile to optical programs (*e.g.* Zemax [7]). Without this proposed framework, lens designers would have to use FEM simulations and over-mesh the pupil area before exporting the lens sag to optical programs; which is time-consuming with dense meshing.

Less calculation time, with our modeling framework, for the lens displacement originates from the pre-calculations of (linear and nonlinear) variational integrals in terms of the actuator's geometrical parameters. This has enabled storing mathematical expressions for the variational integrals that can be called once needed. For a new actuator's geometrical parameter, we can use a simple substitution to calculate the new displacement profile.

Chapter 3 describes the proposed modeling framework for these type of lenses. We have considered different polygonal pupil geometries to explore if a design tradeoff can be gained in the optical performance. We have found out the first design concept called as *pupil masking*. With a 45-rotated square opening in the piezoelectric actuator, while keeping the lens pupil circular, it gives a tradeoff between the lens' optical parameters, *e.g.*, lower RMSWFE at the expense of having larger focal length f allowing having large lens apertures.

The proposed modeling framework (in Ch. 3) has a weakness that it has not

accounted for the discontinuity of the lens layered structure around the pupil boundary. This required an increase of the model's degrees of freedom upto 120 in order to converge to a solution with a decent accuracy. Thus, in chapter 4, we have proposed having two new ansätze that use the aforementioned weighted Gegenbauer polynomials and, in addition, the exact solutions of the circular plate's differential equations. This has improved the speed of convergence to a solution and enabled having reduced-order models, which provide system-level designers with computationally efficient models. Yet, the new ansätze can be mapped to Zernike polynomials as well.

Chapters 3 and 4 have dealt with the linear performance that is less accurate in case of large actuation voltages. The linear model also neglects residual stresses resulting from fabrication. Thus, we have proposed in chapter 5, to use von Kármán's plate theory instead of Kirchhoff theory. As a result, we have been able to consider the effect of having different residual stresses within the lens' layered structure and larger actuation voltages. Through the understanding of the model parameters, we have been able to propose the second design concept. By controlling the residual stresses during fabrication, the lens' tunable range of focal lengths can be increased by having the lens operating, depending on the driving voltage, as a plano-convex or a plano-concave lens.

The proposed modeling frameworks have been verified versus FEM simulation as a reference point and moreover the nonlinear model has been verified versus measurements as well. In practice, these developed models can be utilized for optimization of different material choices and layers thicknesses to find the optimum geometrical parameter of the piezoelectric actuator. Finally, we provide conclusions and proposals for future work to build a dynamic model for the lens.

List of papers

Papers omitted from online publication due to publisher's regulations

Article 1

Mahmoud A. Farghaly, Muhammad Nadeem Akram, and Einar Halvorsen, "Modeling framework for piezoelectrically actuated MEMS tunable lenses," Opt. Express 24, 28889-28904 (2016).

Article 2

Mahmoud A. Farghaly, Muhammad Nadeem Akram, Einar Halvorsen, "Optical performance of piezoelectrically actuated MEMS tunable lenses with various pupil geometries," Optical Engineering 56(3), 035104 (21 March 2017).

Article 3

Mahmoud A. Farghaly, Ulrik Hanke, Muhammad Nadeem Akram, Einar Halvorsen, "Trial functions for reduced-order models of piezoelectrically actuated microelectromechanical systems tunable lenses," Optical Engineering 57(9), 095103 (24 September 2018).

Article 4: submitted to Journal of Intelligent Material Systems and Structures

Mahmoud A. Farghaly, Vladimir Kartashov, Muhammad Nadeem Akram, Einar Halvorsen, "Electromechanical modeling of piezoelectrically actuated MEMS tunable lenses with geometric nonlinearity".

Other articles not included in the thesis

Cuong H. Nguyen, Mahmoud A. Farghaly, Muhammad N. Akram, Ulrik Hanke, Einar Halvorsen, "Electrode configurations for layered-plate piezoelectric micro-actuators," *Microelectronic Engineering*, Volume 174, Pages 59-63 (2017).

List of Tables

1.1	Polight AS' micro tunable lens versus the macro-scale mechanism VCM (adapted from [8]).	2
2.1	Thermodynamic character functions and their corresponding constitutive equations. The constitutive equations and the thermodynamic functions are written in Einstein's notation. Superscripts D, E, S or T denote that matrix components are measured at zero displacement field, electric field, strain or stress, respectively. In literature, the internal energy function F is often referred to as U .	15
3.1	Optimum γ_v^* and γ_{FEM}^* ratios corresponding to minimum $F\#$ for variational solutions and FEM simulations, respectively. The A_f , $F\#$ and RMSWFE corresponds to γ_{FEM}^* values for tunable lens with polygonal and circular pupils at $V_p = -10V$	48
5.1	Optical power swing for a 30-V source.	76
5.2	The fitting parameters.	79
A.1	Zernike polynomials Z_n^m	98

List of Figures

1.1	(a) The VCM focusing mechanism, which shows two thick-lenses mounted in a barrel surrounded by coils to generate Lorentz forcing and results in vertical movement of the lenses (Adapted from [3]). (b) The Ultrasonic motor mechanism in which the rotor, representing the lower part, has a traveling wave and causes the stator to move rotational movement (Adapted from [4]).	3
1.2	(a) LC lens (Adapted from [9]). (b) Microfluidic lens (Adapted from [10]). (c) Electrowetting-based lens (Adapted from [11]).	4
1.3	(a) Schematic view showing tunable lens's principle of operation; both at rest position when $V_p = 0$ and at focus when V_p is nonzero. (b) Cross-sectional view of tunable lens showing dimensions.	5
3.1	Even Gegenbauer-polynomial basis functions $\phi_m(X)$ on $[-1, 1]$	40
3.2	Planar view of possible study cases of piezoelectrically actuated MEMS tunable lenses. A clamped square diaphragm with circular opening: (a) case I and (b) case II ring actuator with opaque covering outside the ring till the diaphragm edges.	41
3.3	(a) Displacement profiles in xz -plane from FEM and the variational tool ($N = 28$) for square diaphragm with case I actuator at different values of ratio γ for piezoelectric material at $V_p = -10V$. (b) l_2 relative error norm versus polynomial order N	42

3.4 Displacement profiles in xz -plane from FEM and the variational tool ($N = 28$) for square diaphragm with case II actuator at different values of ratio $\gamma_1 = 2c_1/a$ when $\gamma_2 = 2c_2/a$ equals (a) 0.9 and (b) 0.5 at $V_p = -10V$ 42

3.5 Planar view of possible study cases of piezoelectrically-actuated tunable lenses. A clamped square diaphragm with: (a) square, (b) 45° rotated square, (c) hexagonal, (d) octagonal, (e) 22.5° rotated octagonal and (f) circular pupils. The red arrows indicate the reference dimension L_r for each pupil. 44

3.6 Displacement profiles in xz -plane from FEM simulations and the variational solutions ($N = 28$) for a clamped square diaphragm with (a) square, (b) 45° rotated square, (c) hexagonal, (d) octagonal, (e) 22.5° rotated octagonal and (f) circular pupils at different γ ratios with $V_p = -10V$ 45

3.7 (a) Tunable lens arrangement for on-axis optical simulations. (b) Reciprocal $F\#$ and (c) RMSWFE versus the area factor A_f for different pupils using variational solutions and FEM simulations, all with $V_p = -10V$ and $\lambda = 550nm$. The numbers 1 to 6 respectively represent lenses with square, 45-rotated square, hexagonal, octagonal, 22.5-rotated octagonal and circular pupils, respectively. 47

3.8 (a) Arrangement of the tunable lens with a fixed lens in Zemax for optical simulations. Sagittal and (tangential) MTF for (b) the fixed lens alone without movement when the object is located at infinity and 368mm at different field points on the image plane (coordinates are given in mm in legends). MTF for the tunable lens with circular pupil and the fixed lens when the object is located away (c) 1103mm, (d) 552mm and (e) 368mm. 49

3.9	(a) Planar view of pupil-masked case 2. (b) Cross-sectional view showing the 45° -rotated square actuator with its circular lower Pt electrode etched to form a circular pupil. The red arrow indicates the reference dimension L_r for each pupil. The blue arrow indicates the diameter $2c$ for the circular pupil opening in the lower Pt electrode.	50
3.10	Scattering plots of (a) RMSWFE and (b) lens dioptric power $1/f$ with varying the ratios γ_{op} and γ , all with $V_p = -10V$ and $\lambda = 550nm$	51
4.1	Planar views of the piezoelectrically actuated MEMS tunable lens showing decomposing its structure into subdomains. (a) Model 1 break the lens into two subdomains: Ω_I and Ω_2 . (b) Model 2 breaks it into three subdomains: Ω_I , Ω_{II} and Ω_{III} . Subdomains Ω_{II} and Ω_{III} are separated by a fictitious circular boundary $\Gamma_{\Omega_{II}}$	56
4.2	Planar views showing the normalized radial coordinates in the circular and annular subdomains for (a) models 0 and 1, and (b) model 2.	56
4.3	Displacement profiles in xz -plane from FEM and different models at $N = 3$ and $N = 7$ for different values of ratio γ_1 with piezoelectric material at $V_p = -10V$	61
4.4	l_2 relative error norm for the displacement versus number of polynomials N for different models.	62
4.5	Reciprocal $F\#$ and RMSWFE versus the ratio γ_1 , all with $V_p = -10V$ and $\lambda = 550nm$ for the three models.	64
4.6	l_2 relative error norm of (a) reciprocal $F\#$ and (b) RMSWFE versus order N for three models.	65

5.1 Displacement profiles in xz -plane from FEM (dashed) and the variational tool ($N = 13$) for $\gamma_0 = 0.5$ at different layer stresses and voltages. They are at different voltages ranging from -4V (colored blue) to -28V (colored dark green) with a constant step of -4V. 72

5.2 Displacement profiles in xz -plane from FEM (dashed) and the variational tool ($N = 13$) for other γ_0 values at different layer stresses and voltages. They are at different voltages ranging from -4V (colored blue) to -28V (colored dark green) with a constant step of -4V. 74

5.3 $\gamma_0 a / f$ and RMSWFE versus actuation voltage V_p for different $T^{R,(2)}$ values at $T^{R,(1)} = 0$, $\gamma_0 = 0.6$ and $\lambda = 550\text{nm}$ 76

5.4 (a) Measured displacement profile at 0V. (b) Measured displacement profile at 0 V after numerical treatment to remove tilt, rotational misalignment and distorted data around the electrode's inner edges. (c) Cross-sectional profiles from the measurements and model fittings at three voltages. 77

6.1 Equivalent circuit of the tunable lens. 86

6.2 Step response of the lens using the ansatz of (a) model 0 (b) model 1, and (c) model 2 with Rayleigh parameters $\alpha_R = 10^{-6} \text{ s}$ and $\alpha_M = 10^{-4} \text{ s}^{-1}$ 87

Contents

Dedication	i
Preface	v
Acknowledgments	vii
Abstract	ix
List of papers	xiii
List of Tables	xv
List of Figures	xvii
1 Introduction	1
1.1 Tunable focusing mechanisms in literature	1
1.1.1 Macro-scale approaches	2
1.1.2 Micro-scale approaches	3
1.2 Fabrication process of piezoelectric thin films	5
1.3 Motivation	7
1.4 Area of research	7
1.5 Thesis layout	11
2 Variational formulation for piezoelectric plates	13

xxi

2.1	Thermodynamic character functions for piezoelectric media under isothermal conditions	14
2.2	Hamilton's principle for piezoelectric media	16
2.3	Strains	17
2.4	Material symmetry	19
2.5	Voltage and electric field in terms of strains	20
2.6	Stress resultants	22
2.7	Variational formulation	24
2.8	Displacement ansatz and equation of motions	30
3	Modeling framework for piezoelectrically actuated MEMS tunable lenses with various pupil geometries	35
3.1	The linear variational formulation	36
3.2	Displacement ansatz and its suitability for the optoelectromechanical modeling	37
3.3	Variational solutions versus FEM	40
3.3.1	Circular pupils	40
3.3.2	Various pupil geometries	43
3.3.3	Optical performance using ray tracing analysis	46
4	Trial functions for reduced-order modeling of piezoelectrically actuated MEMS tuneable lenses	53
4.1	The need for reduced-order models	54
4.2	Normalized coordinates	55
4.3	New ansätze for model order reduction	57
4.3.1	Model 1	57
4.3.2	Model 2	58
4.4	Variational formulation	59

4.5	Comparison between variational models	59
4.5.1	Variational solutions versus FEM simulations	60
4.5.2	Optical Simulations	62
4.6	New ansätze relation to Zernike polynomials	65
5	Modeling piezoelectrically actuated MEMS tuneable lenses with geometric nonlinearity	69
5.1	Variational formulation	70
5.1.1	Variational solutions versus FEM	71
5.2	Qualitative optical performance	73
5.3	Model versus Measurements	77
6	Conclusions and proposal for future research	81
6.1	Conclusions	81
6.2	Proposals for future research	85
	Appendix A Zernike polynomials	97
	Appendix B Weighted Gegenbauer polynomials	103
	B.1 Mapping weighted Gegenbauer polynomials to Zernike polynomials	104
	Appendix C Dynamic Analysis	111
	Appendix D Article 1	113
	Appendix E Article 2	131
	Appendix F Article 3	143
	Appendix G Article 4	163

1 Introduction

The following chapter provides a literature review of the tunable focusing mechanisms that are sold in the market, and under research with an emphasis on the piezoelectrically actuated MEMS tunable lenses and their fabrication process. It also presents thesis motivation in Sec. 1.3, area of research in Sec. 1.4 and thesis layout in Sec 1.5.

1.1 Tunable focusing mechanisms in literature

Tuning focal length in miniaturized cameras is currently done at macro-scales at the expense of large power dissipation and slow response during focus scanning, as shown in Tab. 1.1. The large power dissipation does not align with the long-life of batteries in digital cameras or smartphones. Therefore, there are other technologies, in evolving phase, that could potentially solve these problems by having weak lenses at micro-scale. Whether the mechanism is at micro or macro scale, the tunable lens could be attached to a fixed-focal-length optical system for adjusting the overall focal length based on the object distance from the pho-

tographing device.

Table 1.1: Polight AS' micro tunable lens versus the macro-scale mechanism VCM (adapted from [8]).

Parameter	Polight AS	VCM
Focus response	1 ms	5-15 ms
Power consumption	< 5mW	220 mW
Field-Of-View(FoV)*	no auto-focus pumping	auto-focus pumping
Magnetic interference	No	Yes

* FOV is reduced for VCM during focus adjustment due to the relatively large movement of tunable lens within the system, while micro-lenses displacement is in the order of a few micrometers. This cause almost no auto-focus pumping when compared to VCM.

1.1.1 Macro-scale approaches

In conventional macro-scale focusing systems sold in the camera market nowadays, for example VCM [3] and ultrasonic motors [4], tunable focus is achieved through changing the relative positions of lenses mounted inside a barrel in front of a fixed lens. Each technology moves that barrel differently within the camera housing. The VCM, shown in Fig. 1.1a, effectively uses Lorentz forces on current carrying coils wrapped around the barrel to move it forwards or backwards. Ultrasonic motors, shown in Fig. 1.1b, use piezoelectric actuators to generate a traveling wave rotating along the circumference of a circular disk and couple the resultant circular movement through a gear system to an axially moving lever attached to the barrel.

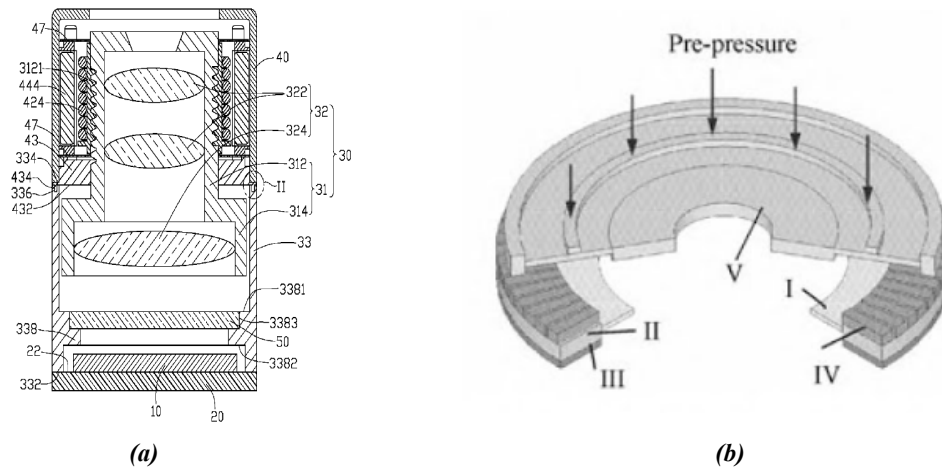


Figure 1.1: (a) The VCM focusing mechanism, which shows two thick-lenses mounted in a barrel surrounded by coils to generate Lorentz forcing and results in vertical movement of the lenses (Adapted from [3]). (b) The Ultrasonic motor mechanism in which the rotor, representing the lower part, has a traveling wave and causes the stator to move rotational movement (Adapted from [4]).

1.1.2 Micro-scale approaches

Tunable focus in micro-scale systems is generally achievable by two approaches. The first approach is to change the effective refractive index as in a liquid crystal (LC) lens [9]. An LC lens, shown in Fig. 1.2a, can converge or diverge light beams by controlling the electric field that reorients LC molecules causing a spatially dependent refractive index within LC layers. The second approach is to change the interface slope through which the light rays pass between two media with different refractive indices. Tunable microfluidic lenses [10, 12], shown in Fig. 1.2b, uses a pump to control the pressure of a liquid trapped inside a fluidic cavity to deform the cavity's top surface. A tunable liquid lens, shown in 1.2c, changes the interface curvature between two polar liquids by electrowetting [11].

The MEMS tunable lenses, that are the focus of this thesis, are based on piezo-

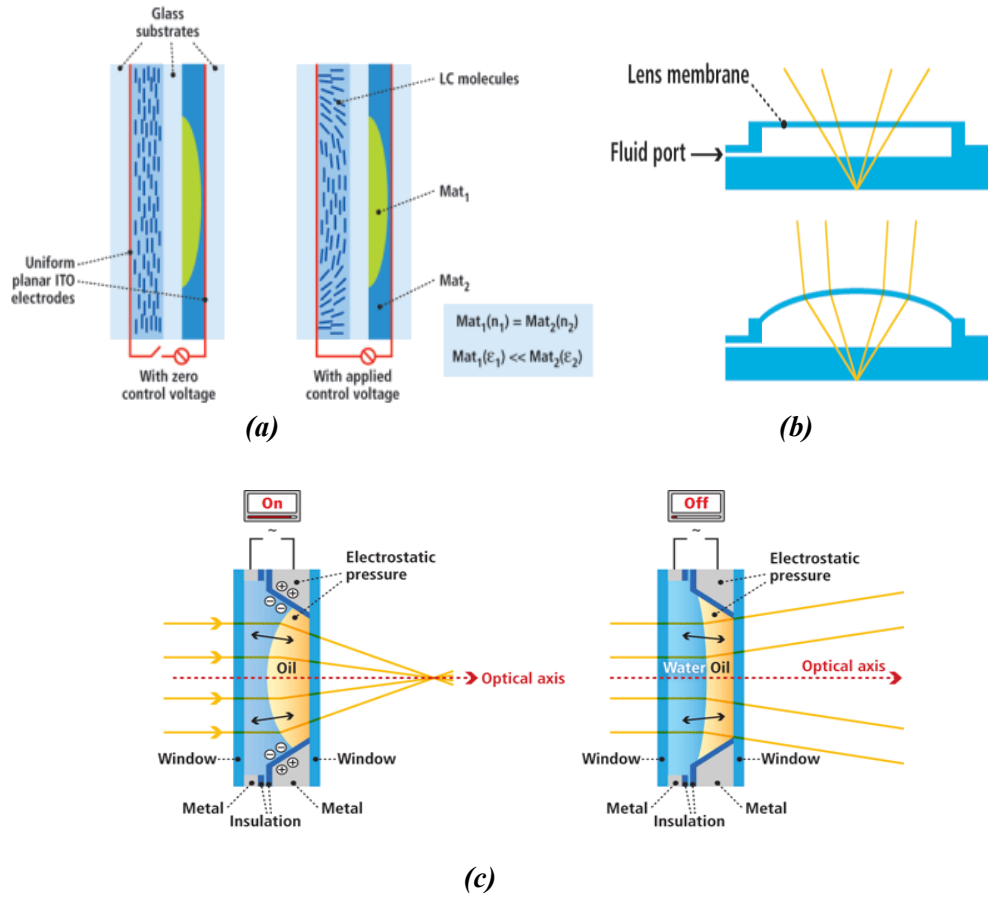


Figure 1.2: (a) LC lens (Adapted from [9]). (b) Microfluidic lens (Adapted from [10]). (c) Electrowetting-based lens (Adapted from [11]).

electric actuation as a bending mechanism of a diaphragm to provide a voltage dependent curvature at the interface between air and a polymer [13]. In the paraxial approximation for a thin plano-convex lens with radius of curvature R and refractive index n_{medium} , the focal length is $f = R/(n_{\text{medium}} - 1)$. The lens shown in Fig. 1.3 consists of four elements: a piezoelectric actuator, a thin transparent glass layer, a soft polymer gel and a transparent thicker glass layer as substrate. A DC voltage V_p is applied to the piezoelectric actuator to set an electric field E_3 having the same alignment as the polarization within the piezoelectric material. This causes an in-plane contraction in the piezoelectric stack and the

flexible thin glass layer bends upwards. The upper surface of the soft polymer (or fluid) is shaped by this bending, forming a complicated refractive surface for light rays, as shown in Fig. 1.3. Thus, controlling the actuation voltage V_p makes the lens's focusing-power tunable and enables focusing at objects located at different distances from the camera.

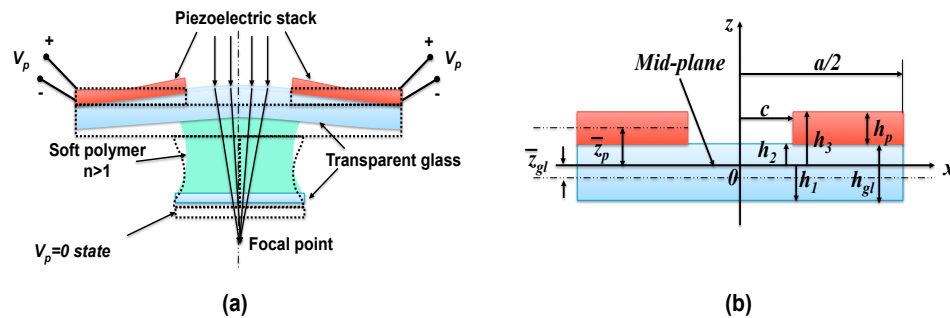


Figure 1.3: (a) Schematic view showing tunable lens's principle of operation; both at rest position when $V_p = 0$ and at focus when V_p is nonzero. (b) Cross-sectional view of tunable lens showing dimensions.

1.2 Fabrication process of piezoelectric thin films

The thin-film PZT stacks are either fabricated by sputtering [14], laser ablation [15], chemical vapor deposition [16] or sol-gel [17--19]. However, the sol-gel technique when combined with spin coating, has become the most widely used fabrication technique. Spin coating and multiple rapid thermal annealing (RTA) steps improve the film quality by providing control over densification to have crack-free thin films, and crystallization into the desired perovskite [17]. Thus, the fabrication process involves heating treatment, which leads to the impossi-

bility of having a PZT stack free from residual stresses after being cooled down.

Such piezoelectric lenses are fabricated by sol-gel technique [17--19] with spin coatings. This fabrication process involves many steps of thermal annealing followed by a hot-polling step to ensure the orientation of piezoelectric domains in the favored direction. The piezoelectric stack is composed of layers with different thermal expansion coefficients [20--23], which builds in-plane stresses inside these layers after being cooled down to the room temperature.

For example, a $1\mu\text{m}$ thin-film PZT stack is formed layer-by-layer through multiple spin coating [19]. Each layer is 60nm thick and is pyrolyzed at 350°C for 15s using slowly ramp of 20°Cs^{-1} . To reduce residual stresses, the process is splited into four steps of RTA ranging from 15 to 30°Cs^{-1} that are employed after every $250\mu\text{m}$. At the end, the wafer would have faced 16 spin coatings and 4 RTA steps. Afterwards, the PZT thin film is hot poled at 150°C with a voltage source setting electric field of $50\text{-}250\text{ kVcm}^{-1}$ for 10 min. The final layer structure of the PZT stack form the process in [19, 24] is Si/SiO₂/Pt/PZT/Au. These layers differ in their thermal expansion coefficient, which results in having residual stresses in these layers. For example, the residual stress for that $1\mu\text{m}$ PZT film amounts respectively to 110 MPa and 180 MPa before and after the poling step [18]. The thermal treatments, during fabrication and poling, determine the value of residual stresses.

For the linear performance of piezoelectrically-actuated lens, discussed in chapters 3 & 4, we neglect the effect of residual stresses because of the linear assumption. However, in chapter 5, we consider their effect as a part of modeling the nonlinear behavior of this lens.

1.3 Motivation

This thesis is a part of a project called '*beat the human eye*' that focuses on research and development of the piezoelectrically actuated MEMS tunable lens (shown in Fig. 1.3) in order to find novel actuator designs to enlarge the tunable range of focal length while maintaining the RMS-wavefront error (RMSWFE) below $\lambda/14$; as recommended by Maréchal's criterion [25]. In this way, the tunable lens is diffraction-limited lens that can be added to a fixed-focal-length lens system resulting in an overall tunable optical system.

The objective of this thesis is to develop semi-analytical models for the tunable lens, which has a complex structure of a square diaphragm with a hole running only through the piezoelectric actuator layer. Through these models, we could investigate different design concepts based on the understanding gained through the models' parameters.

1.4 Area of research

Previous research [26--29] has dealt with pure elastic (circular and rectangular) plates, with no piezoelectric elements, taking the approach of constructing FEM elements derived from the solutions of the biharmonic differential equation of the circular plates. Also, this research has mostly concentrated on finding the eigen frequencies and their mode-shapes that are of great importance in the field of aerospace. However, research from [30, 31] has solved the static case of piezoelectrically-actuated pump that is composed of a clamped circular piezoelectric plate with a hole running only through the piezoelectric actuator; which

is similar to the lens structure under study. Difficulties, from the modeling aspect, are the discontinuity at the lens layered structure and having circular symmetry in the pupil region in addition to square symmetry of the diaphragm. This difficulties has not been yet solved in the previous literature through semi-analytical expressions. In this thesis, we deal with these difficulties in two different manners in chapters 3 and 4.

Not only that we want to approximate the lens displacement, but also to find a suitable displacement ansatz suited to simplify the mapping to optical programs without any accuracy lost in the mapping. Yet, the most challenging job is to have at the end a reduced-order model through which the lens displacement is obtained through a simple substitution of the driving voltage value and the layers' elastic and piezoelectric coefficients. With such reduced-order models, the system-level lens designers can manage to get the new lens profile without the burden to run FEM simulations.

In order to begin with approximating the lens displacement, we have started with a variational formulation (discussed in details in ch. 2) resulted from Hamilton's principle. After simplifications suiting the lens under study, we have ended up with two system of equations; the first is for the linear case while the second is for the nonlinear case considering only the geometric nonlinearity.

In order to fill the knowledge gaps discussed above, we have followed the following steps:

1. Expressing the stress resultants from (refer to Eq. 2.18) in terms of zero and first order strains, material parameters, driving voltage and residual stresses. It is of interest to end up with a correction factor to the membrane flexural stiffness (Eq. (2.19)) due to the piezoelectric coupling within the piezoelectric material, similar to what has been discussed for piezoelectric beams in [32].

2. Deducing two equations of motion; one for the linear case and the other for the nonlinear one. As a result of the pupil opening, we have found out that the nonlinear system of equations has non-zero quadratic stiffnesses that result in having a favorable bending direction for the lens (*hardening* and *softening* effects) depending on the relation between layers' elastic coefficients. This affects the lens performance depending on the values of the driving voltage and the residual layers' stresses.
3. Choosing the displacement ansatz as a sum of the weighted Gegenbauer polynomials because they satisfy the clamped boundary conditions and are orthogonal to eliminate the possibility of a numerically ill-conditioned system of equations arising from the variational treatment. Yet, these polynomials are easy to be mapped to Zernike polynomials, which suits optical representation of the lens sag for optical programs such as Zemax.
4. Considering different polygonal pupil geometries and to move around the difficulty of calculating the variational integrals, we have presented the idea of complementary pupil function $\bar{\zeta}(X, Y)$ in [33] that has simplified numerical calculations of the equivalent stiffness matrix $R_{k_1 k_2}$.
5. Calculating analytical expressions for the linear stiffnesses using the symbolic toolbox in MATLAB in terms of the circular pupil opening ratio γ . However, for other polygonal shapes, the pupil area was divided into small square elements over which the variational integrals have been evaluated. Then, the final linear stiffness matrix, with the help of the complementary pupil function, has been evaluated by subtracting the sum of the integrals over those square elements.
6. Obtaining variational solutions in a time of 1.3 seconds while it has taken FEM 1.5 minutes using the same computer. Also, we have validated the

linear variational solutions versus FEM and have obtained less than 10% displacement relative error for the different pupil geometries.

7. Proposing a novel actuator design (*i.e.* pupil masking) that having a 45-rotated opening in the piezoelectric actuator while maintaining a circular pupil provides a tradeoff between the dioptric power and RMSWFE allowing larger apertures when compared with the original design shown in Fig. 1.3.
8. Performing system-level simulations such that when the tunable lens is combined with a fixed lens, the overall performance is not degrading throughout the whole focusing range despite changing object distances from the lens.
9. Reducing the number of Degrees-Of-Freedom (DOFs) of the linear model from 120 to 10 by introducing new analytical ansätze that are not neglecting the discontinuity at the circular pupil boundary. This has resulted in speeding the convergence to a solution with respective accuracies of 11.4% and 6.2% for RMSWFE and $1/F\#$ with only 10 DOFs.
10. Calculating analytical expressions for the nonlinear stiffnesses. The weighted Gegenbauer polynomials have been written on the form of a Fourier trigonometric series. By using the orthogonality property of the trigonometric functions, the number of nonlinear variational integrals has been tremendously reduced.
11. Validating the nonlinear model versus FEM and measurements. Based on the understanding of the model parameters, we have been able to provide the second design insight on how to enlarge the tunable focusing range through controlling the layer stresses during fabrication. This is done by

operating the lens simultaneously as a plano-concave and a plano-convex lens. In this manner, RMSWFE values are kept low to still have a tunable diffraction-limited lens while the focal length changes from being negative to positive.

1.5 Thesis layout

Chapter 2 presents in details the variational formulation beginning from energy methods that ends with two equations of motion; one is linear for the linear performance and the second is cubic system for the geometric nonlinear performance. In chapter 3, the modeling framework has been used to compare between the optical performance of various pupil geometries, then we have performed system-level simulations for the tunable lens combined with a fixed lens, and have examined the design concept of pupil masking versus the original design. Chapter 4 presents the reduced-order linear models resulted from using a piece-wise ansätze; each approximating the lens displacement at different regions. Also, we have presented a comparison between the different models accuracies in terms of the displacement and optical parameters. In chapter 5, the nonlinear model is fully developed and validated versus FEM and measurements. At the end, chapter 6 represents the conclusion and proposal for future research. The appendix includes expressions of Zernike polynomials, examples of expanding weighted Gegenbauer polynomials in terms of Zernike polynomials, starting ground expressions for the lens' dynamic model and all the scientific publications resulted from this thesis.

2 Variational formulation for piezoelectric plates

The variational formulation is an essential part of the electromechanical modeling framework developed for the piezoelectrically actuated MEMS tunable lenses. It is based on Hamilton's principle that is a general energy method to deduce equations of motion. This chapter introduces mathematically the variational formulation and the simplifying assumptions related to geometry, strains, material symmetry and electric fields. The variational formulation finally produces a linear (or nonlinear) system of equations that can be solved in MATLAB [5] taking calculation time less than that is taken by Finite Element Methods (FEM) programs *i.e.* COMSOL [6].

This chapter starts in sections 2.1-2 with introducing different thermodynamic functions under isothermal conditions and Hamilton's principle for piezoelectric media. Then, throughout sections 2.3-7, the variational formulation is mathematically expressed starting from the electrical enthalpy after introducing the simplifying assumptions and their reasoning. Finally, section 2.8 closes with linear and nonlinear equations of motion that are used for determining the lens' displacement through the whole thesis.

2.1 Thermodynamic character functions for piezoelectric media under isothermal conditions

A *thermodynamic function* has energy units and depends on sets of conjugate pairs called *state variables* such as (stress T , strain S), (electric field intensity E , electric field displacement D) and (temperature, specific entropy). We will drop the later pair since we are here more concerned about the electromechanical coupling under isentropic conditions (for thermodynamic functions with the later pair, the reader may refer to Ref. [34]). With the left four state variables (T, S) and (E, D), one can possibly formulate four thermodynamic functions based on choosing which two of the state variables are the independent ones. Table 2.1 lists these four thermodynamic functions, their formulas and the corresponding constitutive equations¹ [1, 35]. All four functions are related to each others through Legendre transformation².

In our development of the variational formulation for piezoelectric media, we have chosen the strain and the electric field intensity as the independent variables. As a result, the thermodynamic character function is the Electric Gibbs energy G_2 . Afterwards, we use a modified Lagrangian for the piezoelectric media to end up with the electric enthalpy H as it is often done in literature [37, 38].

¹are set of equations relating the dependent state variables to the independent ones.

² is a mathematical transformation of a function with certain state variables to another function with new state variables [36].

Table 2.1: Thermodynamic character functions and their corresponding constitutive equations. The constitutive equations and the thermodynamic functions are written in Einstein's notation. Superscripts D , E , S or T denote that matrix components are measured at zero displacement field, electric field, strain or stress, respectively. In literature, the internal energy function F is often referred to as U .

Independent variable	constitutive equations	Thermodynamic function
S, D	$T_{ij} = C_{ijkl}^D S_{kl} - h_{kij} D_k$ $E_i = -h_{ikl} S_{kl} + \beta_{ik}^S D_k$	Internal energy $F = \frac{1}{2} C_{ijkl}^D S_{ij} S_{kl} - h_{ijk} E_i S_{jk} + \frac{1}{2} \beta_{ij}^S D_i D_j$
T, E	$S_{ij} = s_{ijkl}^E S_{kl} + d_{kij} E_k$ $D_i = d_{ikl} T_{kl} + \epsilon_{ik}^T E_k$	Gibbs free energy $G = -\frac{1}{2} s_{ijkl}^E T_{ij} T_{kl} - d_{ijk} E_i T_{jk} - \frac{1}{2} \epsilon_{ij}^T E_i E_j$
T, D	$S_{ij} = s_{ijkl}^D T_{kl} + g_{kij} D_k$ $E_i = -g_{ikl} T_{kl} + \beta_{ik}^T D_k$	Elastic Gibbs energy $G_1 = -\frac{1}{2} s_{ijkl}^D T_{ij} T_{kl} - g_{ijk} D_i T_{jk} + \frac{1}{2} \beta_{ij}^T D_i D_j$
S, E	$T_{ij} = C_{ijkl}^E S_{kl} - e_{kij} E_k$ $D_i = e_{ikl} S_{kl} + \epsilon_{ik}^S E_k$	Electric Gibbs energy $G_2 = \frac{1}{2} C_{ijkl}^E S_{ij} S_{kl} - e_{ijk} E_i S_{jk} - \frac{1}{2} \epsilon_{ij}^S E_i E_j$

Relation between the thermodynamic functions
 $G = F - TS - ED, G_1 = F - TS, G_2 = F - ED$

2.2 Hamilton's principle for piezoelectric media

Hamilton's principle is more general than Newtonian theory in deducing equations of motion for a mechanical system. It is a general postulate starts with formulating a scalar function called the Lagrangian and is followed by minimizing the time integral of its variation with respect to the independent variables. This integral minimization consequently leads to equations of motion that are called Euler-Lagrange equations. Hamilton's principle is stated as [39]:

"Of all the possible paths along which a dynamical system may move from one point to another within a specified time interval (consistent with any constraints), the actual path followed is that which minimizes the time integral of the difference between the kinetic and potential energies".

From the calculus of variation [39, 40], the Hamilton's principle for a conservative system with no constraints can be expressed as

$$\delta \int_{t_1}^{t_2} L(\mathbf{q}, \dot{\mathbf{q}}) dt = 0, \quad (2.1)$$

where δ is the variation operator³. \mathbf{q} and $\dot{\mathbf{q}}$ are respectively the independent state vector and its time derivative. $L = K - U$ is the Lagrangian function where K and U are the kinetic and the potential energies. Applying calculus of variations lemmas [39, 40] leads to Euler-Lagrange equations of motion that are given by

$$\frac{d}{dt} \left(\frac{\partial L}{\partial \dot{\mathbf{q}}} \right) - \frac{\partial L}{\partial \mathbf{q}} = 0. \quad (2.2)$$

³is similar to differential operator with respect to the independent variables.

These Euler-Lagrange equations are solved to determine the system new state vector.

For piezoelectric media, it is more convenient to transform the potential energy in the Lagrangian into the electric enthalpy $H = U - ED$ (refer to Tab. 2.1) through Legendre transformation since the independent pair of variables considered are (S, E) . The Hamilton's principle from Eq. (2.1) is then modified to include the virtual work due to external forces [38,41] and it becomes

$$\delta \int_{t_1}^{t_2} L_p dt + \int_{t_1}^{t_2} \delta W dt = \delta \int_{t_1}^{t_2} \Pi dt = 0, \quad (2.3)$$

where $L_p = K - H$ is the Lagrangian of piezoelectric media written as the difference between the kinetic energy and the electrical enthalpy rather than the difference between the kinetic energy minus the potential energy [38]. The term δW is the virtual work due to external mechanical and electric forces. Π is a mathematical function equals to $L_p + W$. Expressions for δK , δH and δW are discussed thoroughly in section 2.7.

2.3 Strains

The tunable lenses under consideration compose of a square elastic membrane and a piezoelectric stack that their total thickness (*e.g.* $22\mu\text{m}$) is less than 100 times the in-plane dimension (*e.g.* 3mm). Thus, the 3-dimensional elasticity equations can be replaced by a simpler 2-dimensional classical plate theories such as von Kármán⁴ or Kirchhoff⁵ plate theories. These classical laminated plate the-

⁴is a nonlinear 2-D plate theory as it includes the dominant term of stretching strains due to the transverse displacement w_0 .

⁵it fully neglects the mid-plane stretching and shear strains due to the the transverse displacement w_0 in expressions of S_{xx}^0, S_{yy}^0 and γ_{xy}^0 from von Kármán strains.

ories have the following assumptions [42]

1. *Straight lines perpendicular to the mid-surface before the deformation remain straight after deformation.*
2. *The transverse normals do not experience elongation (i.e., they are inextensible)*
3. *The transverse normals rotate such that they remain perpendicular to the middle surface after deformation.*

These assumptions amount that the plate displacements (u, v, w) in cartesian coordinates can be expressed as

$$u(x, y, z, t) = u_0(x, y, t) - z \frac{\partial w_0}{\partial x}, \quad (2.4a)$$

$$v(x, y, z, t) = v_0(x, y, t) - z \frac{\partial w_0}{\partial y}, \quad (2.4b)$$

$$w(x, y, z, t) = w_0(x, y, t), \quad (2.4c)$$

where u_0, v_0 and w_0 are respectively the mid-plane displacements in x, y and z directions. As a result, the normal and shear von Kármán strains can be written as

$$S_{xx} = \frac{\partial u_0}{\partial x} + \frac{1}{2} \left(\frac{\partial w_0}{\partial x} \right)^2 - z \frac{\partial^2 w_0}{\partial x^2} = S_{xx}^0 + z S_{xx}^1, \quad (2.5a)$$

$$S_{yy} = \frac{\partial v_0}{\partial y} + \frac{1}{2} \left(\frac{\partial w_0}{\partial y} \right)^2 - z \frac{\partial^2 w_0}{\partial y^2} = S_{yy}^0 + z S_{yy}^1, \quad S_{zz} = 0, \quad (2.5b)$$

$$\gamma_{xy} = \frac{\partial u_0}{\partial y} + \frac{\partial v_0}{\partial x} + \frac{\partial w_0}{\partial x} \frac{\partial w_0}{\partial y} - 2z \frac{\partial^2 w_0}{\partial x \partial y} = \gamma_{xy}^0 + z \gamma_{xy}^1, \quad (2.5c)$$

$$\gamma_{yz} = 0, \quad \gamma_{xz} = 0, \quad (2.5d)$$

where $(S_{ii}^0, \gamma_{ij}^0)$ and $(S_{ii}^1, \gamma_{ij}^1)$ are the membrane stretching strains at middle surface and bending (flexural) strains. The terms depending on the transverse displace-

ment w_0 in the strains $(S_{ii}^0, \gamma_{ij}^0)$ reflect the geometric nonlinearity. The variational non-zero strains become

$$\delta S_{xx}^0 = \frac{\partial \delta u_0}{\partial x} + \frac{\partial w_0}{\partial x} \frac{\partial \delta w_0}{\partial x}, \quad \delta S_{xx}^1 = -\frac{\partial^2 \delta w_0}{\partial x^2}, \quad (2.6a)$$

$$\delta S_{yy}^0 = \frac{\partial \delta v_0}{\partial y} + \frac{\partial w_0}{\partial y} \frac{\partial \delta w_0}{\partial y}, \quad \delta S_{yy}^1 = -\frac{\partial^2 \delta w_0}{\partial y^2}, \quad (2.6b)$$

$$\delta \gamma_{xy}^0 = \frac{\partial \delta u_0}{\partial y} + \frac{\partial \delta v_0}{\partial x} + \left(\frac{\partial \delta w_0}{\partial x} \frac{\partial w_0}{\partial y} + \frac{\partial w_0}{\partial x} \frac{\partial \delta w_0}{\partial y} \right), \quad \delta \gamma_{xy}^1 = -2 \frac{\partial^2 \delta w_0}{\partial x \partial y}. \quad (2.6c)$$

2.4 Material symmetry

Due to the PZT material symmetry [1], the constitutive equations referred to the middle plane as a reference plane can be reduced to

$$\begin{bmatrix} T_{xx} \\ T_{yy} \\ T_{xy} \\ D_3 \end{bmatrix} = \begin{bmatrix} \bar{Q}_{11} & \bar{Q}_{12} & 0 \\ \bar{Q}_{12} & \bar{Q}_{22} & 0 \\ 0 & 0 & \bar{Q}_{66} \\ \bar{e}_{31} & \bar{e}_{32} & 0 \end{bmatrix} \begin{bmatrix} S_{xx} \\ S_{yy} \\ \gamma_{xy} \end{bmatrix} + \begin{bmatrix} -\bar{e}_{31} \\ -\bar{e}_{32} \\ 0 \\ \bar{\epsilon}_{33}^S \end{bmatrix} E_3 \quad (2.7a)$$

$$\begin{bmatrix} D_1 \\ D_2 \end{bmatrix} = \begin{bmatrix} \bar{e}_{15} & 0 \\ 0 & \bar{e}_{24} \end{bmatrix} \begin{bmatrix} \gamma_{yz} \\ \gamma_{xz} \end{bmatrix} + \begin{bmatrix} \bar{\epsilon}_{11}^S & 0 \\ 0 & \bar{\epsilon}_{22}^S \end{bmatrix} \begin{bmatrix} E_1 \\ E_2 \end{bmatrix}, \quad (2.7b)$$

where T_{ij} , S_{ij} , γ_{ij} , D_i and E_i are components of stress, normal strain, shear strain, electric displacement and electric field respectively. The material axes (1, 2 and 3) coincide with the coordinate axes (x , y and z). D_1 and D_2 can be neglected due to negligible transverse shear strains (γ_{xz} and γ_{yz}) and zero E_1 and E_2 from the electrode configuration (refer to Fig 1.3). $(\bar{Q}_{ij}, \bar{e}_{ij}, \bar{\epsilon}_{ij}^S)$ are effective material

properties (due to plane stress condition ⁶), defined as

$$\bar{Q}_{ij} = \bar{C}_{ij}, \quad \bar{C}_{11} = \frac{s_{11}^E}{(s_{11}^E + s_{12}^E)(s_{11}^E - s_{12}^E)}, \quad \bar{C}_{12} = \frac{-s_{12}^E}{(s_{11}^E + s_{12}^E)(s_{11}^E - s_{12}^E)}, \quad (2.8a)$$

$$\bar{C}_{66} = \frac{1}{s_{66}^E}, \quad \bar{e}_{31} = \bar{e}_{32} = \frac{d_{31}}{s_{11}^E + s_{12}^E}, \quad \bar{\epsilon}_{33}^S = \epsilon_{33}^T - \frac{2d_{31}^2}{s_{11}^E + s_{12}^E}, \quad (2.8b)$$

where s_{ij}^E is the ij -th elasticity coefficient at zero electric field; $(i, j) = 1, 2, \dots, 6$. d_{31} is the longitudinal d-form piezoelectric coupling coefficient. ϵ_{33}^T is the dielectric constant in the third material axis under zero stress while $\bar{\epsilon}_{33}^S$ is the effective one under zero strain.

2.5 Voltage and electric field in terms of strains

From Gauss's law and electric boundary conditions, we can formulate expressions for E_3 and the voltage v in terms of the bending strains, the DC actuation voltage V_p and layers dimensions. Since the piezoelectric layer is a charge free region and the in-plane components of the electric displacement are negligible, Gauss's law is simplified to

$$\nabla \cdot D \approx \frac{\partial D_3(x, y, z)}{\partial z} = 0. \quad (2.9)$$

⁶Having zero S_{zz} results in neglecting the transverse normal stress T_{zz} in the variational formulation. Thus, we have plane strain and plane stress conditions.

By substituting with D_3 expression from Eq. (2.7a), the electric field and voltage can be given by

$$E_3(x, y, z) = -\frac{1}{\bar{\epsilon}_{33}^S} \left(\bar{e}_{31} S_{xx}^1 + \bar{e}_{32} S_{yy}^1 \right) z + c_1, \quad (2.10)$$

$$v(x, y, z) = -\int E_3(x, y, z) dz = \frac{1}{\bar{\epsilon}_{33}^S} \left(\bar{e}_{31} S_{xx}^1 + \bar{e}_{32} S_{yy}^1 \right) \frac{z^2}{2} - c_1 z + c_2, \quad (2.11)$$

where the integration constants c_1 and c_2 are determined from the electrical boundary conditions ($v = 0$ at $z = h_2$ and $v = V_p$ at $z = h_3$) (refer to Fig. 1.3) as follows

$$c_1 = \frac{-V_p}{h_p} + \frac{1}{\bar{\epsilon}_{33}^S} \left(\bar{e}_{31} S_{xx}^1 + \bar{e}_{32} S_{yy}^1 \right) \bar{z}_p, \quad (2.12a)$$

$$c_2 = c_1 h_2 - \frac{1}{\bar{\epsilon}_{33}^S} \left(\bar{e}_{31} S_{xx}^1 + \bar{e}_{32} S_{yy}^1 \right) \frac{h_2^2}{2}. \quad (2.12b)$$

The final expressions of the electric field and the voltage in terms of bending strains are

$$E_3(x, y, z) = \frac{-V_p}{h_p} - \frac{\bar{e}_{31}}{\bar{\epsilon}_{33}^S} \left(S_{xx}^1 + S_{yy}^1 \right) (z - \bar{z}_p), \quad (2.13a)$$

$$v(x, y, z) = \frac{V_p}{h_p} (z - h_2) + \frac{\bar{e}_{31}}{\bar{\epsilon}_{33}^S} \left(S_{xx}^1 + S_{yy}^1 \right) \left(\frac{(z^2 - h_2^2)}{2} + \bar{z}_p (h_2 - z) \right), \quad (2.13b)$$

where $\bar{z}_p = (h_2 + h_3)/2$. The first term on the right hand side of Eqs. (2.13) is the field one would have without deformation and the second term is a result of the deformation through the piezoelectric coupling.

⁷ $E_3(x, y, z) = -\nabla v(x, y, z)$ is also valid for time varying fields as an electrostatic approximation, because piezoelectric materials are dielectrics with low loss tangent such that conduction currents can be neglected.

2.6 Stress resultants

It is useful to integrate stresses from Eq (2.7a) over the thickness and to include the layers residual stresses to get expressions for the stress resultants as follows [42, 43]

$$\begin{bmatrix} N_{xx} \\ N_{yy} \\ N_{xy} \\ M_{xx} \\ M_{yy} \\ M_{xy} \end{bmatrix} = \begin{bmatrix} A_{11} & A_{12} & 0 & B_{11} & B_{12} & 0 \\ A_{12} & A_{22} & 0 & B_{21} & B_{22} & 0 \\ 0 & 0 & A_{66} & 0 & 0 & B_{66} \\ B_{11} & B_{12} & 0 & D_{11} & D_{12} & 0 \\ B_{12} & B_{22} & 0 & D_{21} & D_{22} & 0 \\ 0 & 0 & B_{66} & 0 & 0 & D_{66} \end{bmatrix} \begin{bmatrix} S_{xx}^0 \\ S_{yy}^0 \\ \gamma_{xy}^0 \\ S_{xx}^1 \\ S_{yy}^1 \\ \gamma_{xy}^1 \end{bmatrix} - \begin{bmatrix} N_{xx}^E \\ N_{yy}^E \\ N_{xy}^E \\ M_{xx}^E \\ M_{yy}^E \\ M_{xy}^E \end{bmatrix} + \begin{bmatrix} \sum_{l=1}^{n_l} N_{xx}^{R,(l)} \\ \sum_{l=1}^{n_l} N_{yy}^{R,(l)} \\ \sum_{l=1}^{n_l} N_{xy}^{R,(l)} \\ \sum_{l=1}^{n_l} M_{xx}^{R,(l)} \\ \sum_{l=1}^{n_l} M_{yy}^{R,(l)} \\ \sum_{l=1}^{n_l} M_{xy}^{R,(l)} \end{bmatrix}, \quad (2.14)$$

where

$$\begin{aligned} A_{ij} &= \sum_{l=1}^{n_l} \bar{Q}_{ij}^{(l)} (h_{l+1} - h_l), & B_{ij} &= \frac{1}{2} \sum_{k=1}^{n_l} \bar{Q}_{ij}^{(l)} (h_{l+1}^2 - h_l^2), \\ D_{ij} &= \frac{1}{3} \sum_{k=1}^{n_l} \bar{Q}_{ij}^{(l)} (h_{l+1}^3 - h_l^3). \end{aligned} \quad (2.15)$$

$\bar{Q}_{ij}^{(l)}$ are the effective stiffness coefficients for the l^{th} layer and ($i, j=1, 2, 6$). (S_{ii}^0 , γ_{xy}^0) and (S_{ii}^1 , γ_{xy}^1) are membrane stretching strains at middle surface and bending (flexural) strains [42]. N_{ij} and M_{ij} are the thickness integrated forces and moments, respectively. N_{ij}^E and M_{ij}^E identified by a superscript E are terms that originate from the piezoelectric coupling [43]. The other terms $N_{ij}^{R,(l)}$ and $M_{ij}^{R,(l)}$ identified by a superscript R originate from fabrication residual stresses in the l^{th}

layer. The stress resultants are given by

$$(N_{xx}, N_{yy}, N_{xy}, M_{xx}, M_{yy}, M_{xy}) = \int (T_{xx}, T_{yy}, T_{xy}, zT_{xx}, zT_{yy}, zT_{xy}) dzm \quad (2.16a)$$

$$(N_{xx}^E, N_{yy}^E, N_{xy}^E, M_{xx}^E, M_{yy}^E, M_{xy}^E) = \int (\bar{e}_{31}, \bar{e}_{32}, \bar{e}_{36}, z\bar{e}_{31}, z\bar{e}_{32}, z\bar{e}_{36}) E_3 dz, \quad (2.16b)$$

$$(N_{xx}^{R,(l)}, N_{yy}^{R,(l)}, N_{xy}^{R,(l)}, M_{xx}^{R,(l)}, M_{yy}^{R,(l)}, M_{xy}^{R,(l)}) = \int (T_{xx}^{R,(l)}, T_{yy}^{R,(l)}, T_{xy}^{R,(l)}, zT_{xx}^{R,(l)}, zT_{yy}^{R,(l)}, zT_{xy}^{R,(l)}) dz. \quad (2.16c)$$

Using Eqs. (2.13), we can express the stress resultant originating from piezoelectric coupling as

$$N_{xx}^E = N_{yy}^E = -\bar{e}_{31} V_p, \quad N_{xy}^E = 0, \quad (2.17a)$$

$$M_{xx}^E = M_{yy}^E = -\bar{e}_{31} \left[\frac{\bar{e}_{31}}{\bar{\epsilon}_{33}^S} (S_{xx}^1 + S_{yy}^1) \left(\frac{(h_3 - h_2)^3}{12} \right) + V_p \bar{z}_p \right], \quad M_{xy}^E = 0. \quad (2.17b)$$

By backsubstituting from Eqs. (2.17) into Eq. (2.14), we get the stress resultants

$$\begin{bmatrix} N_{xx} \\ N_{yy} \\ N_{xy} \\ M_{xx} \\ M_{yy} \\ M_{xy} \end{bmatrix} = \begin{bmatrix} A_{11} & A_{12} & 0 & B_{11} & B_{12} & 0 \\ A_{12} & A_{22} & 0 & B_{21} & B_{22} & 0 \\ 0 & 0 & A_{66} & 0 & 0 & B_{66} \\ B_{11} & B_{12} & 0 & D_{11}^* & D_{12}^* & 0 \\ B_{12} & B_{22} & 0 & D_{21}^* & D_{22}^* & 0 \\ 0 & 0 & B_{66} & 0 & 0 & D_{66}^* \end{bmatrix} \begin{bmatrix} S_{xx}^0 \\ S_{yy}^0 \\ \gamma_{xy}^0 \\ S_{xx}^1 \\ S_{yy}^1 \\ \gamma_{xy}^1 \end{bmatrix} + \bar{e}_{31} V_p \begin{bmatrix} 1 \\ 1 \\ 0 \\ \bar{z}_p \\ \bar{z}_p \\ 0 \end{bmatrix} + \begin{bmatrix} \sum_{l=1}^{n_l} N_{xx}^{R,(l)} \\ \sum_{l=1}^{n_l} N_{yy}^{R,(l)} \\ \sum_{l=1}^{n_l} N_{xy}^{R,(l)} \\ \sum_{l=1}^{n_l} M_{xx}^{R,(l)} \\ \sum_{l=1}^{n_l} M_{yy}^{R,(l)} \\ \sum_{l=1}^{n_l} M_{xy}^{R,(l)} \end{bmatrix}, \quad (2.18)$$

where

$$D_{ij}^* = D_{ij}^{\text{gl}} + D_{ij}^{\text{p}} = \sum_{k=1}^2 \bar{Q}_{ij}^{(l)} \left[\frac{1}{12} \left(1 + \chi_{ij}^{(l)} \right) (h_{l+1} - h_l)^3 \right], \chi_{ij}^{(l)} = \frac{\bar{e}_{3i}^{(l)} \bar{e}_{3j}^{(l)}}{\bar{Q}_{ij}^{(l)} \bar{\epsilon}_{33}^{(l)}}. \quad (2.19)$$

D_{ij}^* are modified membrane flexural stiffnesses, D_{ij}^{gl} is for the glass layer only, D_{ij}^{p} for the piezoelectric layer only and χ_{ij} is a correction factor to the membrane flexural stiffnesses due to the piezoelectric coupling within the piezoelectric material, as discussed for piezoelectric beams in [32].

2.7 Variational formulation

In this section, we describe mathematically the variational formulation, that is the core for electromechanical modeling of the piezoelectrically actuated MEMS tunable lenses. It has the following assumptions

1. Classical laminate plate theory which takes into account first order bending strains and neglects the normal strain S_{zz} and the transverse engineering strains γ_{xz} and γ_{yz} .
2. Linear theory of piezoelectricity that assumes a linear coupling between electric field components and strains.
3. The piezoelectric layer is a charge free region so that Gauss's law is simplified to $\nabla \cdot \mathbf{D} = 0$.
4. A thin film approximation which neglects the lack of smoothness at the transitions between areas that are covered by a piezoelectric thin film and those that are not. This approximation is made by using displacement ansatz that are continuous and differentiable over the whole diaphragm plane.

5. The soft polymer that is deformed by actuation of the diaphragm and is assumed to be weightless and do not to affect the diaphragm bending.

6. The deformation is mainly dominated by the transverse mid-plane displacement and the in-plane displacements v_0 and u_0 are negligible.

7. Electrostatic approximation of time-varying electric fields, which neglects electric fields originates from conduction currents. The identity $-\nabla V = \mathbf{E}$ holds valid for time varying fields, because piezoelectric materials are dielectrics with very low values of loss tangent.

8. The effect of platinum and adhesion layers on the lens displacement is neglected, because of their small thickness relatively to the PZT layer.

The Hamilton's principle for piezoelectric media from Eq. (2.3) can be rewritten as

$$\int_{t_0}^{t_1} \delta \Pi dt = \int_{t_0}^{t_1} \left(\delta K - \underbrace{(\delta U - \delta E)}_{\delta H} + \delta W \right) dt = 0. \quad (2.20)$$

The electric enthalpy, as previously discussed, has been replaced by $U - E$ [44]. δK , δU and δE are the virtual variation of kinetic, strain (or internal) and electric energies while δW is the virtual variation of external work applied to the system.

They can be defined as [42, 44]

$$\begin{aligned}\delta U &= \int_{\Omega} T_{ij} \delta S_{ij} dx dy dz \\ &= \int_{\Omega} (N_{xx} \delta S_{xx}^0 + M_{xx} \delta S_{xx}^1 + N_{yy} \delta S_{yy}^0 + M_{yy} \delta S_{yy}^1 + N_{xy} \delta \gamma_{xy}^0 + M_{xy} \delta \gamma_{xy}^1) dx dy,\end{aligned}\tag{2.21a}$$

$$\delta K = \int_{\Omega} \rho (\dot{u} \delta \dot{u} + \dot{v} \delta \dot{v} + \dot{w} \delta \dot{w}) dx dy dz,\tag{2.21b}$$

$$\delta W = \int_S (t_i \delta u_i - q \delta v) dS,\tag{2.21c}$$

$$\delta E = \int_{\Omega} (D_1 \delta E_1 + D_2 \delta E_2 + D_3 \delta E_3) dx dy dz,\tag{2.21d}$$

where ρ , q and t_i are the mass density, the surface charge per unit area and the surface traction ($i=1,2,3$) against the displacement field. By following the variational formulation assumptions and substituting with developed expressions for the stresses resultant and the variational strains, Eqs. (2.21) can be expressed as below in terms of mid-plane transverse displacement and voltage only.

$$\begin{aligned}
 \delta U = \int_{\Omega} \left\{ \left(\frac{B_{11}}{2} \left(\frac{\partial w_0}{\partial x} \right)^2 + \frac{B_{12}}{2} \left(\frac{\partial w_0}{\partial y} \right)^2 - D_{11}^* \frac{\partial^2 w_0}{\partial x^2} - D_{12}^* \frac{\partial^2 w_0}{\partial y^2} \right) \left(-\frac{\partial^2 \delta w_0}{\partial x^2} \right) \right. \\
 + \left(\frac{B_{12}}{2} \left(\frac{\partial w_0}{\partial x} \right)^2 + \frac{B_{22}}{2} \left(\frac{\partial w_0}{\partial y} \right)^2 - D_{12}^* \frac{\partial^2 w_0}{\partial x^2} - D_{22}^* \frac{\partial^2 w_0}{\partial y^2} \right) \left(-\frac{\partial^2 \delta w_0}{\partial y^2} \right) \\
 + \left(B_{66} \left(\frac{\partial w_0}{\partial x} \frac{\partial w_0}{\partial y} \right) - 2D_{66}^* \frac{\partial^2 w_0}{\partial x \partial y} \right) \left(-2 \frac{\partial^2 \delta w_0}{\partial x \partial y} \right) \\
 + \left(\frac{A_{11}}{2} \left(\frac{\partial w_0}{\partial x} \right)^2 + \frac{A_{12}}{2} \left(\frac{\partial w_0}{\partial y} \right)^2 - B_{11} \frac{\partial^2 w_0}{\partial x^2} - B_{12} \frac{\partial^2 w_0}{\partial y^2} \right) \left(\frac{\partial w_0}{\partial x} \frac{\partial \delta w_0}{\partial x} \right) \\
 + \left(\frac{A_{12}}{2} \left(\frac{\partial w_0}{\partial x} \right)^2 + \frac{A_{22}}{2} \left(\frac{\partial w_0}{\partial y} \right)^2 - B_{12} \frac{\partial^2 w_0}{\partial x^2} - B_{22} \frac{\partial^2 w_0}{\partial y^2} \right) \left(\frac{\partial w_0}{\partial y} \frac{\partial \delta w_0}{\partial y} \right) \\
 + \left(A_{66} \left(\frac{\partial w_0}{\partial x} \frac{\partial w_0}{\partial y} \right) - 2B_{66} \frac{\partial^2 w_0}{\partial x \partial y} \right) \left(\frac{\partial \delta w_0}{\partial x} \frac{\partial w_0}{\partial y} + \frac{\partial w_0}{\partial x} \frac{\partial \delta w_0}{\partial y} \right) \\
 + \left(\bar{e}_{31} V_p + \sum_{k=1}^{n_l} N_{xx}^{R,(k)} \right) \frac{\partial w_0}{\partial x} \frac{\partial \delta w_0}{\partial x} + \left(\bar{e}_{32} V_p + \sum_{k=1}^{n_l} N_{yy}^{R,(k)} \right) \frac{\partial w_0}{\partial y} \frac{\partial \delta w_0}{\partial y} \\
 + \left(\bar{e}_{36} V_p + \sum_{k=1}^{n_l} N_{xy}^{R,(k)} \right) \left(\frac{\partial \delta w_0}{\partial x} \frac{\partial w_0}{\partial y} + \frac{\partial w_0}{\partial x} \frac{\partial \delta w_0}{\partial y} \right) \\
 + \left(\bar{e}_{31} V_p \bar{z}_p + \sum_{k=1}^{n_l} M_{xx}^{R,(k)} \right) \left(-\frac{\partial^2 \delta w_0}{\partial x^2} \right) + \left(\bar{e}_{32} V_p \bar{z}_p + \sum_{k=1}^{n_l} M_{yy}^{R,(k)} \right) \left(-\frac{\partial^2 \delta w_0}{\partial y^2} \right) \\
 + \left. \left(\bar{e}_{36} V_p \bar{z}_p + \sum_{k=1}^{n_l} M_{xy}^{R,(k)} \right) \left(-2 \frac{\partial^2 \delta w_0}{\partial x \partial y} \right) \right\} dx dy, \quad (2.22)
 \end{aligned}$$

$$\delta K = \int_{\Omega} \left\{ I_0 \dot{w}_0 \delta \dot{w}_0 + I_2 (\dot{w}_{0,x} \delta \dot{w}_{0,x} + \dot{w}_{0,y} \delta \dot{w}_{0,y}) \right\} dx dy, \quad (2.23)$$

$$\delta W = \int_{\Gamma_{\Omega}} \left(\hat{M}_{nn} \frac{\partial \delta w_0}{\partial \hat{\mathbf{n}}} + \hat{M}_{ns} \frac{\partial \delta w_0}{\partial \hat{\mathbf{s}}} \right) ds + \int_{\Omega} (p \delta w_0 - q \delta v) ds, \quad (2.24)$$

where

$$(I_0, I_2) = \int (1, z^2) \rho dz. \quad (2.25)$$

\hat{M}_{nn} and \hat{M}_{ns} are normal and tangential external stress moments applied over the domain Ω 's outer boundary Γ_Ω , respectively. They depend on the type of supports that hold the tunable lens. For the clamped case, the first integral vanishes because of zero displacement and zero slope conditions at the edges. $\hat{\mathbf{n}}$ and $\hat{\mathbf{s}}$ are the normal and tangential unit vectors along the outer boundary Γ_Ω , respectively. p is the transverse pressure. The second integral is the external work due to a pressure force p , which vanishes based on having no external pressure and the assumption previously made that the polymer don't affect the membrane displacement.

$$\begin{aligned} \delta E &= - \int \mathbf{D} \cdot \nabla(\delta v) dx dy dz = - \int_S \mathbf{D} \delta v \cdot d\mathbf{S} + \int \delta v \underbrace{(\nabla \cdot \mathbf{D})}_{=0} dx dy dz \\ &= - \int_S \mathbf{D} \delta v \cdot d\mathbf{S}, \end{aligned} \quad (2.26)$$

where \mathbf{S} is the unit vector normal to the surface S . At either the top or the bottom surfaces of the piezoelectric layer, the electric displacement field D_3 must be equal to the surface charge density to satisfy the electric boundary conditions of zero normal component of the electric field inside the Pt electrodes. Thus, the variation in electric energy becomes

$$\delta E = - \int_S q \delta v dx dy, \quad (2.27)$$

and it cancels the electric term in δW expression. This cancellation is necessary and appears naturally from the variational formulation as discussed in [37].

Therefore, the variational formulation can be reduced to

$$\begin{aligned}
 & \int_{\Omega} \left\{ I_0 \dot{w}_0 \delta \dot{w}_0 + I_2 (\dot{w}_{0,x} \delta \dot{w}_{0,x} + \dot{w}_{0,y} \delta \dot{w}_{0,y}) \right\} dx dy \\
 & + \int_{\Omega} \left\{ \left(\frac{B_{11}}{2} \left(\frac{\partial w_0}{\partial x} \right)^2 + \frac{B_{12}}{2} \left(\frac{\partial w_0}{\partial y} \right)^2 - D_{11}^* \frac{\partial^2 w_0}{\partial x^2} - D_{12}^* \frac{\partial^2 w_0}{\partial y^2} \right) \left(\frac{\partial^2 \delta w_0}{\partial x^2} \right) \right. \\
 & + \left(\frac{B_{12}}{2} \left(\frac{\partial w_0}{\partial x} \right)^2 + \frac{B_{22}}{2} \left(\frac{\partial w_0}{\partial y} \right)^2 - D_{12}^* \frac{\partial^2 w_0}{\partial x^2} - D_{22}^* \frac{\partial^2 w_0}{\partial y^2} \right) \left(\frac{\partial^2 \delta w_0}{\partial y^2} \right) \\
 & + \left(B_{66} \left(\frac{\partial w_0}{\partial x} \frac{\partial w_0}{\partial y} \right) - 2D_{66}^* \frac{\partial^2 w_0}{\partial x \partial y} \right) \left(2 \frac{\partial^2 \delta w_0}{\partial x \partial y} \right) \\
 & + \left(\frac{A_{11}}{2} \left(\frac{\partial w_0}{\partial x} \right)^2 + \frac{A_{12}}{2} \left(\frac{\partial w_0}{\partial y} \right)^2 - B_{11} \frac{\partial^2 w_0}{\partial x^2} - B_{12} \frac{\partial^2 w_0}{\partial y^2} \right) \left(- \frac{\partial w_0}{\partial x} \frac{\partial \delta w_0}{\partial x} \right) \\
 & + \left(\frac{A_{12}}{2} \left(\frac{\partial w_0}{\partial x} \right)^2 + \frac{A_{22}}{2} \left(\frac{\partial w_0}{\partial y} \right)^2 - B_{12} \frac{\partial^2 w_0}{\partial x^2} - B_{22} \frac{\partial^2 w_0}{\partial y^2} \right) \left(- \frac{\partial w_0}{\partial y} \frac{\partial \delta w_0}{\partial y} \right) \\
 & - \left(A_{66} \left(\frac{\partial w_0}{\partial x} \frac{\partial w_0}{\partial y} \right) - 2B_{66} \frac{\partial^2 w_0}{\partial x \partial y} \right) \left(\frac{\partial \delta w_0}{\partial x} \frac{\partial w_0}{\partial y} + \frac{\partial w_0}{\partial x} \frac{\partial \delta w_0}{\partial y} \right) + \int_{\Omega} p \delta w_0 ds \\
 & - \left(\bar{e}_{31} V_p + \sum_{k=1}^{n_l} N_{xx}^{R,(k)} \right) \frac{\partial w_0}{\partial x} \frac{\partial \delta w_0}{\partial x} - \left(\bar{e}_{32} V_p + \sum_{k=1}^{n_l} N_{yy}^{R,(k)} \right) \frac{\partial w_0}{\partial y} \frac{\partial \delta w_0}{\partial y} \\
 & - \left(\bar{e}_{36} V_p + \sum_{k=1}^{n_l} N_{xy}^{R,(k)} \right) \left(\frac{\partial \delta w_0}{\partial x} \frac{\partial w_0}{\partial y} + \frac{\partial w_0}{\partial x} \frac{\partial \delta w_0}{\partial y} \right) \\
 & + \left(\bar{e}_{31} V_p \bar{z}_p + \sum_{k=1}^{n_l} M_{xx}^{R,(k)} \right) \left(\frac{\partial^2 \delta w_0}{\partial x^2} \right) + \left(\bar{e}_{32} V_p \bar{z}_p + \sum_{k=1}^{n_l} M_{yy}^{R,(k)} \right) \left(\frac{\partial^2 \delta w_0}{\partial y^2} \right) \\
 & + \left. \left(\bar{e}_{36} V_p \bar{z}_p + \sum_{k=1}^{n_l} M_{xy}^{R,(k)} \right) \left(2 \frac{\partial^2 \delta w_0}{\partial x \partial y} \right) \right\} dx dy = 0. \tag{2.28}
 \end{aligned}$$

The above formulation is the typical one would have for pure elastic media except for the last six additional terms that depend on the piezoelectric coupling and residual stresses. The first three of these six terms modify the equivalent linear stiffness matrix while the last three form the equivalent force matrix.

2.8 Displacement ansatz and equation of motions

All energies are currently expressed in terms of the mid-plane displacement in z -direction. To solve the variational formulation for w_0 , we write an approximate solution w_N as a finite linear combination of basis functions

$$w_0(X, Y) \approx w_N(X, Y) = \sum_{k=1}^{N_r} C_k(t) \Phi_k(X, Y), \quad (2.29)$$

where $\Phi_k(X, Y)$ are the basis functions and C_k are their coefficients that depend on time and to be determined. X and Y are the normalized cartesian coordinates. N_r is the number of basis functions and is increased until convergence is attained over mechanical and optical parameters. The choice of basis functions is an important part of the ansatz. They must satisfy the mechanical boundary conditions. By substituting with Eq. (2.29) in the variational formulation, the Euler-Lagrange equations of motion become

$$\frac{d}{dt} \left(\frac{\partial \Pi}{\partial \dot{\mathbf{C}}} \right) - \frac{\partial \Pi}{\partial \mathbf{C}} = 0, \quad (2.30)$$

where \mathbf{C} is a vector of the coefficients C_k (*i.e.* the state vector). In Einstein notation, the resultant system of equations due to von Kármán strains can be written as

$$\left(R_{k_1 k_2} + R_{k_1 k_2}^N \right) C_{k_1} + R_{k_1 k_2 k_3} C_{k_1} C_{k_2} + R_{k_1 k_2 k_3 k_4} C_{k_1} C_{k_2} C_{k_3} + M_{k_1 k_2} \ddot{C}_{k_1} - F_{k_2} = 0. \quad (2.31)$$

It is obvious that the equations of motion are cubic in terms of the basis function coefficients. The linear stiffness has two term; the first term $R_{k_1k_2}$ is the linear stiffness one would have without geometric nonlinearity and the second term $R_{k_1k_2}^N$ is modifying the linear stiffness as a contribution of the residual stresses and the piezoelectric coupling due to the nonlinear deformation. The $R_{k_1k_2k_3}$ and $R_{k_1k_2k_3k_4}$ are the quadratic and cubic stiffness terms resulting from including the dominant term of stretching strains due to the transverse displacement w_0 . The term $M_{k_1k_2}$ represents the equivalent mass while the last term F_{k_2} represents the equivalent force due to piezoelectric coupling and residual stresses. For modeling the lens dynamics, a damping term $\zeta_{k_1k_2}\dot{C}_{k_1}$ will be added to Eq. 2.31 to represent a damping mechanism. The terms from Eq. 2.31 are respectively defined below for the cartesian and polar lens's subdomains.

$$\begin{aligned}
 R_{k_1 k_2} = & \frac{1}{(a/2)^2} \int_{\Omega} \left\{ (D_{11}^* \Phi_{k_1, XX} + D_{12}^* \Phi_{k_1, YY}) \Phi_{k_2, XX} \right. \\
 & + (D_{12}^* \Phi_{k_1, XX} + D_{22}^* \Phi_{k_1, YY}) \Phi_{k_1, YY} \\
 & \left. + 4D_{66}^* \Phi_{k_1, XY} \Phi_{k_2, XY} \right\} dXdY, \quad (2.32a)
 \end{aligned}$$

$$\begin{aligned}
 R_{k_1 k_2}^N = & \int_{\Omega} \left\{ \left(\bar{e}_{31} V_p + \sum_{k=1}^{n_l} N_{xx}^{R, (k)} \right) \Phi_{k_1, X} \Phi_{k_2, Y} + \left(\bar{e}_{31} V_p + \sum_{k=1}^{n_l} N_{yy}^{R, (k)} \right) \Phi_{k_1, Y} \Phi_{k_2, Y} \right. \\
 & \left. + \left(\bar{e}_{36} V_p + \sum_{k=1}^{n_l} N_{xy}^{R, (k)} \right) (\Phi_{k_1, Y} \Phi_{k_2, X} + \Phi_{k_1, X} \Phi_{k_2, Y}) \right\} dXdY, \quad (2.32b)
 \end{aligned}$$

$$\begin{aligned}
 R_{k_1 k_2 k_3} = & \frac{1}{(a/2)^2} \int_{\Omega} \left\{ - \left(\frac{B_{11}}{2} \Phi_{k_1, X} \Phi_{k_2, X} + \frac{B_{12}}{2} \Phi_{k_1, Y} \Phi_{k_2, Y} \right) \Phi_{k_3, XX} \right. \\
 & - \left(\frac{B_{12}}{2} \Phi_{k_1, X} \Phi_{k_2, X} + \frac{B_{22}}{2} \Phi_{k_1, Y} \Phi_{k_2, Y} \right) \Phi_{k_3, YY} \\
 & - 2B_{66} \Phi_{k_1, X} \Phi_{k_2, Y} \Phi_{k_3, XY} - (B_{11} \Phi_{k_1, XX} + B_{12} \Phi_{k_1, YY}) \Phi_{k_3, X} \Phi_{k_3, X} \\
 & - (B_{12} \Phi_{k_1, XX} + B_{22} \Phi_{k_1, YY}) \Phi_{k_3, Y} \Phi_{k_3, Y} \\
 & \left. - 2B_{66} \Phi_{k_1, XY} (\Phi_{k_2, Y} \Phi_{k_3, X} + \Phi_{k_3, X} \Phi_{k_2, Y}) \right\} dXdY, \quad (2.32c)
 \end{aligned}$$

$$\begin{aligned}
 R_{k_1 k_2 k_3 k_4} = & \frac{1}{(a/2)^2} \int_{\Omega} \left\{ \left(\frac{A_{11}}{2} \Phi_{k_1, X} \Phi_{k_2, X} + \frac{A_{12}}{2} \Phi_{k_1, Y} \Phi_{k_2, Y} \right) \Phi_{k_3, X} \Phi_{k_4, X} \right. \\
 & + \left(\frac{A_{12}}{2} \Phi_{k_1, X} \Phi_{k_2, X} + \frac{A_{22}}{2} \Phi_{k_1, Y} \Phi_{k_2, Y} \right) \Phi_{k_3, Y} \Phi_{k_4, Y} \\
 & \left. + A_{66} \Phi_{k_1, X} \Phi_{k_2, Y} (\Phi_{k_3, Y} \Phi_{k_4, X} + \Phi_{k_3, X} \Phi_{k_4, Y}) \right\} dXdY, \quad (2.32d)
 \end{aligned}$$

$$\begin{aligned}
 F_{k_2} = & \int_{\Omega} \left\{ \left(\bar{e}_{31} V_p \bar{z}_p + \sum_{k=1}^{n_l} M_{xx}^{R, (k)} \right) \Phi_{k_2, XX} + \left(\bar{e}_{31} V_p \bar{z}_p + \sum_{k=1}^{n_l} M_{yy}^{R, (k)} \right) \Phi_{k_2, YY} \right. \\
 & \left. + 2 \left(\bar{e}_{36} V_p \bar{z}_p + \sum_{k=1}^{n_l} M_{xy}^{R, (k)} \right) \Phi_{k_2, XY} \right\} dXdY,
 \end{aligned}$$

$$\begin{aligned}
 M_{k_1 k_2} = & \int_{\Omega} \left\{ (a/2)^2 I_0 \Phi_{k_1} \Phi_{k_2} + I_2 (\Phi_{k_1, X} \Phi_{k_2, X} + \Phi_{k_1, Y} \Phi_{k_2, Y}) \right\} dXdY, \\
 & (2.32e)
 \end{aligned}$$

$$\begin{aligned}
 R_{k_1 k_2} = & \frac{1}{\gamma_0^2 (a/2)^2} \int_{\Omega} \left\{ \left(D_{11}^* \tilde{\Phi}_{k_1, rr} + D_{12}^* \left(\frac{1}{r} \tilde{\Phi}_{k_1, r} + \frac{1}{r^2} \tilde{\Phi}_{k_2, \theta\theta} \right) \right) \tilde{\Phi}_{k_1, rr} \right. \\
 & + \left(D_{12}^* \tilde{\Phi}_{k_1, rr} + D_{22}^* \left(\frac{1}{r} w_{0, r} + \frac{1}{r^2} \tilde{\Phi}_{k_1, \theta\theta} \right) \right) \left(\frac{1}{r} \tilde{\Phi}_{k_2, r} + \frac{1}{r^2} \tilde{\Phi}_{k_2, \theta\theta} \right) \\
 & \left. + 4D_{66}^* \left(\frac{1}{r} \tilde{\Phi}_{k_1, r\theta} - \frac{1}{r^2} \tilde{\Phi}_{k_1, \theta} \right) \left(\frac{1}{r} \tilde{\Phi}_{k_2, r\theta} - \frac{1}{r^2} \tilde{\Phi}_{k_2, \theta} \right) \right\} r dr d\theta, \quad (2.33a)
 \end{aligned}$$

$$\begin{aligned}
 R_{k_1 k_2}^N = & \int_{\Omega} \left\{ \left(\bar{e}_{31} V_p + \sum_{k=1}^{n_l} N_{rr}^{R, (k)} \right) \tilde{\Phi}_{k_1, r} \tilde{\Phi}_{k_2, r} \right. \\
 & + \left(\bar{e}_{32} V_p + \sum_{k=1}^{n_l} N_{\theta\theta}^{R, (k)} \right) \frac{1}{r^2} \tilde{\Phi}_{k_1, \theta} \tilde{\Phi}_{k_2, \theta} \\
 & \left. + \left(\bar{e}_{36} V_p + \sum_{k=1}^{n_l} N_{r\theta}^{R, (k)} \right) \left(\frac{1}{r} \tilde{\Phi}_{k_1, r} \tilde{\Phi}_{k_2, \theta} + \frac{1}{r} \tilde{\Phi}_{k_2, r} \tilde{\Phi}_{k_1, \theta} \right) \right\} r dr d\theta, \quad (2.33b)
 \end{aligned}$$

$$\begin{aligned}
 R_{k_1 k_2 k_3} = & \frac{1}{\gamma_0^2 (a/2)^2} \int_{\Omega} \left\{ - \left(\frac{B_{11}}{2} \tilde{\Phi}_{k_1, r} \tilde{\Phi}_{k_2, r} + \frac{B_{12}}{2} \frac{1}{r^2} \tilde{\Phi}_{k_1, \theta} \tilde{\Phi}_{k_2, \theta} \right) \tilde{\Phi}_{k_3, rr} \right. \\
 & - \left(\frac{B_{12}}{2} \tilde{\Phi}_{k_1, r} \tilde{\Phi}_{k_2, r} + \frac{B_{22}}{2} \frac{1}{r^2} \tilde{\Phi}_{k_1, \theta} \tilde{\Phi}_{k_2, \theta} \right) \left(\frac{1}{r} \tilde{\Phi}_{k_3, r} + \frac{1}{r^2} \tilde{\Phi}_{k_3, \theta\theta} \right) \\
 & - 2B_{66} \frac{1}{r^2} \tilde{\Phi}_{k_1, r} \tilde{\Phi}_{k_2, \theta} \left(\tilde{\Phi}_{k_3, r\theta} - \frac{1}{r} \tilde{\Phi}_{k_3, \theta} \right) \\
 & - \left(\frac{B_{11}}{2} \tilde{\Phi}_{k_1, rr} + \frac{B_{12}^*}{2} \left(\frac{1}{r} w_{0, r} + \frac{1}{r^2} \tilde{\Phi}_{k_1, \theta\theta} \right) \right) \tilde{\Phi}_{k_2, r} \tilde{\Phi}_{k_3, r} \\
 & - \left(\frac{B_{12}}{2} \tilde{\Phi}_{k_1, rr} + \frac{B_{22}}{2} \left(\frac{1}{r} \tilde{\Phi}_{k_1, r} + \frac{1}{r^2} \tilde{\Phi}_{k_1, \theta\theta} \right) \right) \frac{1}{r^2} \tilde{\Phi}_{k_2, \theta} \tilde{\Phi}_{k_3, \theta} \\
 & \left. - 2B_{66} \left(\frac{1}{r} \tilde{\Phi}_{k_1, r\theta} - \frac{1}{r^2} \tilde{\Phi}_{k_1, \theta} \right) \left(\frac{1}{r} \tilde{\Phi}_{k_3, r\theta} - \frac{1}{r^2} \tilde{\Phi}_{k_3, \theta} \right) \right\} r dr d\theta, \quad (2.33c)
 \end{aligned}$$

$$\begin{aligned}
 R_{k_1 k_2 k_3 k_4} = & \frac{1}{\gamma_0^2 (a/2)^2} \int_{\Omega} \left\{ \left(\frac{A_{11}}{2} \tilde{\Phi}_{k_1, r} \tilde{\Phi}_{k_2, r} + \frac{A_{12}}{2r^2} \tilde{\Phi}_{k_1, \theta} \tilde{\Phi}_{k_2, \theta} \right) \tilde{\Phi}_{k_3, r} \tilde{\Phi}_{k_4, r} \right. \\
 & + \left(\frac{A_{11}}{2} \tilde{\Phi}_{k_1, r} \tilde{\Phi}_{k_2, r} + \frac{A_{12}^*}{2r^2} \tilde{\Phi}_{k_1, \theta} \tilde{\Phi}_{k_2, \theta} \right) \frac{1}{r^2} \tilde{\Phi}_{k_3, \theta} \tilde{\Phi}_{k_4, \theta} \\
 & \left. + A_{66} \frac{1}{r} \tilde{\Phi}_{k_1, r} \tilde{\Phi}_{k_2, \theta} \left(\frac{1}{r} \tilde{\Phi}_{k_3, r} \tilde{\Phi}_{k_4, \theta} + \frac{1}{r} \tilde{\Phi}_{k_4, r} \tilde{\Phi}_{k_3, \theta} \right) \right\} dr d\theta, \quad (2.33d)
 \end{aligned}$$

$$\begin{aligned}
 F_{k_2} = \int_{\Omega} \left\{ \left(\bar{e}_{31} V_p \bar{z}_p + \sum_{k=1}^{n_l} M_{rr}^{R,(k)} \right) \tilde{\Phi}_{k_2,rr} + \left(\bar{e}_{31} V_p \bar{z}_p + \sum_{k=1}^{n_l} M_{\theta\theta}^{R,(k)} \right) \frac{1}{r^2} \tilde{\Phi}_{k_2,\theta\theta} \right. \\
 \left. + 2 \left(\bar{e}_{36} V_p \bar{z}_p + \sum_{k=1}^{n_l} M_{r\theta}^{R,(k)} \right) \left(\frac{1}{r} \tilde{\Phi}_{k_2,r\theta} - \frac{1}{r^2} \tilde{\Phi}_{k_2,\theta} \right) \right\} dXdY, \quad (2.33e)
 \end{aligned}$$

$$M_{k_1 k_2} = \int_{\Omega} \left\{ \gamma_0^2 (a/2)^2 I_0 \tilde{\Phi}_{k_1} \tilde{\Phi}_{k_2} + I_2 \left(\tilde{\Phi}_{k_1,r} \tilde{\Phi}_{k_2,r} + \frac{1}{r^2} \tilde{\Phi}_{k_1,\theta} \tilde{\Phi}_{k_2,\theta} \right) \right\} dXdY. \quad (2.33f)$$

If Kirchhoff plate theory is considered to approximate strains, Eq. (2.31) is reduced to the following linear system of equation

$$R_{k_1 k_2} C_{k_1} + M_{k_1 k_2} \ddot{C}_{k_1} - F_{k_2} = 0. \quad (2.34)$$

Based on the next chapters' context, static and dynamic versions of Eqs.(2.31) and (2.34) are used in the electromechanical part of the modeling framework that predicts the optoelectromechanical performance of the piezoelectrically actuated MEMS tunable lenses.

3 Modeling framework for piezoelectrically actuated MEMS tunable lenses with various pupil geometries

This chapter investigates the effect of having different shapes of piezoelectric actuators on the lens optical performance. A search has been conducted for a design space of the actuator's geometrical parameters, that could achieve higher focusing capability without increasing RMS-wavefront error that reduces image quality. Thus, a modeling framework has been developed for evaluating the performance of piezoelectrically actuated MEMS tunable lenses. It models the static optoelectromechanical coupling for symmetric configurations of d_{31} piezoelectric actuators. This helps finding geometrical parameters for actuators that give a diffraction limited tunable lens with minimum F-number. The modeling framework has two major parts. Its first part is to model the static electromechanical performance and is verified against FEM with an error criterion. The second part is to investigate quantitatively the tunable lens's optical performance using ray tracing by analyzing its F -number ($F\#$), RMS wavefront error (RMSWFE) and Modulation Transfer Function (MTF). The tunable lens' optical performance and its focusing capability, alone and in combination with a fixed lens, have been cal-

culated in terms of object distance and actuation voltage. Using the modeling framework, we have confirmed that the MTF for objects located at different distances remains the same within a limited Field of View (FoV) after voltage adjustment to refocus at near objects.

Section 3.1 introduces the linear variation formulation and discusses the integration mask (*the complementary pupil function*) that allows moving around the difficulty of calculating the variational integrals over lens' subdomains. Then, section 3.2 presents the displacement ansatz and reasons for their suitability in the optoelectromechanical modeling of the tunable lens. Section 3 investigates the variational and FEM solutions for tunable lenses with various polygonal pupil geometries. At the end, it discusses the optical performance of the different lenses and investigates the design concept of pupil masking.

3.1 The linear variational formulation

The core of our modeling framework for square diaphragms is a weak formulation (*i.e.* Eq. (2.32)) based on the assumptions mentioned in Sec. 2.7. In addition, we here assume quasi-static conditions such that there is no time dependence. Thus, the weak formulation can be reduced to

$$\int_{\Omega} \left\{ \left(D_{11}^* \frac{\partial^2 w_0}{\partial x^2} + D_{12}^* \frac{\partial^2 w_0}{\partial y^2} \right) \left(\frac{\partial^2 \delta w_0}{\partial x^2} \right) + \left(D_{12}^* \frac{\partial^2 w_0}{\partial x^2} + D_{22}^* \frac{\partial^2 w_0}{\partial y^2} \right) \left(\frac{\partial^2 \delta w_0}{\partial y^2} \right) + \left(2D_{66}^* \frac{\partial^2 w_0}{\partial x \partial y} \right) \left(2 \frac{\partial^2 \delta w_0}{\partial x \partial y} \right) \right\} dx dy = \bar{e}_{31} V_p \bar{z}_p \int_{\Omega_p} \nabla_{x,y}^2 \delta w_0 dx dy, \quad (3.1)$$

where $\Omega = \Omega_{gl} \cup \Omega_p$. Ω_{gl} and Ω_p are domains for glass and piezoelectric layers, respectively. $\nabla_{x,y}^2$ is the 2-D Laplace differential operator, which can be ex-

pressed in normalized cartesian or polar coordinates according to the shape of the domain. The quantities D_{ij}^* expression vary over the plate due to the difference in layer structure between the lens pupil and the actuator area. To simplify numerical integration, they can be expressed in a more general form

$$D_{ij}^* = D_{ij}^{gl} + D_{ij}^p \bar{\zeta}(X, Y) \quad (3.2)$$

where D_{ij}^{gl} is the flexural rigidity for the glass layer only, D_{ij}^p is for piezoelectric layer including the piezoelectric coupling within the piezoelectric material. $X = x/(a/2)$ and $Y = y/(a/2)$ are the normalized Cartesian coordinates. The complementary pupil function $\bar{\zeta}(X, Y)$ is 0 over the opening and 1 elsewhere. From Eq. (3.2), the quantities D_{ij}^* vary over the plate due to the difference in layer structure between the lens pupil and the actuator areas. The function $\bar{\zeta}$ serves as an integration mask in Eq. (3.2) allowing numerical calculations of the variational integrals to treat various pupil geometries on the same footing. This would be equivalent to calculating the energy terms for a square diaphragm, then, subtracting the energy terms for the pupil domain.

3.2 Displacement ansatz and its suitability for the optoelectromechanical modeling

To solve Eq. (3.1) for the deflection w_0 , we write an approximate solution w_N as a finite linear combination of basis functions

$$w_0(X, Y, 0) \approx w_N(X, Y, 0) = \sum_{m=1}^N \sum_{n=1}^N C_{mn} \Phi_{mn}(X, Y), \quad (3.3)$$

where $\Phi_{mn}(X, Y)$ are the basis functions and C_{mn} are coefficients to be determined. The choice of basis functions is an important part of the ansatz. They must satisfy the mechanical boundary conditions. In addition, they should preferably be orthogonal and easy to be mapped to Zernike polynomials [45]. Zernike polynomials are orthogonal polynomials over a disc and are convenient for optical representation of wavefronts. Orthogonality of the basis functions helps eliminating the possibility of a numerically ill-conditioned system of equations arising from the variational treatment. There are many options for the bases, such as products of trigonometric and hyperbolic functions [46] known for doubly-clamped beam or products of squared cosines [47]. The disadvantage of the latter functions is that they are not orthogonal. Moreover, for either of these choices, power series expansions of the basis functions in terms X and Y must be made in order to map to Zernike polynomials. This expansion increases the calculational burden necessary to avoid significant errors from the mapping. Thus, we propose a weighted product of Gegenbauer [48] polynomials on the interval $[-1, 1]$. They are orthogonal and have a simple mapping to Zernike polynomials as will be discussed later. By using projection, these basis functions can be written in terms of Zernike polynomials as

$$\Phi_{mn}(X, Y) = \phi_m(X)\phi_n(Y) = \underbrace{(1 - X^2)^{\frac{(\alpha-1/2)}{2}}(1 - Y^2)^{\frac{(\alpha-1/2)}{2}}}_{\text{Weight factor enforcing BC}} G_m^{(\alpha)}(X)G_n^{(\alpha)}(Y), \quad (3.4)$$

where $G_m^{(\alpha)}(X)$ is a Gegenbauer polynomial of order m and the parameter α in the weighting factor should equal $9/2$ to force the basis functions to satisfy the clamped boundary conditions of zero deflection and zero slope along the edges. Due to the symmetry, we have considered even polynomials, i.e. only functions with both indices m and n even. Figure 3.1 shows the x-cross section of the first six even basis functions of weighted Gegenbauer polynomials $\phi_m(X)$. By back-

substituting from Eq. (3.3) in Eq. (3.1), we get a linear system of equations for C_{mn} on the form [42]:

$$\underbrace{[R_{mnpq}]}_{N^2 \times N^2} \underbrace{[C_{mn}]}_{N^2 \times 1} = \underbrace{[F_{pq}]}_{N^2 \times 1}, \quad (3.5)$$

where $[R_{mnpq}]$ and $[F_{pq}]$ are calculated using the decomposition described above.

The products of finite order Gegenbauer polynomials inside a circle of radius $\gamma = 2c/a$ can be expressed as a linear combination of Zernike polynomials with coefficients depending on the geometrical parameter γ . The basis functions can be put on the form

$$\Phi_{mn}(r, \theta) = \sum_{i=0}^{N_s} \sum_{j=0}^{N_s} k_{mni j}(\gamma) Z_i^j(r, \theta), \quad (3.6)$$

where

$$k_{ijmn}^2 = \frac{1}{\mu_j \pi} \int_0^{2\pi} \int_0^1 \Phi_{mn}(\gamma r \cos(\theta), \gamma r \sin(\theta)) Z_i^j(r, \theta) r dr d\theta. \quad (3.7)$$

Z_i^j are Zernike polynomials of the order (i, j) . $N_s = m + n + 8$ is the order of Zernike polynomials sufficient for mapping exactly, where m, n are the orders of the basis function Φ_{mn} . μ_j is Neumann factor that equals 2 if $j = 0$ and 1 otherwise. Appendix B lists few examples on how are the Weighted Gegenbauer polynomials being expanded by Zernike polynomials. Moreover, based on the mirror symmetries of the problem under study, we note that we have only even Zernike-polynomial terms in the expansion. Due to this feature, we have an exact representation of the lens surface in terms of Zernike polynomials.

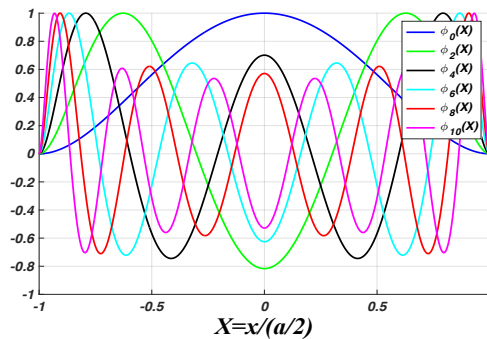


Figure 3.1: Even Gegenbauer-polynomial basis functions $\phi_m(X)$ on $[-1, 1]$.

3.3 Variational solutions versus FEM

3.3.1 Circular pupils

Figure 3.2 shows a planar view of two possible study cases for the tunable lenses. For all cases, light should only pass through the circular opening. Thus, case II with ring actuators has an additional opaque area (*i.e.* the lower Pt electrode of the piezoelectric stack) covering the diaphragm outside the actuator perimeter till the diaphragm edge in order to block out light.

In the analyzed study cases, we have used the same material and structure dimensions for the square diaphragm and the piezoelectric actuator stack as in Ref. 49.

Figure 3.3a shows how the variational solutions for case I match with FEM simulations. To check the convergence of the variational solution to the FEM solution

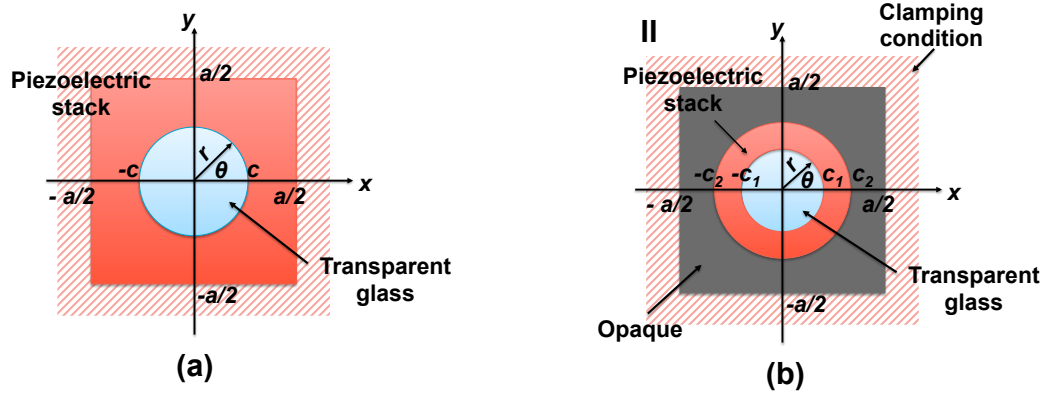


Figure 3.2: Planar view of possible study cases of piezoelectrically actuated MEMS tunable lenses. A clamped square diaphragm with circular opening: (a) case I and (b) case II ring actuator with opaque covering outside the ring till the diaphragm edges.

w_{FEM} , we choose to monitor the l_2 relative error norm

$$\Xi_{l_2} = \sqrt{\frac{\sum (w_{FEM} - w_N)^2}{\sum w_{FEM}^2}}. \quad (3.8)$$

As shown in Fig. 3.3b, the error and convergence speed both depend on the ratio γ . It is evident from Fig. 3.4 that the variational solutions in case II have similar behaviour as the FEM results, but the error is larger than for case I. The thin-film approximation allows us to use one set of continuous basis functions over the entire square diaphragm.

For the case-I actuator, this basis is artificially smooth at the rim of the glass opening where the layer structure changes from glass only to glass and piezoelectric. For the case-II actuator, we have this feature both at the inner and outer perimeter of the piezoelectric ring. The basis here do not account for the structure discontinuity which mandates having very large N to reach a decent accuracy for optical representation of the lens sag for optical simulations. Consequently, these basis are to be modified in chapter 4 in a way to account for this disconti-

nuity.

As shown in Fig. 3.4b, it is apparent that having $\gamma_2 \leq 0.5$ for case II, the displacement in the circular aperture area becomes nearly flat and it becomes a poor refractive surface unable to add any optical power to the passing light. Such behaviour is suitable to operate the structure as a piston micromirror as in [50].

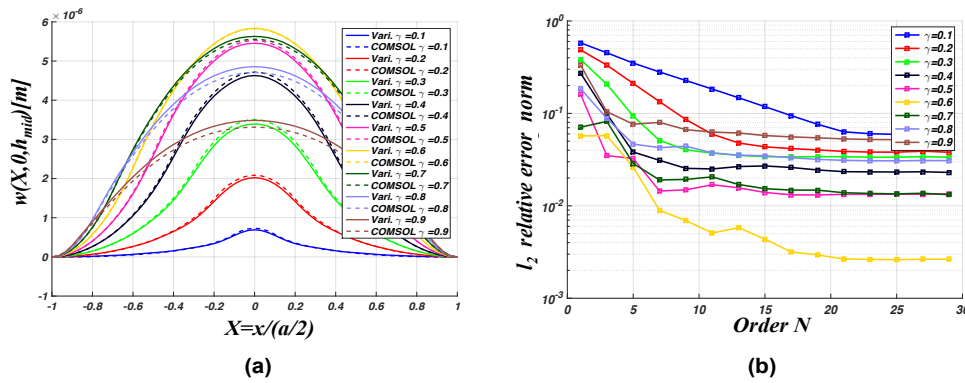


Figure 3.3: (a) Displacement profiles in xz -plane from FEM and the variational tool ($N = 28$) for square diaphragm with case I actuator at different values of ratio γ for piezoelectric material at $V_p = -10V$. (b) l_2 relative error norm versus polynomial order N .

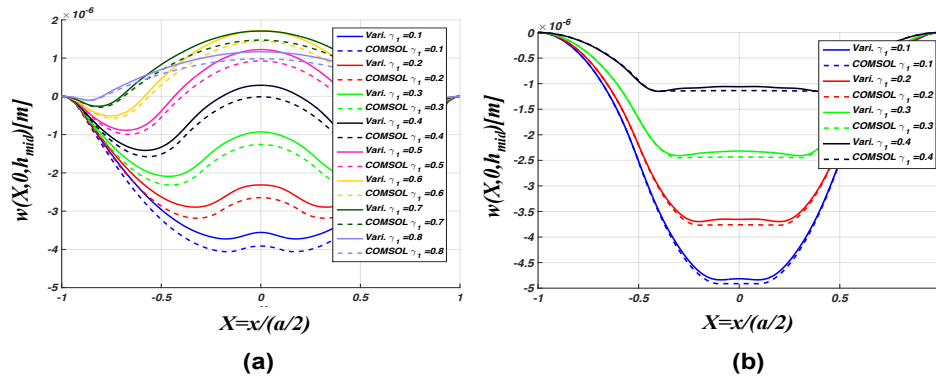


Figure 3.4: Displacement profiles in xz -plane from FEM and the variational tool ($N = 28$) for square diaphragm with case II actuator at different values of ratio $\gamma_1 = 2c_1/a$ when $\gamma_2 = 2c_2/a$ equals (a) 0.9 and (b) 0.5 at $V_p = -10V$.

3.3.2 Various pupil geometries

The variational formulation for tunable lenses can be amended to account for actuators with more complicated geometries than those in section 3.3.1. It can predict the deformation caused by piezoelectric actuators with arbitrary openings; but symmetric. Testing the advantages of non-circular pupil geometry, we have investigated the optical performance of polygon-shaped openings taking case I (from Sec. 3.3.1) as a reference for comparison. However, case I is named here as case 6. Figure 3.5 shows a planar view of symmetric actuator configurations for tunable lenses with different pupil geometries. The geometrical parameter γ for each pupil's actuator is here redefined as the ratio L_r/a , where L_r is the reference dimension marked by red arrows in Fig. 3.5. Specifically in case 6, L_r equals its circular opening diameter $2c$. For all study cases, the light passes only through the pupil opening area.

Figure 3.6 shows how the variational solutions (with $N=28$) for all cases match with FEM simulations. For all cases, with all γ values of interest, $N = 28$ is sufficient to obtain less than 10 % l_2 relative error norm when comparing the displacement from the variational solution with FEM. Thus, they qualitatively provide good prediction for deflection to be used subsequently in optical simulations.

The presented modeling framework provides a fast tool, compared to FEM, to perform optimization and exploration of different materials, layer thicknesses and pupil geometries. For example, on our computer (Intel i7-4940MX, 3.1 GHz, 64-bit OS) the software package MATLAB [5] solves Eq. (3.5) in 1.3 seconds while it takes 1.5 minutes to solve the corresponding problem with FEM (using COMSOL Multiphysics v4.4 [6]).

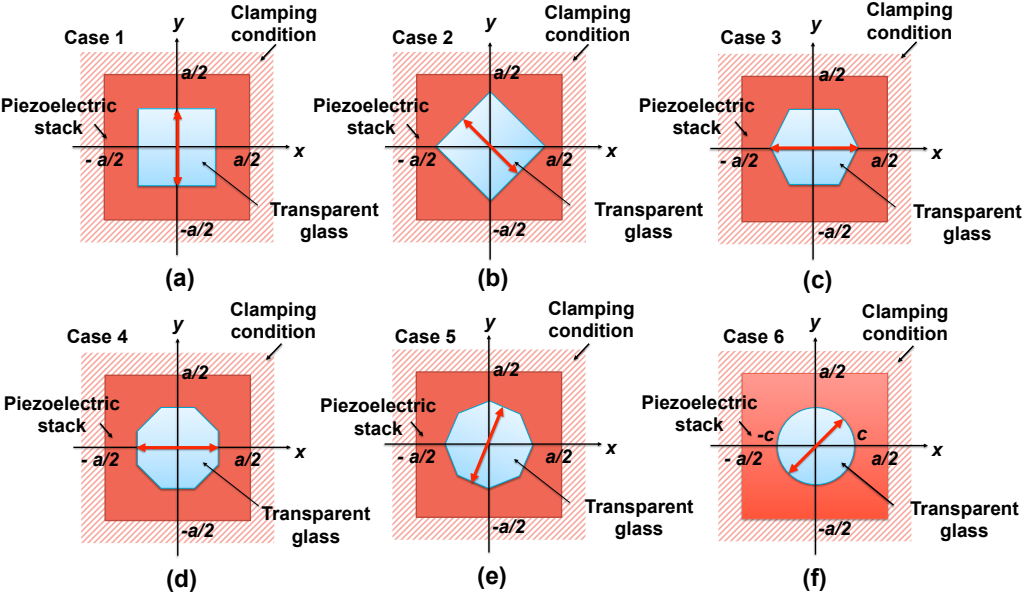


Figure 3.5: Planar view of possible study cases of piezoelectrically-actuated tunable lenses. A clamped square diaphragm with: (a) square, (b) 45° rotated square, (c) hexagonal, (d) octagonal, (e) 22.5° rotated octagonal and (f) circular pupils. The red arrows indicate the reference dimension L_r for each pupil.

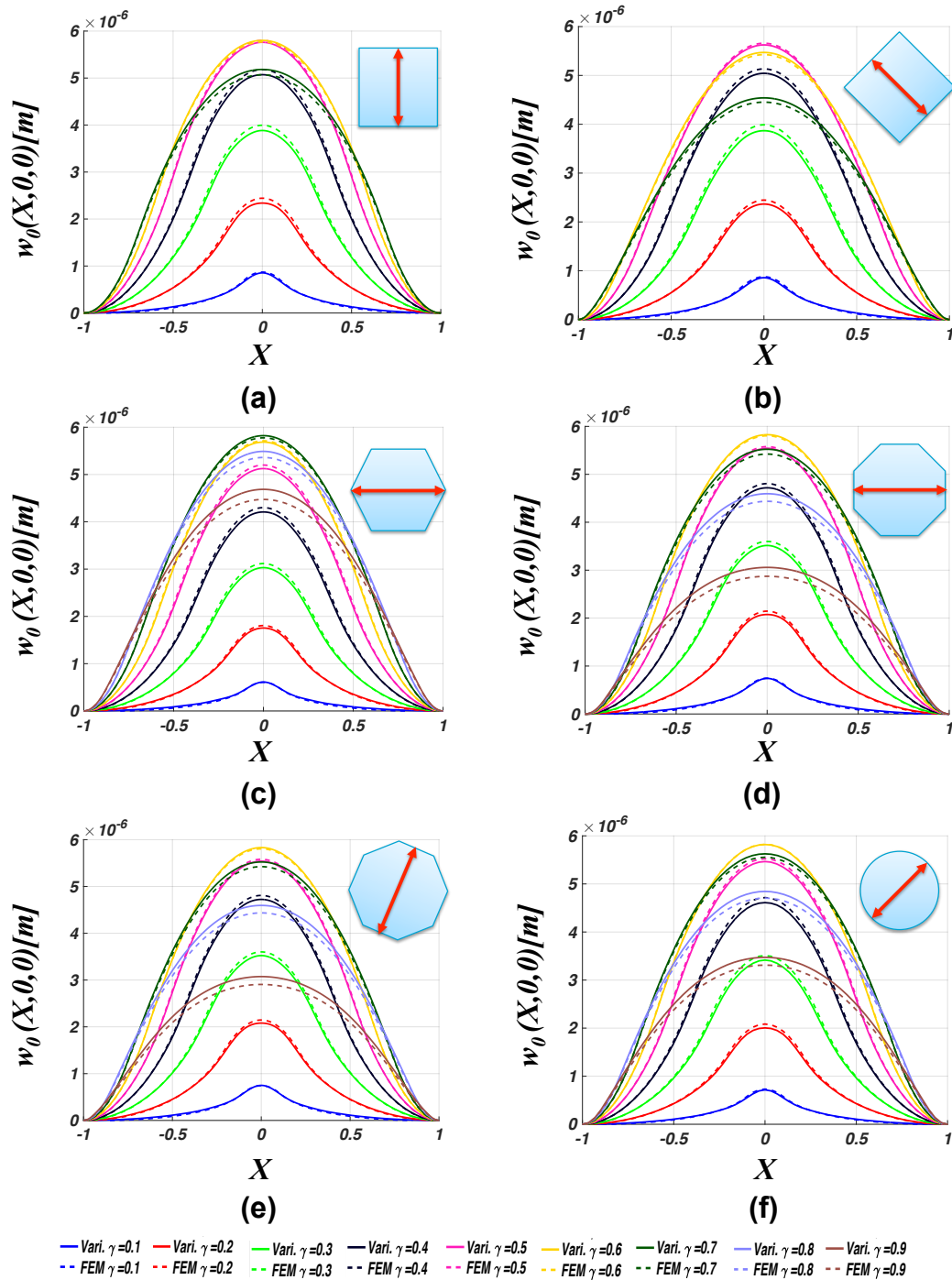


Figure 3.6: Displacement profiles in xz -plane from FEM simulations and the variational solutions ($N = 28$) for a clamped square diaphragm with (a) square, (b) 45° rotated square, (c) hexagonal, (d) octagonal, (e) 22.5° rotated octagonal and (f) circular pupils at different γ ratios with $V_p = -10V$.

3.3.3 Optical performance using ray tracing analysis

The lens sag from both the variational solutions and FEM simulation have been exported to Zemax [7] in which optical simulations are done using ray tracing analysis [33, 49]. The geometrical parameters of the lens' actuator have been optimized to achieve the minimum achievable $F\#$ while having an acceptable RMS-wavefront-error (RMSWFE) to have a diffraction-limited performance. According to Maréchal's criterion [25], the RMSWFE should be $\leq \lambda/14$ to avoid the deviation from diffraction-limited performance.

F-number is defined as $F\# = f / (\sqrt{\frac{4}{\pi}A})$, where f is the focal length and A is the pupil area. The on-axis wavefront error (WFE) is the optical path difference between the constant phase surface of the wave coming out of the lens and a reference sphere having its center at the image plane and its radius equal to the separating distance between lens exit pupil and the image plane [7].

The optical performance of case II actuator has not been superior to case I (or case 6) which achieves the minimum $F\#$; the reader may refer to [49]) for the optical performance of case II. Among different actuator geometries [33, 49], case 6 with the circular pupil has the widest aperture area with an area factor 0.26 compared to the square diaphragm area (refer to Fig. 3.7 and Tab. 3.1). It achieves nearly 4.5 diopters with a 10-V voltage source and has an RMS wavefront error less than the Maréchal's criterion.

To study the tunable lens at the system level, such as for smartphone camera application, we combine it with a fixed lens [33] as shown in Fig. 3.8a. Their combination enables us to put an object at different focus positions from the camera, refocus by adjusting the actuation voltage on the tunable lens, and calculate the overall MTF at the image plane. Over the focusing range, the overall MTF is de-

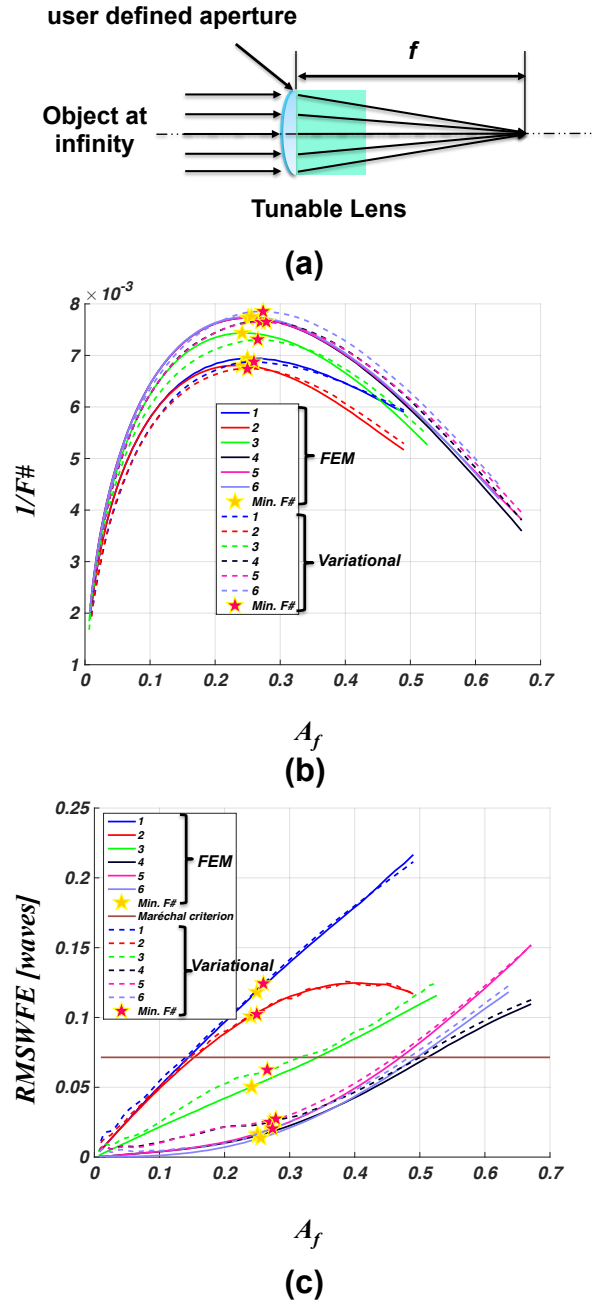


Figure 3.7: (a) Tunable lens arrangement for on-axis optical simulations. (b) Reciprocal $F\#$ and (c) RMSWFE versus the area factor A_f for different pupils using variational solutions and FEM simulations, all with $V_p = -10V$ and $\lambda = 550nm$. The numbers 1 to 6 respectively represent lenses with square, 45-rotated square, hexagonal, octagonal, 22.5-rotated octagonal and circular pupils, respectively.

Table 3.1: Optimum γ_v^* and γ_{FEM}^* ratios corresponding to minimum $F\#$ for variational solutions and FEM simulations, respectively. The A_f , $F\#$ and RMSWFE corresponds to γ_{FEM}^* values for tunable lens with polygonal and circular pupils at $V_p = -10V$.

Pupil	γ_v^*	γ_{FEM}^*	A_f	$F\#$	RMSWFE [waves]
1	0.51	0.5	0.25	143.96	0.1183
2	0.5	0.49	0.24	146.93	0.1009
3	0.64	0.61	0.24	134.51	0.0505
4	0.57	0.55	0.25	129.43	0.0155
5	0.58	0.55	0.25	129.35	0.0168
6	0.59	0.57	0.26	129.04	0.0137

sirably not to be degraded from the MTF of the fixed lens alone. The resolution of the captured image would be consequentially independent of the object distance.

Figure 3.8b shows the MTF of the fixed lens alone both when the object is at infinity and when it is 368mm away. The MTF has dropped significantly for the closer object because of the larger defocus term Z_2^0 in the wavefront error. Combining the fixed lens with the circularly-shaped tunable lens preserves the MTF performance from significant degradation over a range of object distances after refocusing, as shown in Figs. 3.8c to 3.8e. The tunable lens keeps the MTF nearly the same at different object positions. However, a closer look at the combined MTF shows that the performance is diffraction limited up to the field point (0, 0.6839mm) that corresponds to a $\pm 10^\circ$ FOV. Beyond that angle, the MTF drops due to the tunable lens' off-axis aberrations. For a larger FOV, a simultaneous redesign of the tunable and fixed lens would be helpful to compensate for the dominant aberration.

Pupil masking, as a design degree of freedom, can affect lens figure of merits such as: RMSWFE, dioptric lens power $1/f$, pupil area, resolution and contrast.

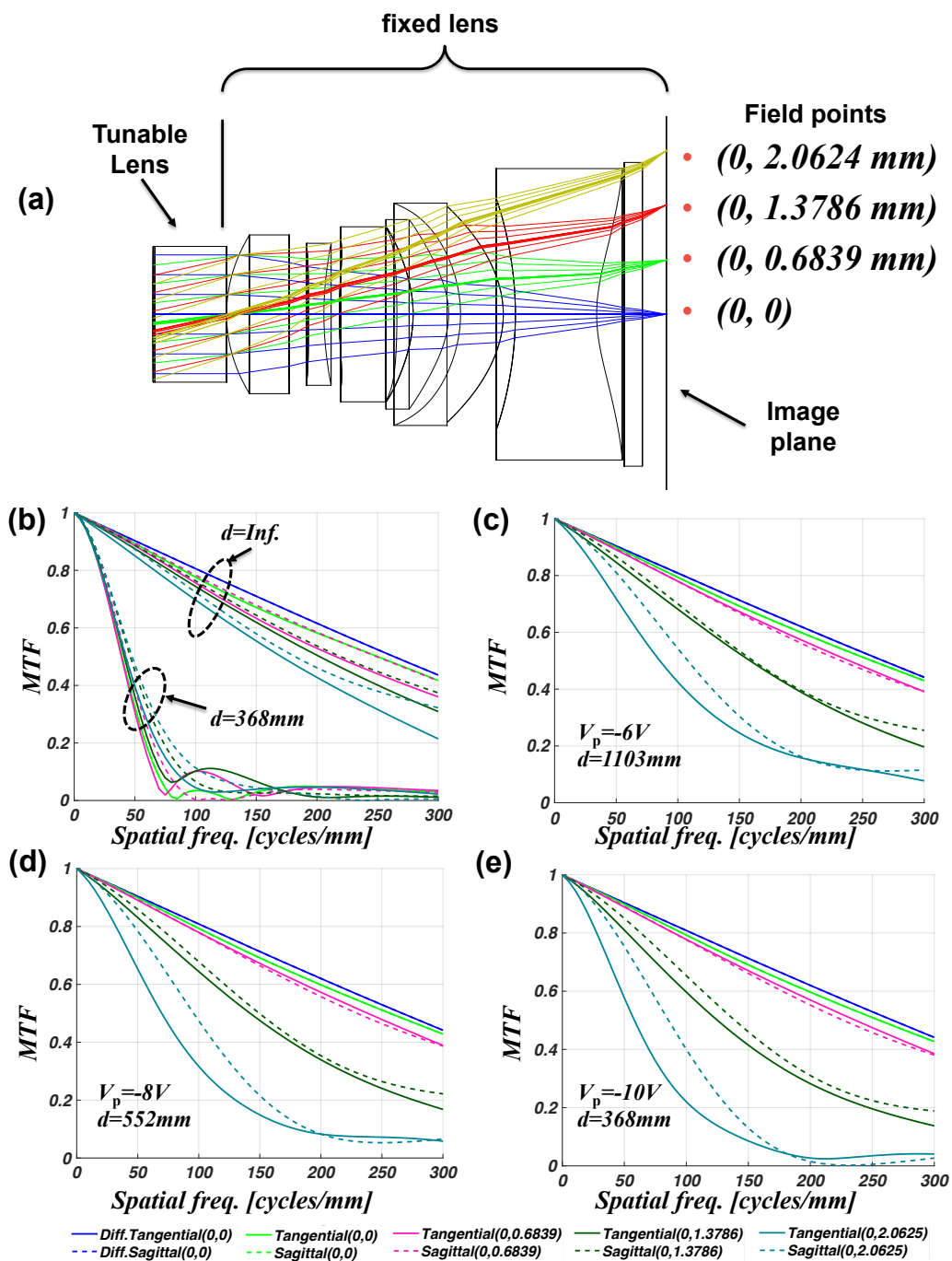


Figure 3.8: (a) Arrangement of the tunable lens with a fixed lens in Zemax for optical simulations. Sagittal and (tangential) MTF for (b) the fixed lens alone without movement when the object is located at infinity and 368mm at different field points on the image plane (coordinates are given in mm in legends). MTF for the tunable lens with circular pupil and the fixed lens when the object is located away (c) 1103mm, (d) 552mm and (e) 368mm.

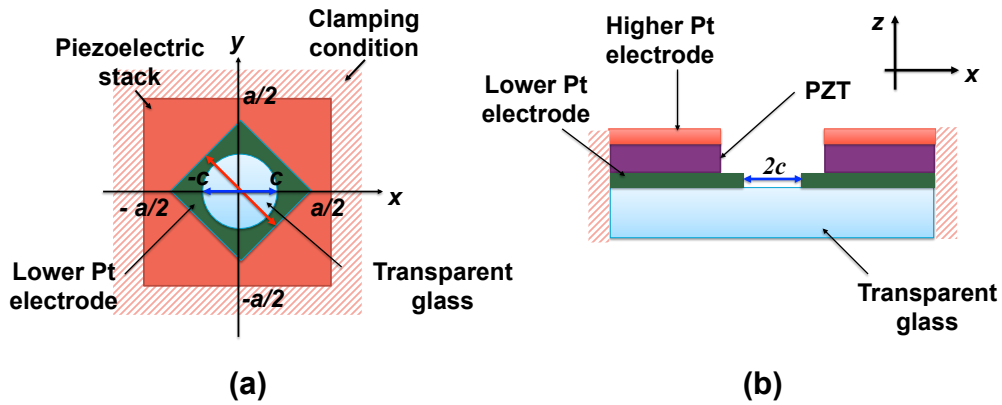


Figure 3.9: (a) Planar view of pupil-masked case 2. (b) Cross-sectional view showing the 45° -rotated square actuator with its circular lower Pt electrode etched to form a circular pupil. The red arrow indicates the reference dimension L_r for each pupil. The blue arrow indicates the diameter $2c$ for the circular pupil opening in the lower Pt electrode.

This can be done during device fabrication by having the PZT stack's lower Pt electrode as a circular opening instead of having the same polygonal shape as the rest of the PZT actuator layers such as in cases 1-6. Figure 3.9 shows a pupil-masked case 2 as an example. Light only passes through the transparent circular opening in the lower Pt electrode layer. The pupil-masked case 2 is now geometrically parameterized by two parameters: γ for the piezoelectric actuator and γ_{op} for the circular opening in the lower Pt electrode. γ_{op} in this pupil-masked case 2 follows the circular pupil definition, which equals $2c/a$ (refer to Fig. 3.9).

For optical simulations, we conduct a parametric sweep on γ_{op} for each γ value. The γ_{op} values are kept below $L_p/(a \tan(\pi/p))$, which corresponds to the polygon's inscribed circle. As a result of this parametric sweep, we get the scattering plots for RMSWFE and $1/f$ in Figs. 3.10a and 3.10b.

We have picked case 6 as a reference since it achieves the minimum $F\#$, as previously discussed. We compare pupil-masked cases 2 versus case 6 with the same pupil opening diameter in Figs. 3.10a and 3.10b. It is evident that pupil-

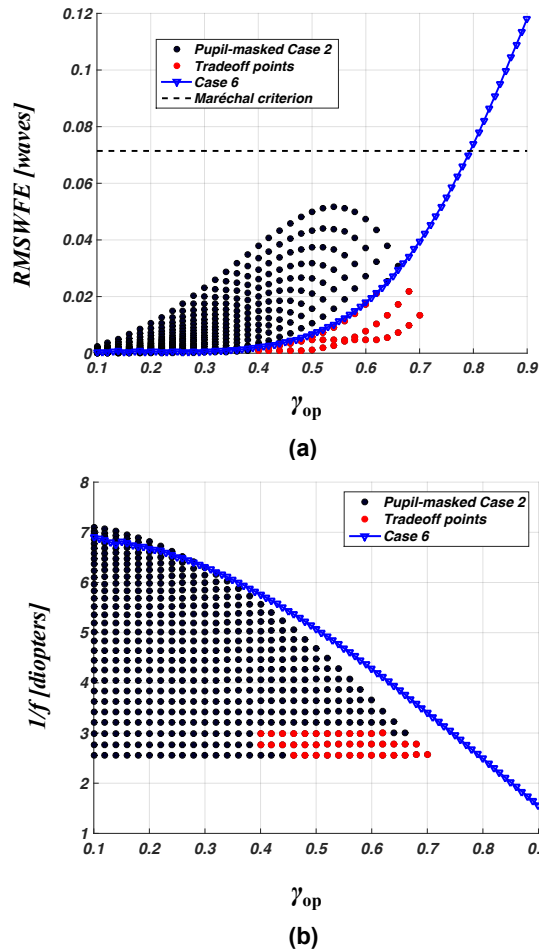


Figure 3.10: Scattering plots of (a) RMSWFE and (b) lens dioptric power $1/f$ with varying the ratios γ_{op} and γ , all with $V_p = -10V$ and $\lambda = 550nm$.

masked case 2, compared to case 6, provides a tradeoff between dioptric power and RMSWFE, specifically for large apertures marked as red dots. They offer lower RMSWFE but less dioptric power for large apertures when compared to case 6. An example on tradeoff points is case 2 with $\gamma = \gamma_{op} = 0.7$ that achieves $f = 389mm$ and RMSWFE of 0.0133 waves. A comparable case 6 with $\gamma = 0.7$ has the same pupil diameter, achieves $f = 293mm$ and RMSWFE= 0.0395 waves, which is 1 diopter better $1/f$ but 3.4 times worse RMSWFE.

4 Trial functions for reduced-order modeling of piezoelectrically actuated MEMS tuneable lenses

This chapter is motivated by the need to further lower the number of Degrees-of-Freedom (DOFs) of the linear model presented the previous chapter. It is named here as model 0 and has been using an ansatz that is solely formed from the weighted Gegenbauer polynomials. Section 4.1 emphasizes on the need for a reduced-order model and discusses how the approach of using a piece-wise ansätze with subfunctions is expected to improve the linear model's speed of convergence to a solution with low DOFs. Section 4.2 presents the new normalized coordinates and how the lens' planar area is partitioned in a way suits applying the new analytical models that are to be presented in section 4.3. Then, section 4.4 displays the linear system of equations for the two new models except that the mathematical derivation has been left out for the reader to check in [51]. Afterwards, section 4.5 compares between three variational models in terms of displacement, optical parameters and more importantly the model order. Finally, this chapter closes with section 4.6 in which an emphasis on that the subfunctions in the pupil area of the new models can still be mapped to Zernike polynomials;

which opens a research possibility to have a reduced-order dynamic model, as will be discussed in Ch. 6.

4.1 The need for reduced-order models

For system-level designers to have computationally efficient models, it is necessary to develop reduced-order models that can be implemented by *e.g.* using MATLAB or a circuit simulator yet faithfully representing the device physics.

Low order models can in principle be obtained by analytical or semi-analytical (series expansion) solutions. In the previous chapter, the diaphragm deflection has been represented by an expansion in a weighted Gegenbauer basis [49]. In this case, each basis function is extended continuously over the entire diaphragm and 120 DOFs were necessary to reach a satisfactory representation of the lens optical performance. Although this is a major improvement in computational effort compared to FEM, it is still quite a large number of DOFs for lumped-model system simulations and too large to be tractable by purely analytical means.

One weakness in the previous formulation is that the basis functions did not account for the discontinuity of the layered structure at the lens opening. There are good reasons to expect that an improvement in convergence could be achieved by taking this discontinuity into account. An approach to significantly improve model accuracy for the piezoelectrically actuated lens is using basis functions that account for the discontinuity in the layered structure at the lens opening. This approach uses the exact solution of the biharmonic equation in the circular regions and fulfills the boundary conditions at the diaphragm edges.

We have chosen analytical ansätze that have Gegenbauer-polynomial-based subfunctions with rectangular symmetry satisfying the plate's boundary condi-

tions and yet can be expanded on the form of Fourier trigonometric series along the circular discontinuity to be matched term-by-term with the exact solutions of the plate's differential equation. For our lens application, the approach succeeds in reducing the model down to 10 DOFs as opposed to 120 for the same accuracy in the previous approach.

4.2 Normalized coordinates

Figure 4.1 shows planar views of the lens marked with definitions used by different models. Models 0 and 1 break the lens domain Ω into two subdomains Ω_1 and Ω_2 while model 2 breaks it into 3 subdomains Ω_I , Ω_{II} and Ω_{III} (we have assigned new labels for subdomains in model 2 to simplify the mathematical representation of variables later on). The lens diaphragm extends over a square with cartesian coordinates $x, y \in [-a/2, a/2]$ and it is convenient to introduce normalized coordinates $X = 2x/a$ and $Y = 2y/a$. Thus, the locus of the lens pupil boundary (Γ_{Ω_1} in Fig. 4.1a or Γ_{Ω_I} in Fig. 4.1b) and the fictitious boundary $\Gamma_{\Omega_{II}}$ in these normalized cartesian coordinates are given by $\sqrt{X^2 + Y^2} = \gamma_1$ and $\sqrt{X^2 + Y^2} = \gamma_2$ where γ_1 and γ_2 respectively are the ratio of the lens pupil and the fictitious circle diameters to the diaphragm side length a .

The lens' circular and annular subdomains Ω_1 , Ω_I and Ω_{II} can be further normalized to a radial coordinate, as shown in Fig. 4.2. For these subdomains, we use the normalized radial coordinate $r = \sqrt{X^2 + Y^2}/\gamma_0$ with $\gamma_0 = \gamma_1$ for models 0 and 1 and to $\gamma_0 = \gamma_2$ for model 2. As shown in Fig. 4.2, the lens pupil boundary for the different models is either of the circles $r = 1$ or $r = \alpha$ where $\alpha = \gamma_1/\gamma_2$.

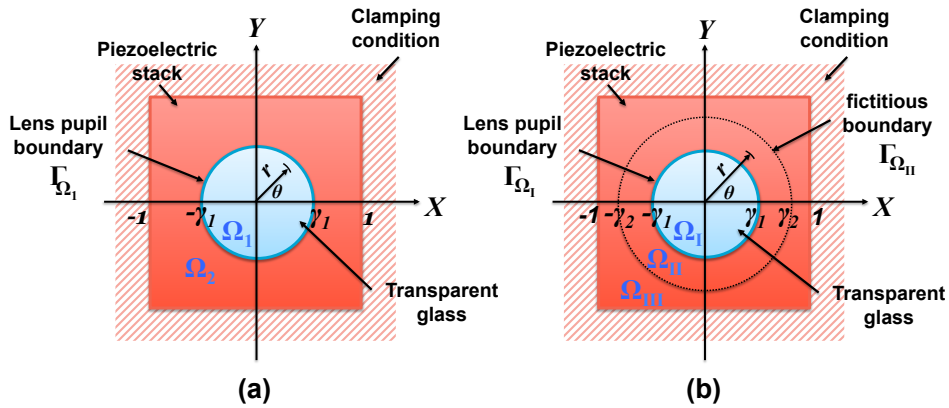


Figure 4.1: Planar views of the piezoelectrically actuated MEMS tunable lens showing decomposing its structure into subdomains. (a) Model 1 break the lens into two subdomains: Ω_1 and Ω_2 . (b) Model 2 breaks it into three subdomains: Ω_I , Ω_{II} and Ω_{III} . Subdomains Ω_{II} and Ω_{III} are separated by a fictitious circular boundary $\Gamma_{\Omega_{II}}$.

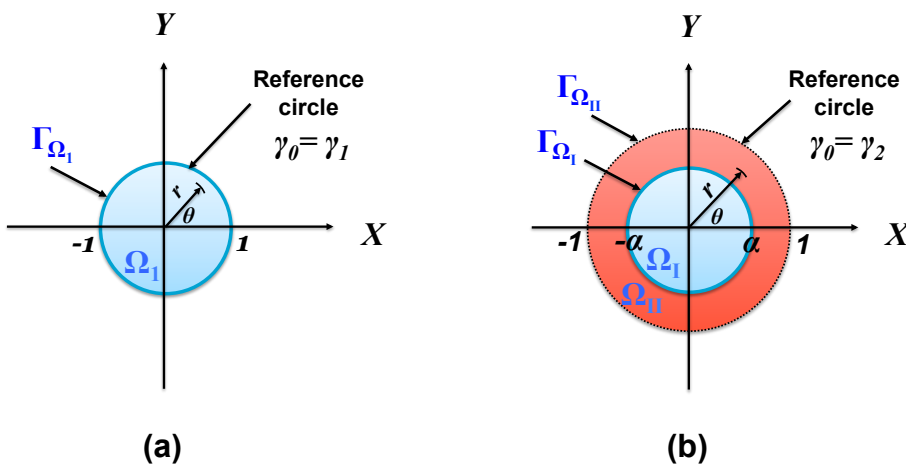


Figure 4.2: Planar views showing the normalized radial coordinates in the circular and annular subdomains for (a) models 0 and 1, and (b) model 2.

4.3 New ansätze for model order reduction

4.3.1 Model 1

Model-1 deals with the lens as a two subdomain problem similar to model 0, but it uses a piecewise expansion of two different basis functions for the displacement approximation in the pupil and actuator regions. Its displacement ansatz in the lens subdomains is

$$\Omega_1: w_0^{(1)} = A_0^I + B_0^I r^2 + \sum_{n=2,4,6,\dots}^{N_F} (A_n^I r^n + B_n^I r^{n+2}) \cos(n\theta), \quad (4.1)$$

$$\Omega_2: w_0^{(2)} = \sum_{k=1}^{N_G} C_k \Phi_k(X, Y), \quad (4.2)$$

where $w_0^{(1)}$ is the subfunction of the displacement ansatz in the subdomain Ω_1 . The ansatz part $w_0^{(1)}$ is equivalent to having a circular FEM element with interpolation functions formed as a product of two polynomials: one is an even polynomial in r for the radial direction and the other a cosine function for the circumferential direction [29]. For the subdomain Ω_2 , the subfunction $w_0^{(2)}$ is the same Gegenbauer basis used in model 0 to enforce the clamped boundary conditions.

4.3.2 Model 2

Model 2 deals with the lens as a three subdomain problem (refer to Fig. 4.1b). To further improve the model accuracy over model 1 at low DOFs, this model enlarges the membrane area over which the homogeneous solution of the plate equation is used beyond the pupil area. Therefore, it adds a fictitious boundary $\Gamma_{\Omega_{II}}$ that amounts to having a new annular subdomain Ω_{III} . Its displacement ansatz in the lens subdomains becomes

$$\begin{aligned} \Omega_I: \quad w_0^{(I)} = & A_0^I + B_0^I r^2 \\ & + \sum_{n=2,4,6,\dots}^{N_F} (A_n^I r^n + B_n^I r^{n+2}) \cos(n\theta), \end{aligned} \quad (4.3)$$

$$\begin{aligned} \Omega_{II}: \quad w_0^{(II)} = & A_0^{II} + B_0^{II} r^2 + C_0^{II} \ln(r) + D_0^{II} r^2 \ln(r) \\ & + \sum_{n=2,4,6,\dots}^{N_F} (A_n^{II} r^n + B_n^{II} r^{n+2} \\ & + C_n^{II} r^{-n} + D_n^{II} r^{-n+2}) \cos(n\theta), \end{aligned} \quad (4.4)$$

$$\Omega_{III}: \quad w_0^{(III)} = \sum_{k=1}^{N_G} C_k \Phi_k(X, Y), \quad (4.5)$$

where $w_0^{(II)}$ is the subfunction of the displacement ansatz over the new annular subdomain Ω_{II} . Its coefficients are A_i^{II} , B_i^{II} , C_i^{II} and D_i^{II} where $i = 0, 2, \dots, N_F$. $w_0^{(II)}$ uses even terms of the full homogeneous solution to the plate equation including logarithmic and negative-power terms, because the subdomain Ω_{II} does not enclose the origin. To maximize the membrane area over which $w_0^{(II)}$ is used, we have chosen the fictitious circle's ratio $\gamma_2 = 1$ in the model-2's computation. This choice means that the homogeneous solution is used over the area of the inscribed circle of the square diaphragm. The subfunction $w_0^{(II)}$ is equivalent to

having an annular FEM element similar to [29]. The subfunction $w_0^{(I)}$ is used for the pupil subdomain as in model 1 while $w_0^{(III)}$ is used over the subdomain Ω_{III} to enforce the clamped conditions, as discussed earlier.

4.4 Variational formulation

We use the linear variation formulation developed in chapter 2. By substituting with the new ansätze, the linear system of equations becomes, for each model,

$$\text{Model 1: } \left(\mathbf{T}_I^T \mathbf{H}^{\Omega_I} \mathbf{T}_I + \mathbf{R}_{k_1 k_2}^{\Omega_2} \right) \mathbf{C} = \mathbf{F}_{k_2} \quad (4.6)$$

$$\text{Model 2: } \left(\mathbf{T}_I^T \mathbf{H}^{\Omega_I} \mathbf{T}_I + \mathbf{T}_{II}^T \mathbf{H}^{\Omega_{II}} \mathbf{T}_{II} + \mathbf{R}_{k_1 k_2}^{\Omega_{III}} \right) \mathbf{C} = \mathbf{T}_{II}^T \mathbf{F}_{II} + \mathbf{F}_{k_2}. \quad (4.7)$$

For the mathematical construction of the matrices in Eqs. (4.6) and (4.7), the reader may refer to Ref. [51].

4.5 Comparison between variational models

In this section, we compare the three variational models taking FEM simulations as a reference. In addition, we have carried out a convergence analysis of these models over the displacement and the optical parameters ($F\#$ and RMSWFE).

4.5.1 Variational solutions versus FEM simulations

Figure 4.3 shows displacement profiles from variational solutions for the three models, and FEM simulations for various pupil opening ratios. Models 0 and 1 show similar behavior when pupil opening ratios are small and the Gegenbauer basis is used for most of the membrane area in model 1. Thus, for these ratios, the contribution of the Gegenbauer-basis terms to the electrical enthalpy of model 1 dominates other contributions and the curves resemble those of model 0 which uses this basis only. This is evident for displacement profiles with $\gamma_1 < 0.6$, as shown in Fig. 4.3. The larger the value of γ_1 is, the more dissimilar are the displacement curves of the two models and the better is the agreement between model 1 and FEM.

Model 2 with $N = 3$ has the worst displacement approximation of all models for most pupil openings, but this improves with increasing N value. Model 2 with $N = 7$ provides better displacement approximations than the other models for all pupil openings of interest. In Fig. 4.3, this becomes particularly clear for the displacement curves of model 2 with $\gamma_1 \leq 0.3$ when compared to models 0 and 1.

To compare the variational solution for w_{NG} of the different models to the FEM result w_{FEM} , we monitor the l_2 relative error norm named here as ζ_w . ζ_w curves for different models and various γ_1 values are shown in Fig. 4.4. It is evident that model 0 shows decreasing, in most cases, nonmonotonic trends for increasing N . However, model 1 shows smoothly decreasing trends and even reaches the highest accuracy at certain N values for γ_1 ratios ≥ 0.4 .

Model 2's approximations appear to be worse with lower order N , but they improve with increasing N . After $N = 7$, the error flattens for all pupil opening

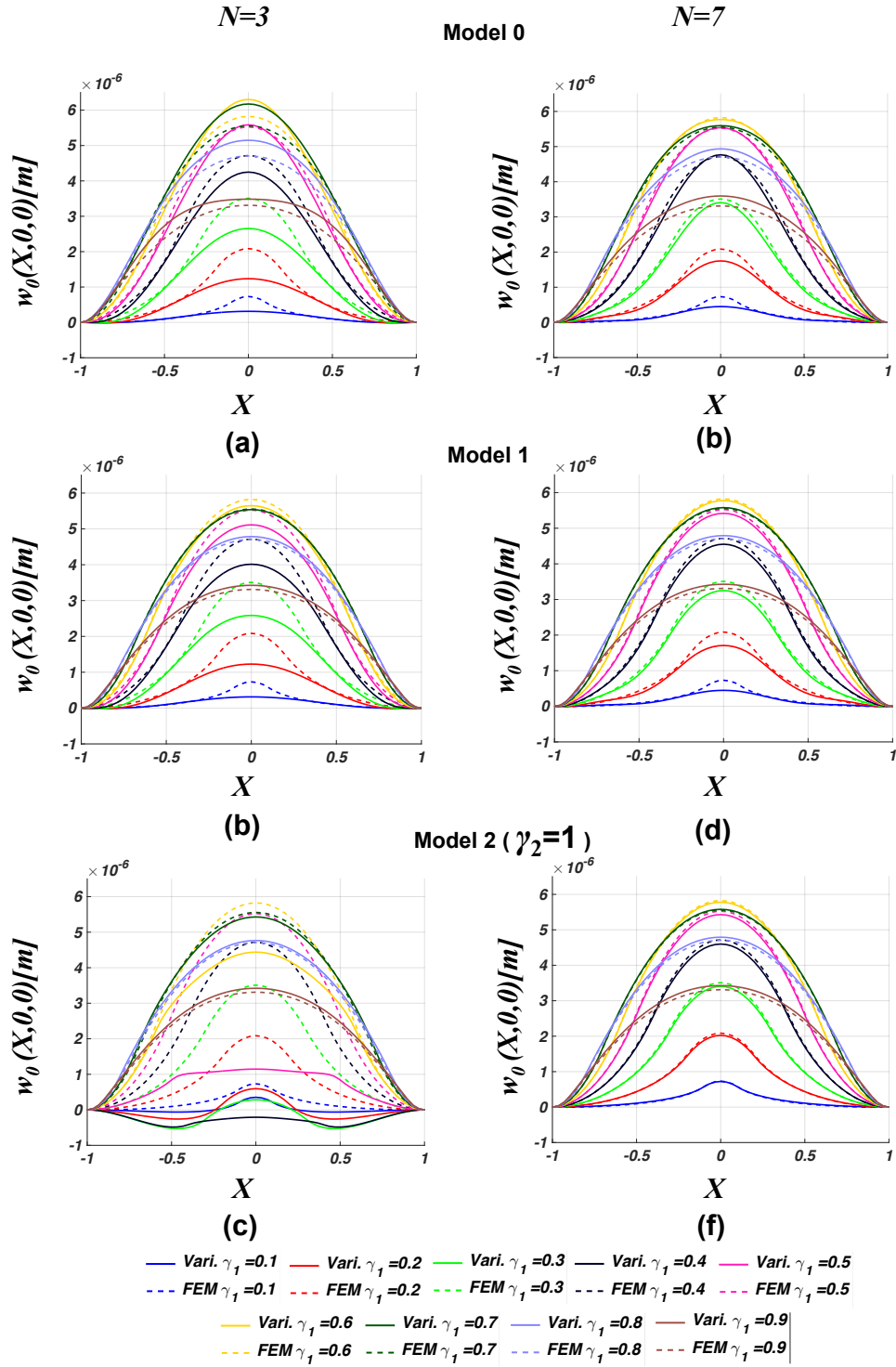


Figure 4.3: Displacement profiles in xz -plane from FEM and different models at $N = 3$ and $N = 7$ for different values of ratio γ_1 with piezoelectric material at $V_p = -10V$.

ratios of interest and model 2 reaches the highest accuracy. Thus, model 2 can outperform the other models with only 10 DOFs.

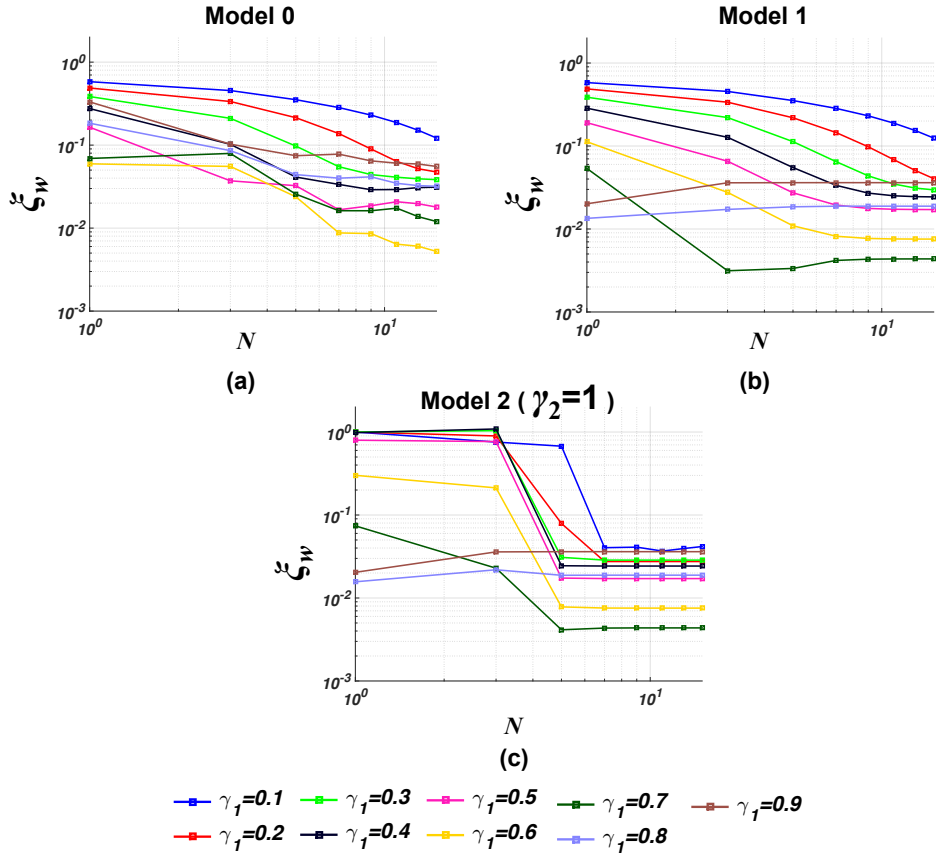


Figure 4.4: l_2 relative error norm for the displacement versus number of polynomials N for different models.

4.5.2 Optical Simulations

Figure 4.5 shows the optical parameters from different models with various N compared to those from FEM simulations. Model 0's approximations show oscillatory behavior for the optical parameters with increasing N similar to the ζ_w curves. Model 1's approximations approach the optical parameters from FEM in

a more uniform way. For $\gamma_1 \leq 0.3$, approximations from models 0 and 1 become similar for the same reason mentioned earlier for their displacements.

For model 2 with $N = 1$, ζ_w is greater than 0.8 for most γ_1 values of interest. Thus, we have omitted optical parameters at that particular value of N . The optical parameters from Model 2 rapidly approach those of FEM and increasing the value of N above 7 does not add any further improvements.

To assess the ability of the variational models in approximating the optical parameters over various pupil openings, we monitor the l_2 relative error norms of $1/F\#$ and RMSWFE expressed as

$$\zeta_{1/F\#} = \left[\frac{\sum_{\gamma_1} (1/F\#_{FEM} - 1/F\#_{Model})^2}{\sum_{\gamma_1} (1/F\#_{FEM})^2} \right]^{1/2}, \quad (4.8)$$

$$\zeta_{RMSWFE} = \left[\frac{\sum_{\gamma_1} (RMSWFE_{FEM} - RMSWFE_{Model})^2}{\sum_{\gamma_1} (RMSWFE_{FEM})^2} \right]^{1/2}. \quad (4.9)$$

The sums in the above equations are over a set of lenses with γ_1 values ranging from 0.1 to 0.9 in steps of 0.02. In this aspect, the parameters $\zeta_{1/F\#}$ and ζ_{RMSWFE} will indicate the effectiveness of each variational model to approximate the lens' optical performance over a wide range of pupil openings. Figure 4.6 shows these norms versus N for the three models. Model 0 and 1 show similar behaviors for $1/F\#$ curves, but model 1 shows an improved performance for RMSWFE curves. Model-1's ζ_{RMSWFE} curve is lower than the one for model 0 by nearly 50% at all N values. Model 2 starts on the wrong foot, but it becomes more accurate as N is increased. When N reaches 7, it becomes the most accurate among the other models. For $N \geq 7$, model 2 achieves accuracies of 5.1% and 2.1% respectively for RMSWFE and $1/F\#$.

For a certain polynomial order, the three models have the same N_G DOFs but their accuracy varies depending on the type of basis functions. Model 2 has reduced these DOFs to only 10 as it uses the homogeneous solution of the plate

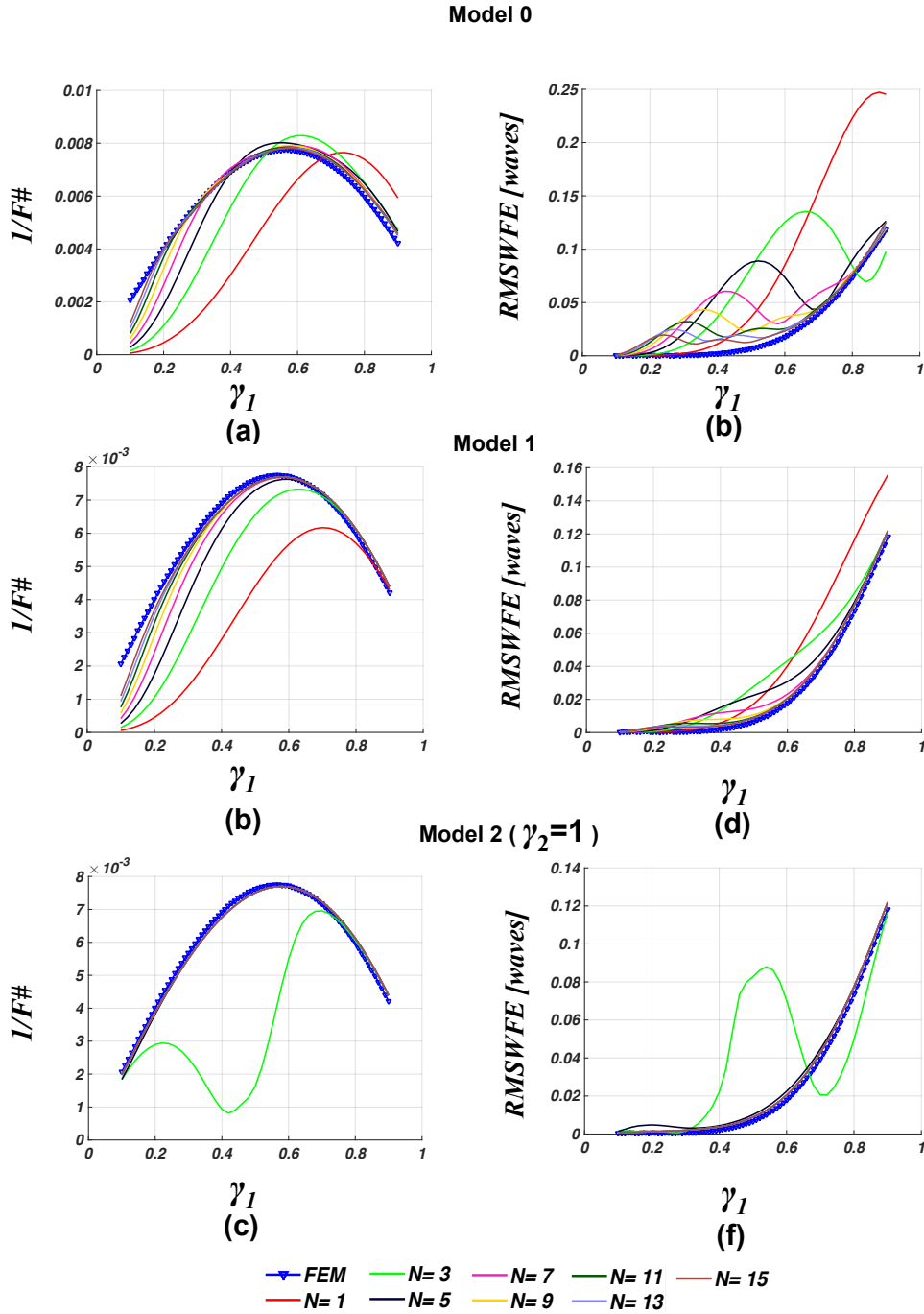


Figure 4.5: Reciprocal $F\#$ and RMSWFE versus the ratio γ_1 , all with $V_p = -10V$ and $\lambda = 550nm$ for the three models.

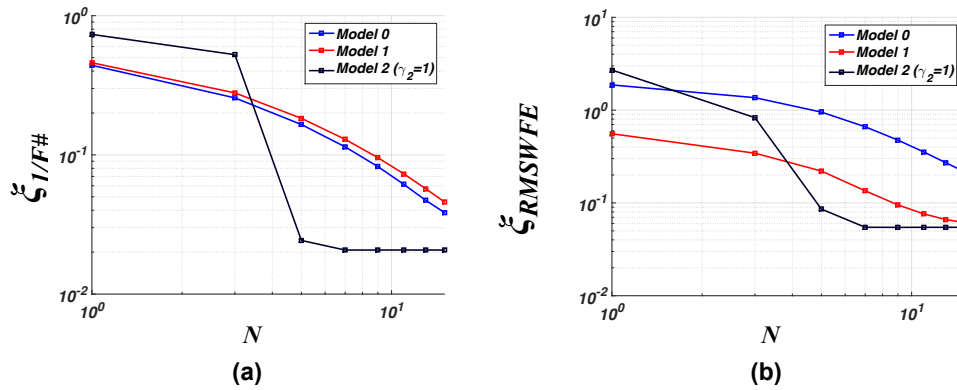


Figure 4.6: l_2 relative error norm of (a) reciprocal $F\#$ and (b) RMSWFE versus order N for three models.

differential equation over most of the membrane area. With the same DOFs, model 0 predicts RMSWFE and $1/F\#$ with the respective accuracies of 11.4% and 66.2%, as shown in Fig. 4.6. It has needed as much as 120 DOFs to bring the accuracies down to those of model 2 in order to provide an acceptable representation of the lens' optical performance [49].

4.6 New ansätze relation to Zernike polynomials

Models 1 and 2 use crafted problem-specific trial functions to yield accurate solution starting with a low-order ansatz. Models 1 and 2 are also powerful tools for optical wavefront representations because they can analytically yield the Zernike coefficients to represent the lens surface. Since the displacement ansatz inside the pupil region has the form of Fourier cosine series, it can be easily mapped to Zernike polynomials $Z_{n'}^{m'}$ [45]. The squared value of Zernike coefficients is calcu-

lated through projection from

Model 1:

$$a_{n'm'}^2 = \int_0^1 \int_0^{2\pi} w_0^{(1)}(r) Z_{n'}^{m'}(r, \theta) r dr d\theta, \quad (4.10)$$

Model 2:

$$a_{n'm'}^2 = \int_0^1 \int_0^{2\pi} w_0^{(I)}(\alpha r) Z_{n'}^{m'}(r, \theta) r dr d\theta \quad (4.11)$$

where

$$\begin{aligned} Z_{n'}^{m'} &= R_{n'}^{m'}(r) \cos(m'\theta) \\ &= \sum_{k=0}^{\frac{n'-m'}{2}} \eta_{n'm'k} r^{n'-2k} \cos(m'\theta), \end{aligned} \quad (4.12)$$

$$\eta_{n'm'k} = (-1)^k \binom{n'-k}{k} \binom{n'-2k}{\frac{n'-m'}{2}-k} \quad (4.13)$$

and n' and m' are nonnegative even integers due to the lens symmetry. Their respective maximum values are $N_F + 2$ and N_F from the $w_0^{(1)}$ (or $w_0^{(I)}$) expression and according to the definition of Zernike polynomials. In Eq. (4.11), the radial variable is scaled by the factor α since Zernike polynomials are defined on a reference unit circle that is usually taken as the lens pupil.

From Eqs. (4.12) and (4.13), and substituting of $w_0^{(1)}$ into Eqs. (4.10) and (4.11), it equals

$$\begin{aligned} a_{n',m'}^2 &= \zeta_{m'} \pi \sum_{k=0}^{\frac{n'-m'}{2}} \eta_{n'm'k} \left(\frac{A_{m'}^I \tau_{A_{m'}}}{n'-2k+m'+2} \right. \\ &\quad \left. + \frac{B_{m'}^I \tau_{B_{m'}}}{n'-2k+m'+4} \right) \end{aligned} \quad (4.14)$$

where A_i^I and B_i^I are the coefficients of the displacement ansatz' subfunction in

the pupil area. $\zeta_{m'}$ is the Neumann factor that equals 2 if $m' = 0$ and 1 otherwise. Due to scaling of the radial variable, the correction factors τ are defined as

$$\mathbf{Model\ 1:} \quad \tau_{A_0} = \tau_{B_0} = \tau_{A_{m'}} = \tau_{B_{m'}} = 1, \quad (4.15)$$

$$\mathbf{Model\ 2:} \quad \tau_{A_0} = 1, \tau_{B_0} = \alpha^2, \tau_{A_{m'}} = \alpha^{m'},$$

$$\tau_{B_{m'}} = \alpha^{m'+2}. \quad (4.16)$$

In that manner, the reduced models can substitute the FEM mechanical simulations of the lens and directly provide the Zernike coefficients representing the lens sag.

5 Modeling piezoelectrically actuated MEMS tuneable lenses with geometric nonlinearity

In the previous chapters, residual stresses due to fabrication processes, as discussed in Sec. 1.2, have been neglected and also the actuation voltage has been kept low enough to stay within the linear regime. Accordingly, the linear model, under those assumptions, has been accurate to model the lens performance. The following chapter, in section 5.1, presents a variational model for the geometrically nonlinear behavior of the piezoelectrically actuated MEMS tuneable lenses. This model can explain the softening and hardening effects exhibited by the lens during its operation affecting its optical performance. Thus, in the view of von Kármán's plate theory, the presented nonlinear model predicts the lens displacement after solving a cubic nonlinear system of equations and shows good agreement with FEM simulations over various combinations of tensile and compressive residual stresses. Then, section 5.2 presents a quantitative optical performance of the lens showing how the lens focus range is enlarged for a certain combination of layers' residual stresses. Finally, in section 5.3, the model succeeds in fitting experiment when used in a constrained optimization scheme in which the layers'

residual stresses and the effective e_{31} piezoelectric coupling coefficient are the fitting parameters.

A difficulty arises, specifically, from the burden of calculating the variational integrals for higher order stiffnesses of the lens' circular pupil. Those integrals are needed to solve the nonlinear equations of motion. To fix that, we have written the ansatz on the form of a Fourier trigonometric series and by using the orthogonality property of the trigonometric functions, the number of these integrals has been significantly reduced. For the mathematical treatment, the interested reader may consult Ref. [52].

5.1 Variational formulation

Considering von kármán strains, the nonlinear system of equations minimizing the energy can be written in Einestein notation as

$$\begin{aligned} & \left(R_{k_1 k_2} + R_{k_1 k_2}^N \right) C_{k_1} + R_{k_1 k_2 k_3} C_{k_1} C_{k_2} \\ & + R_{k_1 k_2 k_3 k_4} C_{k_1} C_{k_2} C_{k_3} - F_{k_2} = 0, \end{aligned} \quad (5.1)$$

where all the indices k_1, k_2, k_3 and k_4 enumerate from 1 to N_G . The linear stiffness has two terms; the first term $R_{k_1 k_2}$ is the linear stiffness one would have without geometric nonlinearity, while the second one $R_{k_1 k_2}^N$ is the contributing stiffness due to the geometric nonlinearity to the linear stiffness, and strongly depends on the residual stresses and the piezoelectric coupling factor. The terms $R_{k_1 k_2 k_3}$ and $R_{k_1 k_2 k_3 k_4}$ are the quadratic and cubic stiffnesses resulting from contributing the transverse displacement w_0 to the stretching strains. The term F_{k_2} represents the equivalent forces due to piezoelectric coupling and residual stresses. To numer-

ically solve Eq. (5.1), Newton-raphson method with an analytical jacobian has been used [52].

5.1.1 Variational solutions versus FEM

In the analyzed cases, we have assumed bi-axial residual stresses in the xy -plane and zero residual shear stress in each layer such that $T_{xx}^{R,(l)} = T_{yy}^{R,(l)} = T^{R,(l)}$ and $T_{xy}^{R,(l)} = 0$. Under various combinations of tensile and compressive stresses, Fig. 5.1 shows that the variational solutions ($N = 13$) are in a good agreement with FEM simulations.

The horizontal subfigures with similar stress $T^{R,(2)}$ in the PZT layer, show that the amplitudes of counterpart displacements at the same voltage, decrease with increasing the stress in the glass layer $T^{R,(1)}$. This indicates that $T^{R,(1)}$ only affects the stiffness terms $R_{k_1 k_2}^N$ not the force ones F_{k_2} (refer to (Eqs.2.32) and (2.33)). The effect of $T^{R,(1)}$ becomes crystal clear for the curves with $T^{R,(2)} = 0$. No effect of $T^{R,(1)}$ on F_{k_2} integrals occurs as a result of integrating $\Phi_{k_2,XX}$ and $\Phi_{k_2,YY}$ in the expression $M_{xx}^{R,(1)} \Phi_{k_2,XX} + M_{yy}^{R,(1)} \Phi_{k_2,YY}$ (refer to Eq. (2.32)) over the whole glass layer, which leads to zero due to the clamping condition of zero slope. However, this is not the case for the $T^{R,(2)}$ since the PZT layer has a central hole causing the resultant F_{k_2} integrals to be nonzero. By looking at the vertical subfigures with the same $T^{R,(1)}$ value, we can infer that $T^{R,(2)}$ changes both the terms $R_{k_1 k_2}^N$ and F_{k_2} . Hence, the changes in the initial bending profile whether it is upwards with (zero or tensile $T^{R,(2)}$), or downwards with compressive $T^{R,(2)}$. Another evidence is the variance in the displacement-to-voltage sensitivity when comparing groups of two displacement profiles at two alike voltages at different values of $T^{R,(2)}$ (refer to the vertical subfigures in Fig. 5.1).

The value of the stress $T^{R,(2)}$ drastically changes the lens optical performance,

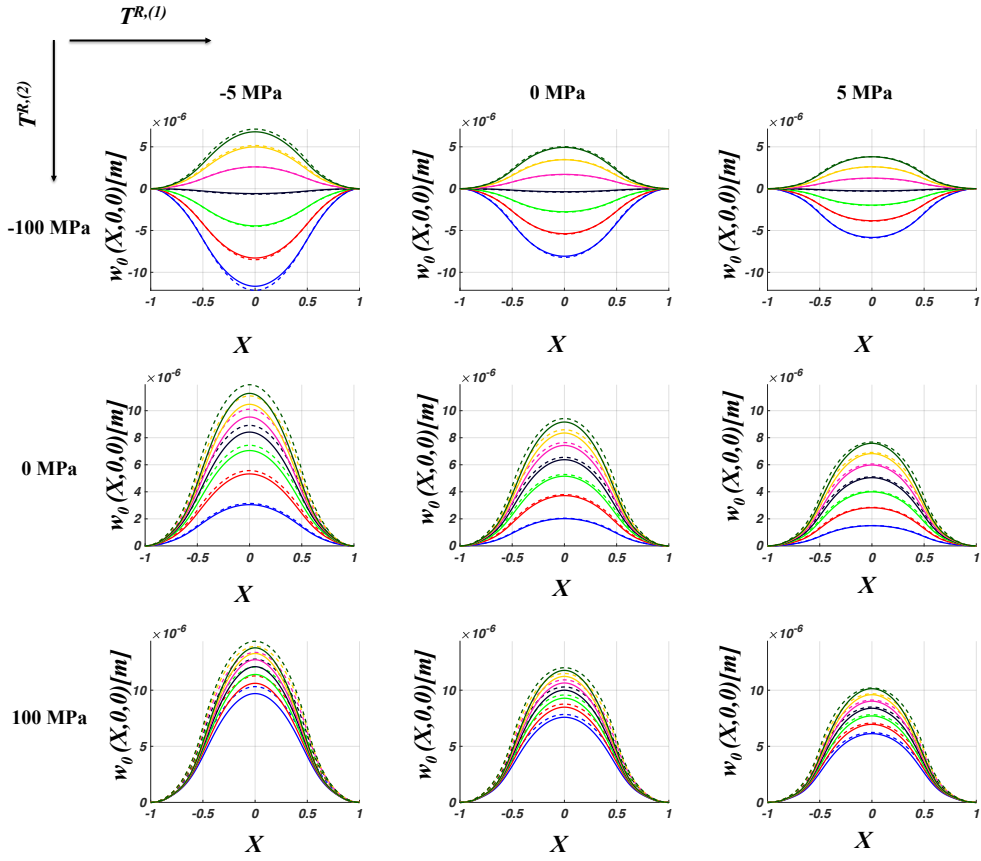


Figure 5.1: Displacement profiles in xz -plane from FEM (dashed) and the variational tool ($N = 13$) for $\gamma_0 = 0.5$ at different layer stresses and voltages. They are at different voltages ranging from -4V (colored blue) to -28V (colored dark green) with a constant step of -4V.

as shown in Fig. 5.1. Its value determines the course of the nonlinear behavior to be either softening, hardening or both; similar to the laminated plate loaded by a pressure in [53]. With a compressive $T^{R,(2)}$, the membrane is initially bent downwards exhibiting a softening effect such that the membrane shows less stiffness, allowing high displacement-to-voltages sensitivity. As the voltage is modified from -4V to -28V with constant steps of -4V, this softening effect swaps to be a hardening effect once the membrane bending profiles change from being downwards to upwards and the displacement-to-voltage sensitivity decreases. In that scheme with compressive $T^{R,(2)}$, the lens possibly would have a wider tunable range of focal lengths due to being operated both as a plano-concave and plano-convex lens, based on the biasing voltage value. Differently, with zero and tensile $T^{R,(2)}$, the membrane exhibits only a hardening effect with varying the biasing voltage values and the initial profiles are bent upwards with slowly increasing amplitudes not matching the increase in voltage values when visually compared to their counterpart curves but with a compressive $T^{R,(2)}$. The more tensile $T^{R,(2)}$ becomes, the stronger the hardening effects and the lower the displacement-to-voltage sensitivity. This can be noticed from the counterpart curves with the same value of $T^{R,(2)}$ in the last two rows in Fig. 5.1. Therefore, larger tensile stresses will limit the lens' tunable range of focal lengths and consequently the optical power swing that could be achieved by the lens.

5.2 Qualitative optical performance

We dedicate this section to qualitatively discuss the lens' optical performance using FEM solutions in terms of RMS-wavefront-error (RMSWFE), and optical power swing (OPS). OPS is defined as the difference between the largest and the lowest

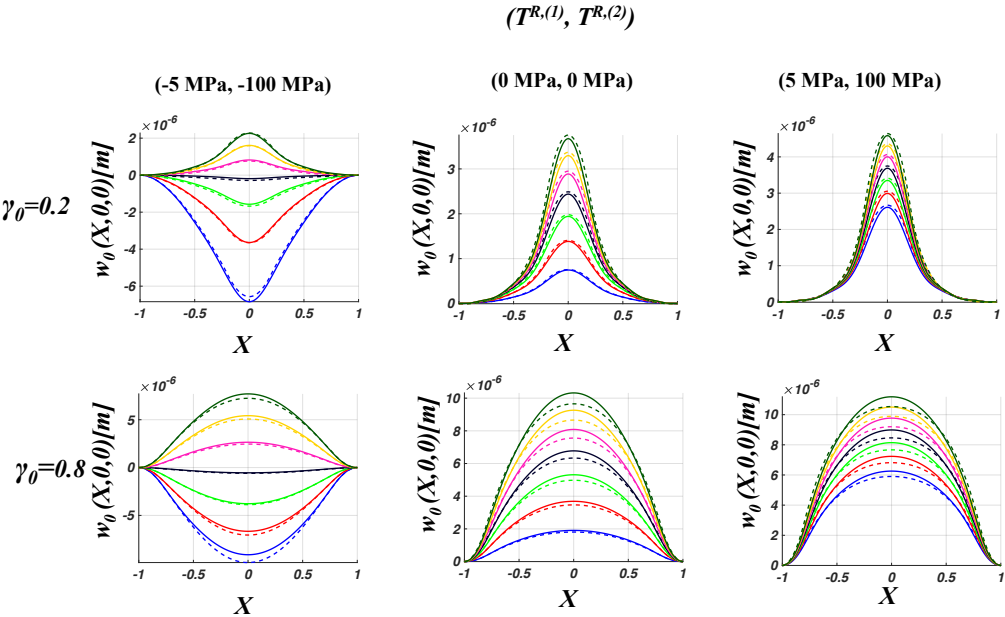


Figure 5.2: Displacement profiles in xz –plane from FEM (dashed) and the variational tool ($N = 13$) for other γ_0 values at different layer stresses and voltages. They are at different voltages ranging from -4V (colored blue) to -28V (colored dark green) with a constant step of -4V.

optical powers obtained by the lens for a certain voltage range; where $(1/f)$ is the optical power and f is the lens' focal length. The mentioned optical parameters are the tunable lens' performance metrics that are to be used for system-level simulations when the lens is to be combined with a fixed-focal-length lens. The higher the optical power swing and the lower the RMSWFE, the better this tunable lens.

Based on the residual stresses values, the bending profile at $V_P = 0$ may be not flat and the tunable lens alone has a non-zero initial optical power. If this lens is directly combined with a fixed-focal-length lens, the on-axis rays from an object at infinity would be focused at a distance either in front or behind the image plane (*i.e* the image sensor). However, this situation can be remedied by modifying the curvature of the first surface of the fixed-focal-length lens and the distance separating it from the tunable lens until the on-axis rays from an object at infinity, are in focus at the center of the image plane. In that manner, the combination of the two lenses has no optical power at 0V.

Figure 5.3 shows optical metrics using the lens sag from FEM simulations for $\gamma_0 = 0.6$. In the view of the displacement profiles from Fig. 5.1 and the optical simulations, if $T^{R,(2)}$ is compressive, the lens can be operated as a plano-convex/plano-concave lens and can possibly achieve the highest optical power swing with the lowest RMSWFE for a certain PZT stack. For $T^{R,(2)} = -100$ MPa, OPS is 11.9 diopters, which is higher when compared to other stress values as shown in Tab. 5.1. However, if the stress $T^{R,(2)}$ becomes tensile, the initial bending profile is upwards and the sensitivity of the displacement-to-voltage becomes less than the situations in which $T^{R,(2)}$ is zero or compressive. In this case, the lens has a large initial optical power that slowly changes with increasing voltage, which results in having smaller optical power swings and higher RMSWFEs. For $T^{R,(2)} = 100$ MPa, OPS is reduced to 5.5 diopters and the optical power is slowly

varied with voltage which matches with slowly varied displacement in Fig. 5.1.

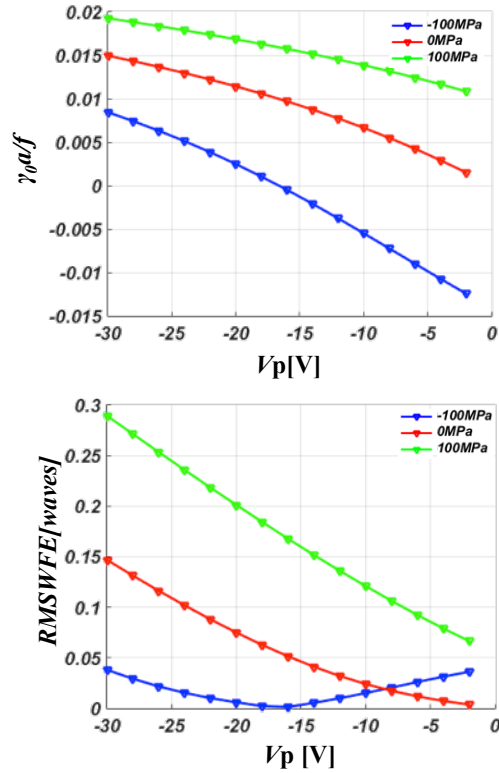


Figure 5.3: $\gamma_0 a/f$ and RMSWFE versus actuation voltage V_p for different $T^{R,(2)}$ values at $T^{R,(1)} = 0$, $\gamma_0 = 0.6$ and $\lambda = 550\text{nm}$.

Table 5.1: Optical power swing for a 30-V source.

$T^{R,(1)}$ [MPa]	-100	0	100
OPS [diopter]	11.9	8.3	5.5

The residual stresses can be controlled through engineering the fabricational process of the PZT stack and the layers on which it is mounted, through optimizing the layers' thicknesses and thermal expansion coefficients. These stresses could be adjusted in a manner that improves the lens' optical performance metrics.

5.3 Model versus Measurements

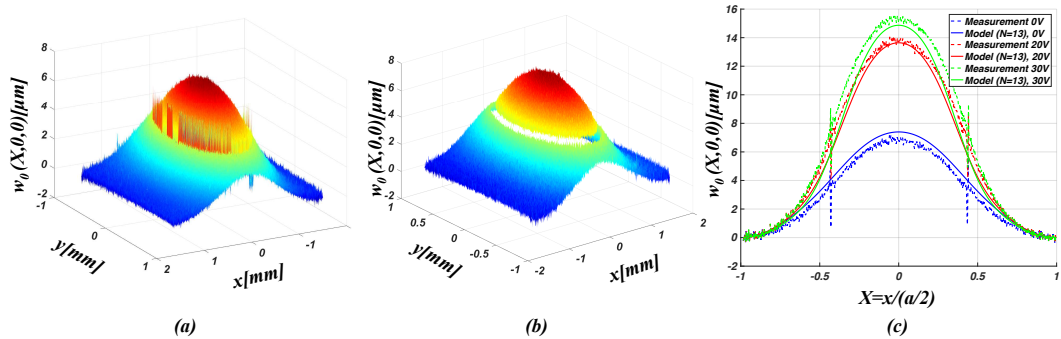


Figure 5.4: (a) Measured displacement profile at 0V. (b) Measured displacement profile at 0 V after numerical treatment to remove tilt, rotational misalignment and distorted data around the electrode's inner edges. (c) Cross-sectional profiles from the measurements and model fittings at three voltages.

To assess the model's effectiveness in modeling the piezoelectric coupling in such lenses, we try to validate the model versus experiment. The measured device is fabricated using Silex-Microsystem's Piezo-MEMS process [24]. The device stack is $\text{Si}/\text{SiO}_2/\text{Ti}/\text{TiO}_2/\text{Pt}/\text{PZT}/\text{Au}$, but the silicon layer is dry etched leaving a layered structure. After etching, a silicon frame is left to mechanically hold the lens and provide clamping conditions at its four edges. When the lens is fabricated, there are uncertainties in determining the exact values of layer stresses ($T^{R,(1)}$, $T^{R,(2)}$) and the effective piezoelectric coupling factor \bar{e}_{31} . Thus, these parameters are the model's fitting parameters whose values are to be optimized until a good agreement is reached between the model and the measurements.

Differently from the simulated devices, the measured device has the structural parameters $a = 3.2\text{mm}$ and $\gamma_0 = 0.41$. The 2-D displacement profiles have been measured using a WYKO white light interferometer NT9100 (Bruker Corp.)

[54] in air and the piezo-stack was biased through two pairs of metal pins touching the device' electric pads that were placed at the clamped silicon frame such that probing would not affect the membrane displacement. To have good resolutions, we have only monitored a rectangular part of the diaphragm area defined by $3.2\text{mm} \times 2\text{mm}$. The measured displacement profiles have asymmetry that can not be captured with the basis functions used in fitting that are forced to have 90° -fold symmetry. Therefore, before fitting, the measured data has been numerically treated to remove tilts, rotational misalignment and the distorted data along the boundary separating the actuator and the pupil, as shown in Figs. 5.4a and 5.4b.

The variational model is used in a constrained optimization scheme such that the fitting parameters are trimmed until a match between the experimental measurement and the model is reached. This matching happens through the following minimization criterion

$$\min_{T^{R,(1)}, T^{R,(2)}, \bar{e}_{31}} \prod_{k=1}^3 \zeta_{w,k}, \quad (5.2)$$

where the index k enumerates from 1 to 3 denoting three voltage measurements of 0, 20 and 30 volts, and $\zeta_{w,k}$ is the l_2 -relative error norm for the k^{th} measurement. However, $\zeta_{w,k}$ here was calculated for the 2-D surface displacement and not just for the cross-sectional profiles as in the simulations part. The objective function is formulated as a product in order not to favor one of the measured profiles based on amplitudes, which happens if the objective function is simply the sum of errors. In that manner, our fitting criterion simultaneously provides good fittings for the three measured voltages.

The process [24] provides a bulk piezoelectric coupling coefficients larger than -15 C/m^2 , which corresponds to \bar{e}_{31} of -21 C/m^2 and has been used as an initial

value of the coefficient \bar{e}_{31} . However, the initial values of the stresses are extracted from measuring test structures on the same wafer as the measured device. These test structures have stacks as Si/SiO₂, Si/SiO₂/Ti/TiO₂/Pt and Si/SiO₂/Ti/TiO₂/Pt/PZT. These stacks have been progressively simulated in COMSOL as a new layer is added and the biaxial stresses in the added layer are finely tuned until a good match is reached between simulations and the measured profiles. However, in our modeling approach, we here have neglected the adhesion and electrode layers. Thus, this leaves us with only two layer stresses $T^{R,(1)}=-11$ MPa and $T^{R,(2)}=26$ MPa.

The variational model has been used in a constrained optimization scheme using the the MATLAB function "*fmincon*". The lower and upper bounds of the fitting parameters are set to freely vary as a percentage of $\pm 50\%$ from their initial values. The initial and fitting values are listed in Table 5.2. The fitting value of \bar{e}_{31} is -20C/m^2 corresponds to a bulk piezoelectric coefficient e_{31} of -14C/m^2 , which is close to the value reported by [24]. Figure 5.4c shows that the fittings from the model ($N = 13$) are in good agreement with the measurements for all the three voltages.

Table 5.2: The fitting parameters.

Parameter	initial value	fitted value
$T^{R,(1)}$	-11 MPa	-15 MPa
$T^{R,(2)}$	26 MPa	29 MPa
\bar{e}_{31}	-21 C/m^2	-20 C/m^2

6 Conclusions and proposal for future research

6.1 Conclusions

Modeling frameworks for the linear and geometrically-nonlinear performance of piezoelectrically actuated MEMS tunable lenses are reported in this thesis. Starting with Hamilton's principle, variational formulations have resulted in obtaining equations of motion, which can be solved in MATLAB in a time less than it takes a FEM program to solve the same problem. The presented models have been verified versus FEM and measurements.

We have constructed a modeling framework that has two major parts. Its first part is to model the static electromechanical performance, while the second part is to investigate quantitatively the tunable lens's optical performance using ray tracing by analyzing its F -number ($F\#$), RMS wavefront error (RMSWFE) and Modulation Transfer Function (MTF). Different symmetric configurations of d_{31} piezoelectric actuators have been investigated. In this way, we have found optimal sets of actuators' geometrical parameters that would give a diffraction-

limited tunable lens.

A key pillar in the success of our modeling framework is the choice of suitable displacement ansätze (the weighted Gegenbauer polynomials in Ch. 3 and the new ansätze in Ch. 4). They satisfy the mechanical boundary conditions, and more importantly the lens displacement within the pupil area can be analytically expressed in terms of Zernike polynomials; which are suitable for the optical representation of the lens' wavefront. In this manner, this has helped in having an error free transformation of the lens sag without the need to export a fine grid-points of the displacement at the pupil area in case of using FEM solutions. Another key pillar is the pre-calculation of the (linear and nonlinear) variational integrals in terms of the actuator's geometrical parameters, which have enabled the modeling framework to be faster compared to FEM especially during an optimization search for an optimum parameter sets.

First, we have investigated linear model for lens with different polygonal pupil shapes. It has been proved to be in agreement with FEM simulation with a relative error norm less than 10%. Among different pupil shapes, the circularly shaped pupil has been proved to achieve a diffraction-limited lens with the widest aperture area with an area factor 0.26 compared to the square diaphragm with nearly 4.5 diopter for a 10-V swing. Second, and through optical simulation, when the tunable lens is combined with fixed lens, the overall MTF has been preserved from degradation over a range of object distance after refocusing. However, a closer look at the combined MTF shows that the performance is diffraction limited up to the field point (0, 0.6839mm) that corresponds to a $\pm 10^\circ$ FOV. Beyond that angle, the MTF drops due to the tunable lens' off-axis aberrations. For a larger FOV, a simultaneous redesign of the tunable and fixed lens would be helpful to compensate for the dominant off-axis aberration.

Third, we have investigated a design idea called pupil masking in which the

lens pupil is kept circular while investigating different polygonal openings in the piezoelectric actuator. As a result, the 45-rotated square opening in the piezoelectric actuator is found to give a trade-off between the focal lens and the RMSWFE allowing having larger apertures. In addition, such design idea allows having lenses with lower RMSWFE at the expense of the dioptric power when compared with the original design of the circular-shaped pupil with the same pupil opening. For example, with $\gamma = \gamma_{op} = 0.7$, the 45-rotated square opening achieves $f = 389\text{mm}$ and RMSWFE of 0.0133 waves, while the circular-shaped pupil with the same ratio $\gamma = 0.7$ achieves $f = 293\text{mm}$ and RMSWFE = 0.0395 waves, which is 1 diopter better $1/f$ but 3.4 times worse RMSWFE.

Fourth, a weakness in the previous ansatz has been identified and there is a room for further improvement of the model. This weakness has been the inability of the weighted Gegenbauer polynomials alone to account for the discontinuity of the lens' layered structure at the pupil opening, as well as the high order (*i.e.* 120 DOFs) needed to have higher accuracies. Hence, we have been motivated to investigate new analytical ansätze that are piecewise subfunctions; one is the weighted Gegenbauer polynomials to enforce the lens boundary conditions, and the others are the exact solutions of the circular plate's differential equations. To be redundant, the new models' subfunction within the pupil can still be mapped to Zernike polynomials. Consequently, we have investigated two other models and fully deduced their variational formulation. The new two models have been proven to achieve less order and higher accuracies than those achieved by using solely the weighted Gegenbauer polynomials. For example, model 2 with 10 DOFs achieves accuracies of 5.1% and 2.1% for RMSWFE and $1/F\#$ while model 0, with the same number of DOFs, can only achieve respective accuracies of 66.2% and 11.4%. Model 2 has been a success because the larger this area over which the exact solution for the elastic plate differential equation is used,

the lower is the number of DOFs needed to reach high accuracy in terms of mechanical and optical parameters.

Finally, we have been motivated to extend the variational model to include geometric-nonlinearity, since in reality there is impossibility to have such lens structure with zero residual stresses and to limit actuation voltage values to the linear regime. Therefore, we have considered von Kármán's strains and developed the cubic equations of motion to solve for the displacement. Because of the discontinuity at the lens pupil, the quadratic stiffness terms in the cubic equation of motion are nonzero. This consequently affects the lens during operation and causes hardening and softening effects that can be utilized in increasing the lens tunable range of focal length. For a certain combination of layer stresses during fabrication, the lens can be operated simultaneously as a plano-convex and a plano-concave lens, which has extend the optical power lens from 8.3 diopters (no stresses) to 11.9 diopters for a 30-V voltage source. To verify the nonlinear model versus measurements, it has been used in a constrained optimization scheme with fitting parameters (layer stresses and piezoelectirc coupling coefficient \bar{e}_{31}), which has resulted in showing good agreement of the model with the measurement.

In practice, the developed models can be utilized for optimization of different material choices and layers thicknesses to find the optimum geometrical parameter of the piezoelectric actuator. In addition, these developed models can be used by system-level lens designers. Accordingly, they can avoid the burden of simulating different actuators of the lens firstly using FEM, then export the lens displacement profiles to optical program to calculate the optical performance. Nevertheless, the presented models can be generally used for any similar structures after reformulating the variational formulation to include the actuating forces due to *e.g.* pressure or thermoelasticity.

6.2 Proposals for future research

The next logical step is to extend the variational model to be a dynamic model in which the displacement ansatz can be written on the form

$$w_0 \approx w_{N_G} = \sum_{k_1=0}^{N_G} C_{k_1}(t) \Phi_{k_1}(X, Y), \quad (6.1)$$

which leads to having the following equation of motion, after adding damping terms, in Einstein notation to be written as

$$R_{k_1 k_2} C_{k_2} + \zeta_{k_1 k_2} \dot{C}_{k_2} + M_{k_1 k_2} \ddot{C}_{k_2} = F_{k_2}, \quad (6.2)$$

where

$$\zeta_{k_1 k_2} = \alpha_R R_{k_1 k_2} + \alpha_M M_{k_1 k_2}, \quad (6.3)$$

such that α_R and α_M are Rayleigh damping coefficients.

A dynamic model allows building an equivalent circuit as shown in Fig. 6.1, which its parameters can be fetched from Eq. (6.2). This enables system-level simulations of the lens dynamics that are of importance when it comes to focal length adjustment during focusing at different objects inside an image frame.

Figure 6.2 shows step response resulting from dynamic simulations using the models from Ch. 4 and with a comparison with FEM solutions. To emphasize on the usefulness of our model, our dynamic model has taken 3 minutes while FEM has taken 1.5 hour for the same transient simulations.

Up to this point, the polymer has been assumed to be weightless and to have low Young modulus such that it does not affect the membrane bending. However, this in reality would depend on its thickness. Accordingly, Eq. (6.2) paves the way

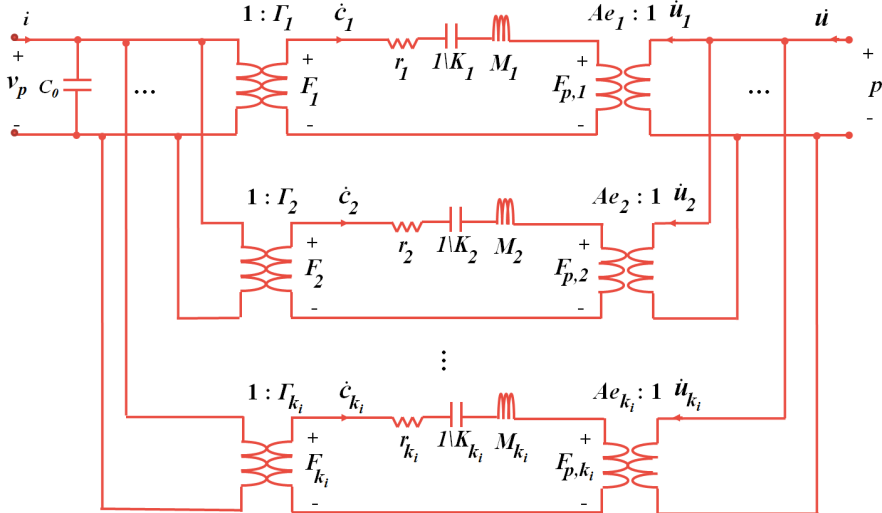


Figure 6.1: Equivalent circuit of the tunable lens.

to include a model for the polymer and allow system-level simulations such as sweeping focus range in the process for the camera to focus on different objects to be captured in images. This will allow monitoring the change of RMSWFE versus time until the lens movement reaches steady state.

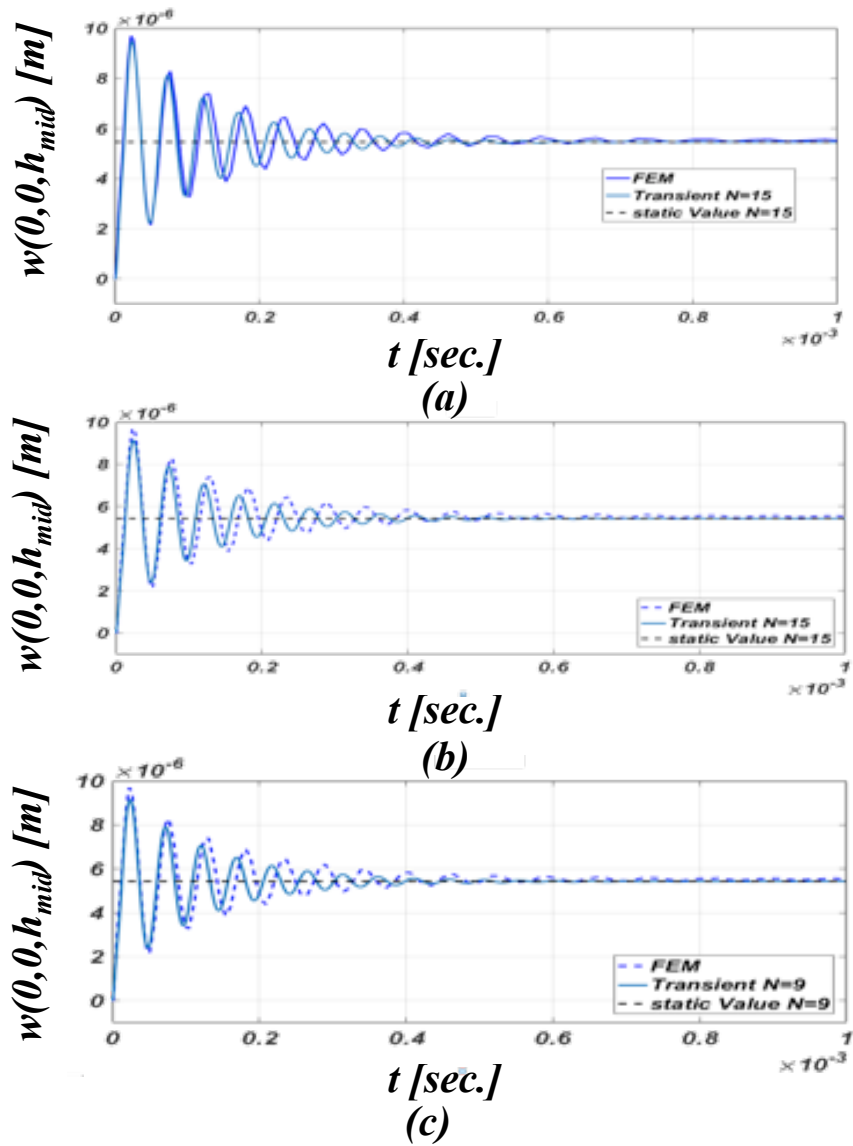


Figure 6.2: Step response of the lens using the ansatz of (a) model 0 (b) model 1, and (c) model 2 with Rayleigh parameters $\alpha_R = 10^{-6} s$ and $\alpha_M = 10^{-4} s^{-1}$.

6 Bibliography

- [1] J. F. Nye, *Physical properties of crystals: Their representation by tensors and matrices*. Oxford university press, 1985.
- [2] J. W. Goodman, *Introduction to Fourier optics*. McGraw-Hill, 1996.
- [3] Y. Tseng, "Voice coil motor apparatus," July 15 2008. US Patent 7,400,068.
- [4] C. Zhao, *Ultrasonic motors: Technologies and applications*. Science Press Beijing and Springer-Verlag Berlin Heidelberg, 2011.
- [5] "<https://www.mathworks.com/products/matlab.html>."
- [6] COMSOL AB, *COMSOL Multiphysics Reference Manual*, November 2013.
- [7] Zemax LLC, Washington, USA, *Zemax 13 Optical Design program*, JUNE 2015.
- [8] PoLight, "<https://www.polight.com/technology-and-products/tlens-compared-to-vcm/default.aspx>," March 2019.
- [9] M. Ye, B. Wang, and S. Sato, "Liquid-crystal lens with a focal length that is variable in a wide range," *Appl. Opt.*, vol. 43, pp. 6407--6412, Dec 2004.
- [10] N. Chronis, G. Liu, K.-H. Jeong, and L. Lee, "Tunable liquid-filled microlens array integrated with microfluidic network," *Opt. Express*, vol. 11, pp. 2370-2378, Sep 2003. [10.1364/OE.11.002370].

- [11] S. Kuiper, B. H. Hendriks, L. J. Huijbregts, A. M. Hirschberg, C. A. Renders, and M. A. van As, "Variable-focus liquid lens for portable applications," *Proc. SPIE*, vol. 5523, pp. 100--109, 2004.
- [12] A. Werber and H. Zappe, "Tunable microfluidic microlenses," *Appl. Opt.*, vol. 44, pp. 3238--3245, Jun 2005.
- [13] K. Haugholt, D. Wang, F. Tyholdt, W. Booiij, and I. Johansen, "Polymer lens," June 12 2012. US Patent 8,199,410.
- [14] K. Tsuchiya, T. Kitagawa, and E. Nakamachi, "Development of rf magnetron sputtering method to fabricate pzt thin film actuator," *Precision Engineering*, vol. 27, no. 3, pp. 258 -- 264, 2003.
- [15] G. Malyavanatham, D. T. O'Brien, M. F. Becker, W. T. Nichols, J. W. Keto, D. Kovar, S. Euphrasie, T. Lou e, and P. Pernod, "Thick films fabricated by laser ablation of pzt microparticles," *Journal of Materials Processing Technology*, vol. 168, no. 2, pp. 273 -- 279, 2005.
- [16] M. Okada, K. Tominaga, T. Araki, S. Katayama, and Y. Sakashita, "Metalorganic chemical vapor deposition of c-axis oriented pzt thin films," *Japanese Journal of Applied Physics*, vol. 29, no. 4R, p. 718, 1990.
- [17] R. W. Schwartz, T. J. Boyle, S. J. Lockwood, M. B. Sinclair, D. Dimos, and C. D. Buchheit, "Sol-gel processing of pzt thin films: A review of the state-of-the-art and process optimization strategies," *Integrated Ferroelectrics*, vol. 7, no. 1-4, pp. 259--277, 1995.
- [18] N. Ledermann, P. Murali, J. Baborowski, S. Gentil, K. Mukati, M. Cantoni, A. Seifert, and N. Setter, "1 0 0-textured, piezoelectric $Pb(Zr_xTi_{1-x})O_3$ thin films for mems: integration, deposition and properties," *Sensors and Actuators A: Physical*, vol. 105, no. 2, pp. 162 -- 170, 2003.

- [19] N. Ledermann, P. Mural, J. Baborowski, M. Forster, and J.-P. Pellaux, "Piezoelectric $Pb(Zr_xTi_{1-x})O_3$ thin film cantilever and bridge acoustic sensors for miniaturized photoacoustic gas detectors," *Journal of Micromechanics and Microengineering*, vol. 14, no. 12, p. 1650, 2004.
- [20] E. Hong, R. Smith, S. Krishnaswamy, C. Freidhoff, and S. Trolier-McKinstry, "Residual stress development in $Pb(Zr,Ti)O_3/ZrO_2/SiO_2$ stacks for piezoelectric microactuators," *Thin Solid Films*, vol. 510, no. 1, pp. 213 -- 221, 2006.
- [21] M. Olfatnia, T. Xu, L. S. Ong, J. M. Miao, and Z. H. Wang, "Investigation of residual stress and its effects on the vibrational characteristics of piezoelectric-based multilayered microdiaphragms," *Journal of Micromechanics and Microengineering*, vol. 20, no. 1, p. 015007, 2010.
- [22] G. A. C. M. Spierings, G. J. M. Dormans, W. G. J. Moors, M. J. E. Ulenaers, and P. K. Larsen, "Stresses in $Pt/Pb(Zr,Ti)O_3/pt$ thin film stacks for integrated ferroelectric capacitors," *Journal of Applied Physics*, vol. 78, no. 3, pp. 1926-1933, 1995.
- [23] S. Corkovic, R. W. Whatmore, and Q. Zhang, "Development of residual stress in sol-gel derived $Pb(Zr,Ti)O_3$ films: An experimental study," *Journal of Applied Physics*, vol. 103, no. 8, p. 084101, 2008.
- [24] M. Rimskog, T. Ebefors, J. Liljeholm, and N. Svedin, "Introducing new materials in a foundry environment with a focus on pzt." <http://www.smart-memphis.eu/publications>, 2015.
- [25] A. Maréchal, *Etude des influences conjuguées des aberrations et de la diffraction sur l'image d'un point*. PhD thesis, Faculté des Sciences des Paris, 1947.

- [26] K. Torabi and A. Azadi, "A new approach to the study of transverse vibrations of a rectangular plate having a circular central hole," *Journal of Solid Mechanics*, vol. 6, no. 2, pp. 135--149, 2014.
- [27] M. K. Kwak and S. Han, "Free vibration analysis of rectangular plate with a hole by means of independent coordinate coupling method," *Journal of Sound and Vibration*, vol. 306, no. 1, pp. 12 -- 30, 2007. [doi:10.1016/j.jsv.2007.05.041].
- [28] G. M. . T. H. A. Olson, Mervyn D. ; Lindberg, "Finite plate-bending elements in polar co-ordinates." NATIONAL AERONAUTICAL ESTABLISHMENT OTTAWA (ONTARIO), OCT 1968.
- [29] G. C. Pardoen, "Asymmetric bending of circular plates using the finite element method," *Computers & Structures*, vol. 5, no. 2, pp. 197 -- 202, 1975.
- [30] M. Deshpande and L. Saggere, "An analytical model and working equations for static deflections of a circular multi-layered diaphragm-type piezoelectric actuator," *Sensors and Actuators A: Physical*, vol. 136, no. 2, pp. 673 -- 689, 2007.
- [31] S. I. E. Lin, "Investigation on packaging parameters of a circular multi-layered diaphragm-type piezoelectric actuator," *Computers and Structures*, vol. 89, no. 3--4, pp. 371 -- 379, 2011.
- [32] E. Tadmor and G. Kosa, "Electromechanical coupling correction for piezoelectric layered beams," *Microelectromechanical Systems, Journal of*, vol. 12, pp. 899--906, Dec 2003.
- [33] M. A. Farghaly, M. N. Akram, and E. Halvorsen, "Optical performance of piezoelectrically actuated mems tunable lenses with various pupil geometries," *Optical Engineering*, vol. 56, no. 3, p. 035104, 2017.

- [34] Z.-B. Kuang, *Theory of Electroelasticity*. Springer-Verlag Berlin Heidelberg, 2014.
- [35] T. Ikeda, *Fundamentals of piezoelectricity*. Oxford University press, New York, 1996.
- [36] O. BÜhler, *A Brief Introduction to Classical, Statistical, and Quantum Mechanics*. Amecian mathematical society, Courant institute of mathematical sciences, 2006.
- [37] J. Mitchell and J. Reddy, "A refined hybrid plate theory for composite laminates with piezoelectric laminae," *International Journal of Solids and Structures*, vol. 32, no. 16, pp. 2345 -- 2367, 1995.
- [38] H. F. Tiersten, "Hamilton's principle for linear piezoelectric media," *Proceedings of the IEEE*, vol. 55, pp. 1523--1524, Aug 1967.
- [39] J. B. Marion and S. T. Thornton, *Classical dynamics of particles and systems*. Cengage Learning India, 2012.
- [40] H. Goldstein, C. poole, and J. Safko, *Classical mechanics*. Addison wesley, 2001.
- [41] O. A. Bauchau, *Flexible Multibody Dynamics*. Springer Science+Business Media, 2011.
- [42] J. N. Reddy, *Mechanics of laminated composite plates and shells: Theory and analysis*. CRC press, 2nd ed., 2004.
- [43] V. Birman, *Plate Structures*, vol. 178 of *Solid Mechanics and its applications*. Springer Science+Bussiness Media, 2011.

- [44] H. F. Tiersten, *Linear Piezoelectric Plate Vibrations: Elements of the Linear Theory of piezoelectricity and the vibration of the piezoelectric plates*. Springer Science Business Media New York, 1969.
- [45] V. N. Mahajan, "Zernike circle polynomials and optical aberrations of systems with circular pupils," *Appl. Opt.*, vol. 33, pp. 8121--8124, Dec 1994.
- [46] B. Boyerinas, C. Mo, and W. W. Clark, "Behavior of unimorph rectangular piezoelectric diaphragm actuators," 2006.
- [47] R. L. Taylor and S. Govindjee, "Solution of clamped rectangular plate problems," *Communications in Numerical Methods in Engineering*, vol. 20, no. 10, pp. 757--765, 2004.
- [48] F. W. J. Olver, D. W. Lozier, R. F. Boisvert, and C. W. Clark, *NIST handbook of mathematical functions*. Cambridge University press, New York, 2010.
- [49] M. A. Farghaly, M. N. Akram, and E. Halvorsen, "Modeling framework for piezoelectrically actuated mems tunable lenses," *Opt. Express*, vol. 24, pp. 28889--28904, Dec 2016.
- [50] T. Bakke, A. Vogl, O. Žero, F. Tyholdt, I.-R. Johansen, and D. Wang, "A novel ultra-planar, long-stroke and low-voltage piezoelectric micromirror," *Journal of Micromechanics and Microengineering*, vol. 20, no. 6, p. 064010, 2010.
- [51] M. A. Farghaly, M. N. Akram, and E. Halvorsen, "Trial functions for reduced-order models of piezoelectrically actuated mems tunable lenses," *To be submitted*, 2018.
- [52] M. A. Farghaly, V. Karatshov, M. N. Akram, and E. Halvorsen, "Electromechanical modeling of piezoelectrically actuated mems tunable lenses with geometric nonlinearity," *To be submitted*.

- [53] G. Singh, G. V. Rao, and N. Iyengar, "Some observations on the large deflection bending of rectangular antisymmetric cross-ply plates," *Composite Structures*, vol. 18, no. 1, pp. 77 -- 91, 1991.

- [54] Norfab, "<https://www.norfab.no/technologies/characterization/usn-mst-lab-2/interferometer-wyko-nt9100/>."

- [55] S. D. Senturia, *Microsystem Design*. Kluwer Academic Press, 2001.

Zernike polynomials

Table A.1: Zernike polynomials Z_n^m .

i	n	m	Z_n^m
0	0	0	1
1	1	1	$r\cos(\theta)$
2	1	-1	$r\sin(\theta)$
3	2	0	$2r^2 - 1$
4	2	2	$r^2\cos(2\theta)$
5	2	-2	$r^2\sin(2\theta)$
6	3	1	$-\cos(\theta)(2r - 3r^3)$
7	3	-1	$-\sin(\theta)(2r - 3r^3)$
8	3	3	$r^3\cos(3\theta)$
9	3	-3	$r^3\sin(3\theta)$
10	4	0	$6r^4 - 6r^2 + 1$
11	4	2	$-\cos(2\theta)(3r^2 - 4r^4)$
12	4	-2	$-\sin(2\theta)(3r^2 - 4r^4)$
13	4	4	$r^4\cos(4\theta)$
14	4	-4	$r^4\sin(4\theta)$
15	5	1	$\cos(\theta)(10r^5 - 12r^3 + 3r)$
16	5	-1	$\sin(\theta)(10r^5 - 12r^3 + 3r)$
17	5	3	$-\cos(3\theta)(4r^3 - 5r^5)$
18	5	-3	$-\sin(3\theta)(4r^3 - 5r^5)$
19	5	5	$r^5\cos(5\theta)$
20	5	-5	$r^5\sin(5\theta)$
21	6	0	$20r^6 - 30r^4 + 12r^2 - 1$
22	6	2	$\cos(2\theta)(15r^6 - 20r^4 + 6r^2)$
23	6	-2	$\sin(2\theta)(15r^6 - 20r^4 + 6r^2)$
24	6	4	$-\cos(4\theta)(5r^4 - 6r^6)$
25	6	-4	$-\sin(4\theta)(5r^4 - 6r^6)$
26	6	6	$r^6\cos(6\theta)$
27	6	-6	$r^6\sin(6\theta)$
28	7	1	$-\cos(\theta)(-35r^7 + 60r^5 - 30r^3 + 4r)$
29	7	-1	$-\sin(\theta)(-35r^7 + 60r^5 - 30r^3 + 4r)$
30	7	3	$\cos(3\theta)(21r^7 - 30r^5 + 10r^3)$
31	7	-3	$\sin(3\theta)(21r^7 - 30r^5 + 10r^3)$
32	7	5	$-\cos(5\theta)(6r^5 - 7r^7)$
33	7	-5	$-\sin(5\theta)(6r^5 - 7r^7)$
34	7	7	$r^7\cos(7\theta)$
35	7	-7	$r^7\sin(7\theta)$
36	8	0	$70r^8 - 140r^6 + 90r^4 - 20r^2 + 1$
37	8	2	$-\cos(2\theta)(-56r^8 + 105r^6 - 60r^4 + 10r^2)$

i	n	m	Z_n^m
38	8	-2	$-\sin(2\theta)(-56r^8 + 105r^6 - 60r^4 + 10r^2)$
39	8	4	$\cos(4\theta)(28r^8 - 42r^6 + 15r^4)$
40	8	-4	$\sin(4\theta)(28r^8 - 42r^6 + 15r^4)$
41	8	6	$-\cos(6\theta)(7r^6 - 8r^8)$
42	8	-6	$-\sin(6\theta)(7r^6 - 8r^8)$
43	8	8	$r^8 \cos(8\theta)$
44	8	-8	$r^8 \sin(8\theta)$
45	9	1	$\cos(\theta)(126r^9 - 280r^7 + 210r^5 - 60r^3 + 5r)$
46	9	-1	$\sin(\theta)(126r^9 - 280r^7 + 210r^5 - 60r^3 + 5r)$
47	9	3	$-\cos(3\theta)(-84r^9 + 168r^7 - 105r^5 + 20r^3)$
48	9	-3	$-\sin(3\theta)(-84r^9 + 168r^7 - 105r^5 + 20r^3)$
49	9	5	$\cos(5\theta)(36r^9 - 56r^7 + 21r^5)$
50	9	-5	$\sin(5\theta)(36r^9 - 56r^7 + 21r^5)$
51	9	7	$-\cos(7\theta)(8r^7 - 9r^9)$
52	9	-7	$-\sin(7\theta)(8r^7 - 9r^9)$
53	9	9	$r^9 \cos(9\theta)$
54	9	-9	$r^9 \sin(9\theta)$
55	10	0	$252r^{10} - 630r^8 + 560r^6 - 210r^4 + 30r^2 - 1$
56	10	2	$\cos(2\theta)(210r^{10} - 504r^8 + 420r^6 - 140r^4 + 15r^2)$
57	10	-2	$\sin(2\theta)(210r^{10} - 504r^8 + 420r^6 - 140r^4 + 15r^2)$
58	10	4	$-\cos(4\theta)(-120r^{10} + 252r^8 - 168r^6 + 35r^4)$
59	10	-4	$-\sin(4\theta)(-120r^{10} + 252r^8 - 168r^6 + 35r^4)$
60	10	6	$\cos(6\theta)(45r^{10} - 72r^8 + 28r^6)$
61	10	-6	$\sin(6\theta)(45r^{10} - 72r^8 + 28r^6)$
62	10	8	$-\cos(8\theta)(9r^8 - 10r^{10})$
63	10	-8	$-\sin(8\theta)(9r^8 - 10r^{10})$
64	10	10	$r^{10} \cos(10\theta)$
65	10	-10	$r^{10} \sin(10\theta)$
66	11	1	$-\cos(\theta)(-462r^{11} + 1260r^9 - 1260r^7 + 560r^5 - 105r^3 + 6r)$
67	11	-1	$-\sin(\theta)(-462r^{11} + 1260r^9 - 1260r^7 + 560r^5 - 105r^3 + 6r)$
68	11	3	$\cos(3\theta)(330r^{11} - 840r^9 + 756r^7 - 280r^5 + 35r^3)$
69	11	-3	$\sin(3\theta)(330r^{11} - 840r^9 + 756r^7 - 280r^5 + 35r^3)$
70	11	5	$-\cos(5\theta)(-165r^{11} + 360r^9 - 252r^7 + 56r^5)$
71	11	-5	$-\sin(5\theta)(-165r^{11} + 360r^9 - 252r^7 + 56r^5)$
72	11	7	$\cos(7\theta)(55r^{11} - 90r^9 + 36r^7)$
73	11	-7	$\sin(7\theta)(55r^{11} - 90r^9 + 36r^7)$
74	11	9	$-\cos(9\theta)(10r^9 - 11r^{11})$
75	11	-9	$-\sin(9\theta)(10r^9 - 11r^{11})$
76	11	11	$r^{11} \cos(11\theta)$

i	n	m	Z_n^m
77	11	-11	$r^{11} \sin(11\theta)$
78	12	0	$924r^{12} - 2772r^{10} + 3150r^8 - 1680r^6 + 420r^4 - 42r^2 + 1$
79	12	2	$-\cos(2\theta)(-792r^{12} + 2310r^{10} - 2520r^8 + 1260r^6 - 280r^4 + 21r^2)$
80	12	-2	$-\sin(2\theta)(-792r^{12} + 2310r^{10} - 2520r^8 + 1260r^6 - 280r^4 + 21r^2)$
81	12	4	$\cos(4\theta)(495r^{12} - 1320r^{10} + 1260r^8 - 504r^6 + 70r^4)$
82	12	-4	$\sin(4\theta)(495r^{12} - 1320r^{10} + 1260r^8 - 504r^6 + 70r^4)$
83	12	6	$-\cos(6\theta)(-220r^{12} + 495r^{10} - 360r^8 + 84r^6)$
84	12	-6	$-\sin(6\theta)(-220r^{12} + 495r^{10} - 360r^8 + 84r^6)$
85	12	8	$\cos(8\theta)(66r^{12} - 110r^{10} + 45r^8)$
86	12	-8	$\sin(8\theta)(66r^{12} - 110r^{10} + 45r^8)$
87	12	10	$-\cos(10\theta)(11r^{10} - 12r^{12})$
88	12	-10	$-\sin(10\theta)(11r^{10} - 12r^{12})$
89	12	12	$r^{12} \cos(12\theta)$
90	12	-12	$r^{12} \sin(12\theta)$
91	13	1	$\cos(\theta)(1716r^{13} - 5544r^{11} + 6930r^9 - 4200r^7 + 1260r^5 - 168r^3 + 7r)$
92	13	-1	$\sin(\theta)(1716r^{13} - 5544r^{11} + 6930r^9 - 4200r^7 + 1260r^5 - 168r^3 + 7r)$
93	13	3	$-\cos(3\theta)(-1287r^{13} + 3960r^{11} - 4620r^9 + 2520r^7 - 630r^5 + 56r^3)$
94	13	-3	$-\sin(3\theta)(-1287r^{13} + 3960r^{11} - 4620r^9 + 2520r^7 - 630r^5 + 56r^3)$
95	13	5	$\cos(5\theta)(715r^{13} - 1980r^{11} + 1980r^9 - 840r^7 + 126r^5)$
96	13	-5	$\sin(5\theta)(715r^{13} - 1980r^{11} + 1980r^9 - 840r^7 + 126r^5)$
97	13	7	$-\cos(7\theta)(-286r^{13} + 660r^{11} - 495r^9 + 120r^7)$
98	13	-7	$-\sin(7\theta)(-286r^{13} + 660r^{11} - 495r^9 + 120r^7)$
99	13	9	$\cos(9\theta)(78r^{13} - 132r^{11} + 55r^9)$
100	13	-9	$\sin(9\theta)(78r^{13} - 132r^{11} + 55r^9)$
101	13	11	$-\cos(11\theta)(12r^{11} - 13r^{13})$
102	13	-11	$-\sin(11\theta)(12r^{11} - 13r^{13})$
103	13	13	$r^{13} \cos(13\theta)$
104	13	-13	$r^{13} \sin(13\theta)$
105	14	0	$3432r^{14} - 12012r^{12} + 16632r^{10} - 11550r^8 + 4200r^6 - 756r^4 + 56r^2 - 1$
106	14	2	$\cos(2\theta)(3003r^{14} - 10296r^{12} + 13860r^{10} - 9240r^8 + 3150r^6 - 504r^4 + 28r^2)$
107	14	-2	$\sin(2\theta)(3003r^{14} - 10296r^{12} + 13860r^{10} - 9240r^8 + 3150r^6 - 504r^4 + 28r^2)$
108	14	4	$-\cos(4\theta)(-2002r^{14} + 6435r^{12} - 7920r^{10} + 4620r^8 - 1260r^6 + 126r^4)$
109	14	-4	$-\sin(4\theta)(-2002r^{14} + 6435r^{12} - 7920r^{10} + 4620r^8 - 1260r^6 + 126r^4)$
110	14	6	$\cos(6\theta)(1001r^{14} - 2860r^{12} + 2970r^{10} - 1320r^8 + 210r^6)$
111	14	-6	$\sin(6\theta)(1001r^{14} - 2860r^{12} + 2970r^{10} - 1320r^8 + 210r^6)$
112	14	8	$-\cos(8\theta)(-364r^{14} + 858r^{12} - 660r^{10} + 165r^8)$
113	14	-8	$-\sin(8\theta)(-364r^{14} + 858r^{12} - 660r^{10} + 165r^8)$
114	14	10	$\cos(10\theta)(91r^{14} - 156r^{12} + 66r^{10})$
115	14	-10	$\sin(10\theta)(91r^{14} - 156r^{12} + 66r^{10})$

i	n	m	Z_n^m
116	14	12	$-\cos(12\theta)(13r^{12} - 14r^{14})$
117	14	-12	$-\sin(12\theta)(13r^{12} - 14r^{14})$
118	14	14	$r^{14}\cos(14\theta)$
119	14	-14	$r^{14}\sin(14\theta)$

Weighted Gegenbauer polynomials

For $N = 5$, the double-indexed weighted Gegenbauer polynomials are

$$\Phi_{00}(X, Y) = (X^2 - 1)^2(Y^2 - 1)^2, \quad (\text{B.1})$$

$$\Phi_{02}(X, Y) = (X^2 - 1)^2(Y^2 - 1)^2(99Y^2/2 - 9/2) \quad (\text{B.2})$$

$$\Phi_{20}(X, Y) = (X^2 - 1)^2(Y^2 - 1)^2(99X^2/2 - 9/2) \quad (\text{B.3})$$

$$\Phi_{22}(X, Y) = (X^2 - 1)^2(Y^2 - 1)^2(99X^2/2 - 9/2)(99Y^2/2 - 9/2) \quad (\text{B.4})$$

$$\Phi_{04}(X, Y) = \frac{33}{8}(X^2 - 1)^2(Y^2 - 1)^2(195Y^4 - 78Y^2 + 3) \quad (\text{B.5})$$

$$\Phi_{40}(X, Y) = \frac{33}{8}(X^2 - 1)^2(Y^2 - 1)^2(195X^4 - 78X^2 + 3) \quad (\text{B.6})$$

$$\Phi_{24}(X, Y) = \frac{297}{16}(X^2 - 1)^2(Y^2 - 1)^2(11X^2 - 1)(195Y^4 - 78Y^2 + 3) \quad (\text{B.7})$$

$$\Phi_{42}(X, Y) = \frac{297}{16}(X^2 - 1)^2(Y^2 - 1)^2(11Y^2 - 1)(195X^4 - 78X^2 + 3) \quad (\text{B.8})$$

$$\Phi_{44}(X, Y) = \frac{1089}{64}(X^2 - 1)^2(Y^2 - 1)^2(195X^4 - 78X^2 + 3)(195Y^4 - 78Y^2 + 3) \quad (\text{B.9})$$

B.1 Mapping weighted Gegenbauer polynomials to Zernike polynomials

$$\begin{aligned}
 \Phi_{00}(r, \theta) = & \left(\frac{3\gamma^8}{640} - \frac{\gamma^6}{16} + \frac{5\gamma^4}{12} - \gamma^2 + 1 \right) Z_0^0 + \frac{\gamma^2}{320} (3\gamma^3 - 36\gamma^4 + 200\gamma^2 - 320) Z_2^0 \\
 & + \frac{\gamma^4}{1344} (9\gamma^4 - 84\gamma^2 + 280) Z_4^0 + \frac{\gamma^4}{672} (-15\gamma^4 + 140\gamma^2 - 168) Z_4^4 \\
 & + \frac{\gamma^6}{1280} (3\gamma^2 - 16) Z_6^0 + \frac{\gamma^6}{384} (-3\gamma^2 + 16) Z_6^4 + \frac{3\gamma^8}{8960} Z_8^0 \\
 & - \frac{\gamma^8}{896} Z_8^4 + \frac{\gamma^8}{128} Z_8^8
 \end{aligned} \tag{B.10}$$

$$\begin{aligned}
 \tilde{\Phi}_{02} = & \left(\frac{99\gamma^{10}}{1024} - \frac{1611\gamma^8}{1280} + \frac{513\gamma^6}{64} - \frac{147\gamma^4}{8} + \frac{135\gamma^2}{8} - \frac{9}{2} \right) Z_0^0 \\
 & + \frac{9\gamma^2}{35840} (825\gamma^8 - 10024\gamma^6 + 57456\gamma^4 - 109760\gamma^2 + 67200) Z_2^0 \\
 & - \frac{99\gamma^2}{17920} (15\gamma^8 - 280\gamma^6 + 3024\gamma^4 - 6720\gamma^2 + 4480) Z_2^2 \\
 & + \frac{3\gamma^4}{14336} (825\gamma^6 - 8592\gamma^4 + 38304\gamma^2 - 43904) Z_4^0 \\
 & - \frac{99\gamma^4}{7168} (5\gamma^6 - 80\gamma^4 + 672\gamma^2 - 896) Z_4^2 \\
 & - \frac{3\gamma^4}{7168} (1155\gamma^6 - 10800\gamma^4 + 14560\gamma^2 - 2688) Z_4^4 \\
 & + \frac{3\gamma^6}{10240} (275\gamma^4 - 2148\gamma^2 + 5472) Z_6^0 \\
 & - \frac{33\gamma^6}{5120} (5\gamma^4 - 60\gamma^2 + 288) Z_6^2 - \frac{3\gamma^6}{1024} (77\gamma^4 - 540\gamma^2 + 416) Z_6^4 \\
 & + \frac{33\gamma^6}{1024} (7\gamma^4 - 84\gamma^2 + 96) Z_6^6 + \frac{9\gamma^8}{71680} (165\gamma^2 - 716) Z_8^0 - \frac{99\gamma^8}{35840} (3\gamma^2 - 20) Z_8^2 \\
 & - \frac{27\gamma^8}{35840} (77\gamma^2 - 300) Z_8^4 + \frac{99\gamma^8}{5120} (3\gamma^2 - 20) Z_8^6 + \frac{9\gamma^8}{5120} (99\gamma^2 - 20) Z_8^8 \\
 & + \frac{33\gamma^{10}}{14336} Z_{10}^0 - \frac{33\gamma^{10}}{35840} Z_{10}^2 - \frac{33\gamma^{10}}{5120} Z_{10}^4 + \frac{33\gamma^{10}}{5120} Z_{10}^6 + \frac{99\gamma^{10}}{5120} Z_{10}^8 - \frac{99\gamma^{10}}{1024} Z_{10}^{10}
 \end{aligned} \tag{B.11}$$

$$\begin{aligned}
 \Phi_{20} = & \left(\frac{99\gamma^{10}}{1024} - \frac{1611\gamma^8}{1280} + \frac{513\gamma^6}{64} - \frac{147\gamma^4}{8} + \frac{135\gamma^2}{8} - \frac{9}{2} \right) Z_0^0 \\
 & + \frac{9\gamma^2}{35840} \left(825\gamma^8 - 10024\gamma^6 + 57456\gamma^4 - 109760\gamma^2 + 67200 \right) Z_2^0 \\
 & + \frac{99\gamma^2}{17920} \left(15\gamma^8 - 280\gamma^6 + 3024\gamma^4 - 6720\gamma^2 + 4480 \right) Z_2^2 \\
 & + \frac{3\gamma^4}{14336} \left(825\gamma^6 - 8592\gamma^4 + 38304\gamma^2 - 43904 \right) Z_4^0 \\
 & + \frac{99\gamma^4}{7168} \left(5\gamma^6 - 80\gamma^4 + 672\gamma^2 - 896 \right) Z_4^2 \\
 & - \frac{3\gamma^4}{7168} \left(1155\gamma^6 - 10800\gamma^4 + 14560\gamma^2 - 2688 \right) Z_4^4 \\
 & + \frac{3\gamma^6}{10240} \left(275\gamma^4 - 2148\gamma^2 + 5472 \right) Z_6^0 \\
 & + \frac{33\gamma^6}{5120} \left(5\gamma^4 - 60\gamma^2 + 288 \right) Z_6^2 - \frac{3\gamma^6}{1024} \left(77\gamma^4 - 540\gamma^2 + 416 \right) Z_6^4 \\
 & - \frac{33\gamma^6}{1024} \left(7\gamma^4 - 84\gamma^2 + 96 \right) Z_6^6 + \frac{9\gamma^8}{71680} \left(165\gamma^2 - 716 \right) Z_8^0 + \frac{99\gamma^8}{35840} \left(3\gamma^2 - 20 \right) Z_8^2 \\
 & - \frac{27\gamma^8}{35840} \left(77\gamma^2 - 300 \right) Z_8^4 + \frac{99\gamma^8}{5120} \left(3\gamma^2 - 20 \right) Z_8^6 + \frac{9\gamma^8}{5120} \left(99\gamma^2 - 20 \right) Z_8^8 \\
 & + \frac{33\gamma^{10}}{14336} Z_{10}^0 + \frac{33\gamma^{10}}{35840} Z_{10}^2 - \frac{33\gamma^{10}}{5120} Z_{10}^4 - \frac{33\gamma^{10}}{5120} Z_{10}^6 + \frac{99\gamma^{10}}{5120} Z_{10}^8 - \frac{99\gamma^{10}}{1024} Z_{10}^{10}
 \end{aligned} \tag{B.12}$$

$$\begin{aligned}
 \Phi_{22} = & \left(\frac{49005\gamma^{12}}{28672} - \frac{20493\gamma^{10}}{1024} + \frac{244377\gamma^8}{2560} - \frac{14337\gamma^6}{64} + \frac{8289\gamma^4}{32} - \frac{1053\gamma^2}{8} + \frac{81}{4} \right) Z_0^0 \\
 & + \frac{81\gamma^2}{573440} \left(27225\gamma^{10} - 303600\gamma^8 + 1351616\gamma^6 - 2854656\gamma^4 + 2750720\gamma^2 - 931840 \right) Z_2^0 \\
 & + \frac{27\gamma^4}{114688} \left(15125\gamma^8 - 151800\gamma^6 + 579264\gamma^4 - 951552\gamma^2 + 550144 \right) Z_4^0 \\
 & - \frac{27\gamma^4}{57344} \left(21175\gamma^8 - 212520\gamma^6 + 782400\gamma^4 - 1191680\gamma^2 + 661248 \right) Z_4^4 \\
 & + \frac{27\gamma^6}{40960} \left(3025\gamma^6 - 25300\gamma^4 + 72408\gamma^2 - 67968 \right) Z_6^0 - \frac{27\gamma^6}{4096} \left(847\gamma^6 - 7084\gamma^4 + 19560\gamma^2 - 17024 \right) Z_6^4 \\
 & + \frac{81\gamma^8}{286720} \left(2475\gamma^4 - 15180\gamma^2 + 24136 \right) Z_8^0 - \frac{81\gamma^8}{143360} \left(3465\gamma^4 - 21252\gamma^2 + 32600 \right) Z_8^4 \\
 & + \frac{729\gamma^8}{20480} \left(165\gamma^4 - 1012\gamma^2 + 1080 \right) Z_8^8 + \frac{297\gamma^{10}}{14688} \left(55\gamma^2 - 184 \right) Z_{10}^0 - \frac{297\gamma^{10}}{40960} \left(55\gamma^2 - 184 \right) Z_{10}^4 \\
 & + \frac{891\gamma^{10}}{40960} \left(55\gamma^2 - 184 \right) Z_{10}^8 + \frac{1485\gamma^{12}}{114688} Z_{12}^0 - \frac{297\gamma^{12}}{8192} Z_{12}^4 + \frac{891\gamma^{12}}{8192} Z_{12}^8 - \frac{9801\gamma^{12}}{8192} Z_{12}^{12}
 \end{aligned} \tag{B.13}$$

$$\begin{aligned}
 \bar{\Phi}_{04} = & \left(\frac{6435\gamma^{12}}{8192} - \frac{22737\gamma^{10}}{2048} + \frac{414711\gamma^8}{5120} - \frac{25839\gamma^6}{128} + \frac{13629\gamma^4}{64} - \frac{1485\gamma^2}{16} + \frac{99}{8} \right) Z_0^0 \\
 & + \frac{99\gamma^2}{1146880} \left(20475\gamma^{10} - 275600\gamma^8 + 1876672\gamma^6 - 4209408\gamma^4 + 3700480\gamma^2 - 1075200 \right) Z_2^0 \\
 & - \frac{1287\gamma^2}{573440} \left(525\gamma^{10} - 9840\gamma^8 + 105280\gamma^6 - 263424\gamma^4 + 241920\gamma^2 - 71680 \right) Z_2^2 \\
 & + \frac{33\gamma^4}{229376} \left(11375\gamma^8 - 137800\gamma^6 + 804288\gamma^4 - 1403136\gamma^2 + 740096 \right) Z_4^0 \\
 & - \frac{143\gamma^4}{114688} \left(875\gamma^8 - 14760\gamma^6 + 135360\gamma^4 - 263424\gamma^2 + 145152 \right) Z_4^2 \\
 & + \frac{11\gamma^4}{114688} \left(-38675\gamma^8 + 360360\gamma^6 + 72000\gamma^4 - 1370880\gamma^2 + 1016064 \right) Z_4^4 \\
 & + \frac{11\gamma^6}{81920} \left(6825\gamma^6 - 68900\gamma^4 + 301608\gamma^2 - 300672 \right) Z_6^0 - \frac{143\gamma^6}{40960} \left(175\gamma^6 - 2460\gamma^4 + 16920\gamma^2 - 18816 \right) Z_6^2 \\
 & + \frac{11\gamma^6}{8192} \left(-1547\gamma^6 + 12012\gamma^4 + 1800\gamma^2 - 19584 \right) Z_6^4 + \frac{143\gamma^6}{8192} \left(189\gamma^6 - 2324\gamma^4 + 3528\gamma^2 - 1152 \right) Z_6^6 \\
 & + \frac{9\gamma^8}{573440} \left(20475\gamma^4 - 151580\gamma^2 + 368632 \right) Z_8^0 - \frac{117\gamma^8}{286720} \left(525\gamma^4 - 5412\gamma^2 + 20680 \right) Z_8^2 \\
 & + \frac{9\gamma^8}{286720} \left(-23205\gamma^4 + 132132\gamma^2 + 11000 \right) Z_8^4 + \frac{117\gamma^8}{40960} \left(405\gamma^4 - 3652\gamma^2 + 3080 \right) Z_8^6 \\
 & + \frac{27\gamma^8}{40960} \left(975\gamma^4 + 15444\gamma^2 - 18920 \right) Z_8^8 + \frac{143\gamma^{10}}{229376} \left(105\gamma^2 - 424 \right) Z_{10}^0 - \frac{143\gamma^{10}}{573440} \left(175\gamma^2 - 984 \right) Z_{10}^2 \\
 & - \frac{143\gamma^{10}}{81920} \left(85\gamma^2 - 264 \right) Z_{10}^4 + \frac{143\gamma^{10}}{81920} \left(135\gamma^2 - 664 \right) Z_{10}^6 + \frac{429\gamma^{10}}{81920} \left(25\gamma^2 + 216 \right) Z_{10}^8 - \frac{429\gamma^{10}}{16384} \left(55\gamma^2 - 24 \right) Z_{10}^{10} \\
 & + \frac{195\gamma^{12}}{32768} Z_{12}^0 - \frac{65\gamma^{12}}{16384} Z_{12}^2 - \frac{221\gamma^{12}}{16384} Z_{12}^4 + \frac{351\gamma^{12}}{16384} Z_{12}^6 + \frac{195\gamma^{12}}{16384} Z_{12}^8 - \frac{2145\gamma^{12}}{16384} Z_{12}^{10} + \frac{6435\gamma^{12}}{16384} Z_{12}^{12} \quad (\text{B.14})
 \end{aligned}$$

$$\begin{aligned}
 \bar{\Phi}_{40} = & \left(\frac{6435\gamma^{12}}{8192} - \frac{22737\gamma^{10}}{2048} + \frac{414711\gamma^8}{5120} - \frac{25839\gamma^6}{128} + \frac{13629\gamma^4}{64} - \frac{1485\gamma^2}{16} + \frac{99}{8} \right) Z_0^0 \\
 & + \frac{99\gamma^2}{1146880} \left(20475\gamma^{10} - 275600\gamma^8 + 1876672\gamma^6 - 4209408\gamma^4 + 3700480\gamma^2 - 1075200 \right) Z_2^0 \\
 & + \frac{1287\gamma^2}{573440} \left(525\gamma^{10} - 9840\gamma^8 + 105280\gamma^6 - 263424\gamma^4 + 241920\gamma^2 - 71680 \right) Z_2^2 \\
 & + \frac{33\gamma^4}{229376} \left(11375\gamma^8 - 137800\gamma^6 + 804288\gamma^4 - 1403136\gamma^2 + 740096 \right) Z_4^0 \\
 & + \frac{143\gamma^4}{114688} \left(875\gamma^8 - 14760\gamma^6 + 135360\gamma^4 - 263424\gamma^2 + 145152 \right) Z_4^2 \\
 & + \frac{11\gamma^4}{114688} \left(-38675\gamma^8 + 360360\gamma^6 + 72000\gamma^4 - 1370880\gamma^2 + 1016064 \right) Z_4^4 \\
 & + \frac{11\gamma^6}{81920} \left(6825\gamma^6 - 68900\gamma^4 + 301608\gamma^2 - 300672 \right) Z_6^0 + \frac{143\gamma^6}{40960} \left(175\gamma^6 - 2460\gamma^4 + 16920\gamma^2 - 18816 \right) Z_6^2 \\
 & + \frac{11\gamma^6}{8192} \left(-1547\gamma^6 + 12012\gamma^4 + 1800\gamma^2 - 19584 \right) Z_6^4 - \frac{143\gamma^6}{8192} \left(189\gamma^6 - 2324\gamma^4 + 3528\gamma^2 - 1152 \right) Z_6^6 \\
 & + \frac{9\gamma^8}{573440} \left(20475\gamma^4 - 151580\gamma^2 + 368632 \right) Z_8^0 + \frac{117\gamma^8}{286720} \left(525\gamma^4 - 5412\gamma^2 + 20680 \right) Z_8^2 \\
 & + \frac{9\gamma^8}{286720} \left(-23205\gamma^4 + 132132\gamma^2 + 11000 \right) Z_8^4 - \frac{117\gamma^8}{40960} \left(405\gamma^4 - 3652\gamma^2 + 3080 \right) Z_8^6 \\
 & + \frac{27\gamma^8}{40960} \left(975\gamma^4 + 15444\gamma^2 - 18920 \right) Z_8^8 + \frac{143\gamma^{10}}{229376} \left(105\gamma^2 - 424 \right) Z_{10}^0 + \frac{143\gamma^{10}}{573440} \left(175\gamma^2 - 984 \right) Z_{10}^2 \\
 & - \frac{143\gamma^{10}}{81920} \left(85\gamma^2 - 264 \right) Z_{10}^4 - \frac{143\gamma^{10}}{81920} \left(135\gamma^2 - 664 \right) Z_{10}^6 + \frac{429\gamma^{10}}{81920} \left(25\gamma^2 + 216 \right) Z_{10}^8 - \frac{429\gamma^{10}}{16384} \left(55\gamma^2 - 24 \right) Z_{10}^{10} \\
 & + \frac{195\gamma^{12}}{32768} Z_{12}^0 + \frac{65\gamma^{12}}{16384} Z_{12}^2 - \frac{221\gamma^{12}}{16384} Z_{12}^4 - \frac{351\gamma^{12}}{16384} Z_{12}^6 + \frac{195\gamma^{12}}{16384} Z_{12}^8 + \frac{2145\gamma^{12}}{16384} Z_{12}^{10} + \frac{6435\gamma^{12}}{16384} Z_{12}^{12} \quad (\text{B.15})
 \end{aligned}$$

$$\begin{aligned}
 \bar{\Phi}_{24} = & \left(\frac{3185325\gamma^{14}}{262144} - \frac{16969095\gamma^{12}}{114688} + \frac{6110181\gamma^{10}}{8192} - \frac{19688427\gamma^8}{10240} + \frac{2684583\gamma^6}{1024} - \frac{233739\gamma^4}{128} + \frac{36531\gamma^2}{64} - \frac{891}{16} \right) Z_0^0 \\
 & + \frac{297\gamma^2}{9175040} \left(875875\gamma^{12} - 10284300\gamma^{10} + 49375200\gamma^8 - 118793472\gamma^6 + 145780992\gamma^4 \right. \\
 & \left. - 84618240\gamma^2 + 17633280 \right) Z_2^0 \\
 & - \frac{297\gamma^2}{917504} \left(25025\gamma^{12} - 376740\gamma^{10} + 2363040\gamma^8 - 7069440\gamma^6 + 9886464\gamma^4 - 6128640\gamma^2 + 1290240 \right) Z_2^2 \\
 & + \frac{297\gamma^4}{1835008} \left(175175\gamma^{10} - 1904500\gamma^8 + 8229200\gamma^6 - 16970496\gamma^4 + 16197888\gamma^2 - 5641216 \right) Z_4^0 \\
 & - \frac{495\gamma^4}{917504} \left(15015\gamma^{10} - 209300\gamma^8 + 1181520\gamma^6 - 3029760\gamma^4 + 3295488\gamma^2 - 1225728 \right) Z_4^2 \\
 & - \frac{99\gamma^4}{917504} \left(675675\gamma^{10} - 7161700\gamma^8 + 28884240\gamma^6 - 52934400\gamma^4 + 45077760\gamma^2 - 14386176 \right) Z_4^4 \\
 & + \frac{99\gamma^6}{1310720} \left(238875\gamma^8 - 2285400\gamma^6 + 8229200\gamma^4 - 12727872\gamma^2 + 6941952 \right) Z_6^0 \\
 & - \frac{99\gamma^6}{131072} \left(6825\gamma^8 - 83720\gamma^6 + 393840\gamma^4 - 757440\gamma^2 + 470784 \right) Z_6^2 \\
 & - \frac{99\gamma^6}{131072} \left(61425\gamma^8 - 572936\gamma^6 + 1925616\gamma^4 - 2646720\gamma^2 + 1287936 \right) Z_6^4 \\
 & + \frac{99\gamma^6}{131072} \left(36855\gamma^8 - 452088\gamma^6 + 1999760\gamma^4 - 3205440\gamma^2 + 1716480 \right) Z_6^6 \\
 & + \frac{81\gamma^8}{9175040} \left(875875\gamma^6 - 6856200\gamma^4 + 18104240\gamma^2 - 15556288 \right) Z_8^0 \\
 & - \frac{81\gamma^8}{917504} \left(25025\gamma^6 - 251160\gamma^4 + 866448\gamma^2 - 925760 \right) Z_8^2 \\
 & - \frac{81\gamma^8}{4587520} \left(1126125\gamma^6 - 8594040\gamma^4 + 21181776\gamma^2 - 16174400 \right) Z_8^4 \\
 & + \frac{81\gamma^8}{131072} \left(19305\gamma^6 - 193752\gamma^4 + 628496\gamma^2 - 559680 \right) Z_8^6 \\
 & + \frac{81\gamma^8}{655360} \left(353925\gamma^6 - 2391480\gamma^4 + 3723984\gamma^2 - 1559360 \right) Z_8^8 + \frac{99\gamma^{10}}{1835008} \left(40425\gamma^4 - 228540\gamma^2 + 329168 \right) Z_{10}^0 \\
 & - \frac{99\gamma^{10}}{917504} \left(5775\gamma^4 - 41860\gamma^2 + 78768 \right) Z_{10}^2 - \frac{99\gamma^{10}}{655360} \left(37125\gamma^4 - 204620\gamma^2 + 275088 \right) Z_{10}^4 \\
 & + \frac{99\gamma^{10}}{131072} \left(4455\gamma^4 - 32292\gamma^2 + 57136 \right) Z_{10}^6 + \frac{297\gamma^{10}}{655360} \left(27225\gamma^4 - 132860\gamma^2 + 112848 \right) Z_{10}^8 \\
 & - \frac{1485\gamma^{10}}{131072} \left(1815\gamma^4 - 13156\gamma^2 + 13872 \right) Z_{10}^{10} + \frac{1755\gamma^{12}}{1835008} \left(385\gamma^2 - 1172 \right) Z_{12}^0 - \frac{585\gamma^{12}}{917504} \left(165\gamma^2 - 644 \right) Z_{12}^2 \\
 & - \frac{117\gamma^{12}}{917504} \left(7425\gamma^2 - 22036 \right) Z_{12}^4 + \frac{3159\gamma^{12}}{917504} \left(165\gamma^2 - 644 \right) Z_{12}^6 + \frac{351\gamma^{12}}{917504} \left(5445\gamma^2 - 14308 \right) Z_{12}^8 \\
 & - \frac{19305\gamma^{12}}{917504} \left(165\gamma^2 - 644 \right) Z_{12}^{10} - \frac{11583\gamma^{12}}{917504} \left(715\gamma^2 - 476 \right) Z_{12}^{12} + \frac{7425\gamma^{14}}{262144} Z_{14}^0 - \frac{7425\gamma^{14}}{917504} Z_{14}^2 - \frac{66825\gamma^{14}}{917504} Z_{14}^4 \\
 & + \frac{40095\gamma^{14}}{917504} Z_{14}^6 + \frac{147015\gamma^{14}}{917504} Z_{14}^8 - \frac{245025\gamma^{14}}{917504} Z_{14}^{10} - \frac{637065\gamma^{14}}{917504} Z_{14}^{12} + \frac{637065\gamma^{14}}{131072} Z_{14}^{14} \quad (\text{B.16})
 \end{aligned}$$

$$\begin{aligned}
 \bar{\Phi}_{42} = & \left(\frac{3185325\gamma^{14}}{262144} - \frac{16969095\gamma^{12}}{114688} + \frac{6110181\gamma^{10}}{8192} - \frac{19688427\gamma^8}{10240} + \frac{2684583\gamma^6}{1024} - \frac{233739\gamma^4}{128} + \frac{36531\gamma^2}{64} - \frac{891}{16} \right) Z_0^0 \\
 & + \frac{297\gamma^2}{9175040} \left(875875\gamma^{12} - 10284300\gamma^{10} + 49375200\gamma^8 - 118793472\gamma^6 + 145780992\gamma^4 \right. \\
 & \left. - 84618240\gamma^2 + 17633280 \right) Z_2^0 \\
 & + \frac{297\gamma^2}{917504} \left(25025\gamma^{12} - 376740\gamma^{10} + 2363040\gamma^8 - 7069440\gamma^6 + 9886464\gamma^4 - 6128640\gamma^2 + 1290240 \right) Z_2^2 \\
 & + \frac{297\gamma^4}{1835008} \left(175175\gamma^{10} - 1904500\gamma^8 + 8229200\gamma^6 - 16970496\gamma^4 + 16197888\gamma^2 - 5641216 \right) Z_4^0 \\
 & + \frac{495\gamma^4}{917504} \left(15015\gamma^{10} - 209300\gamma^8 + 1181520\gamma^6 - 3029760\gamma^4 + 3295488\gamma^2 - 1225728 \right) Z_4^2 \\
 & - \frac{99\gamma^4}{917504} \left(675675\gamma^{10} - 7161700\gamma^8 + 28884240\gamma^6 - 52934400\gamma^4 + 45077760\gamma^2 - 14386176 \right) Z_4^4 \\
 & + \frac{99\gamma^6}{1310720} \left(238875\gamma^8 - 2285400\gamma^6 + 8229200\gamma^4 - 12727872\gamma^2 + 6941952 \right) Z_6^0 \\
 & + \frac{99\gamma^6}{131072} \left(6825\gamma^8 - 83720\gamma^6 + 393840\gamma^4 - 757440\gamma^2 + 470784 \right) Z_6^2 \\
 & - \frac{99\gamma^6}{131072} \left(61425\gamma^8 - 572936\gamma^6 + 1925616\gamma^4 - 2646720\gamma^2 + 1287936 \right) Z_6^4 \\
 & - \frac{99\gamma^6}{131072} \left(36855\gamma^8 - 452088\gamma^6 + 1999760\gamma^4 - 3205440\gamma^2 + 1716480 \right) Z_6^6 \\
 & + \frac{81\gamma^8}{9175040} \left(875875\gamma^6 - 6856200\gamma^4 + 18104240\gamma^2 - 15556288 \right) Z_8^0 \\
 & + \frac{81\gamma^8}{917504} \left(25025\gamma^6 - 251160\gamma^4 + 866448\gamma^2 - 925760 \right) Z_8^2 \\
 & - \frac{81\gamma^8}{4587520} \left(1126125\gamma^6 - 8594040\gamma^4 + 21181776\gamma^2 - 16174400 \right) Z_8^4 \\
 & - \frac{81\gamma^8}{131072} \left(19305\gamma^6 - 193752\gamma^4 + 628496\gamma^2 - 559680 \right) Z_8^6 \\
 & + \frac{81\gamma^8}{655360} \left(353925\gamma^6 - 2391480\gamma^4 + 3723984\gamma^2 - 1559360 \right) Z_8^8 + \frac{99\gamma^{10}}{1835008} \left(40425\gamma^4 - 228540\gamma^2 + 329168 \right) Z_{10}^0 \\
 & + \frac{99\gamma^{10}}{917504} \left(5775\gamma^4 - 41860\gamma^2 + 78768 \right) Z_{10}^2 - \frac{99\gamma^{10}}{655360} \left(37125\gamma^4 - 204620\gamma^2 + 275088 \right) Z_{10}^4 \\
 & - \frac{99\gamma^{10}}{131072} \left(4455\gamma^4 - 32292\gamma^2 + 57136 \right) Z_{10}^6 + \frac{297\gamma^{10}}{655360} \left(27225\gamma^4 - 132860\gamma^2 + 112848 \right) Z_{10}^8 \\
 & + \frac{1485\gamma^{10}}{131072} \left(1815\gamma^4 - 13156\gamma^2 + 13872 \right) Z_{10}^{10} + \frac{1755\gamma^{12}}{1835008} \left(385\gamma^2 - 1172 \right) Z_{12}^0 + \frac{585\gamma^{12}}{917504} \left(165\gamma^2 - 644 \right) Z_{12}^2 \\
 & - \frac{117\gamma^{12}}{917504} \left(7425\gamma^2 - 22036 \right) Z_{12}^4 - \frac{3159\gamma^{12}}{917504} \left(165\gamma^2 - 644 \right) Z_{12}^6 + \frac{351\gamma^{12}}{917504} \left(5445\gamma^2 - 14308 \right) Z_{12}^8 \\
 & + \frac{19305\gamma^{12}}{917504} \left(165\gamma^2 - 644 \right) Z_{12}^{10} - \frac{11583\gamma^{12}}{917504} \left(715\gamma^2 - 476 \right) Z_{12}^{12} + \frac{7425\gamma^{14}}{262144} Z_{14}^0 + \frac{7425\gamma^{14}}{917504} Z_{14}^2 - \frac{66825\gamma^{14}}{917504} Z_{14}^4 \\
 & - \frac{40095\gamma^{14}}{917504} Z_{14}^6 + \frac{147015\gamma^{14}}{917504} Z_{14}^8 + \frac{245025\gamma^{14}}{917504} Z_{14}^{10} - \frac{637065\gamma^{14}}{917504} Z_{14}^{12} - \frac{637065\gamma^{14}}{131072} Z_{14}^{14} \quad (\text{B.17})
 \end{aligned}$$

$$\begin{aligned}
 \bar{\Phi}_{44} = & \left(\frac{161035875\gamma^{16}}{2097152} - \frac{124227675\gamma^{14}}{131072} + \frac{561254265\gamma^{12}}{114688} - \frac{55509597\gamma^{10}}{4096} + \frac{441054801\gamma^8}{20480} - \frac{10006821\gamma^6}{512} \right. \\
 & + \frac{1218591\gamma^4}{128} - \frac{68607\gamma^2}{32} + \frac{9801}{64} \Big) Z_0^0 \\
 & + \frac{3267\gamma^2}{18350080} \left(1035125\gamma^{14} - 12421500\gamma^{12} + 61846200\gamma^{10} - 163113600\gamma^8 + 241925376\gamma^6 - 197600256\gamma^4 + \right. \\
 & \left. 80209920\gamma^2 - 12042240 \right) Z_2^0 \\
 & + \frac{99\gamma^4}{3670016} \left(7245875\gamma^{12} - 81981900\gamma^{10} + 377949000\gamma^8 - 897124800\gamma^6 + 1140505344\gamma^4 \right. \\
 & \left. - 724534272\gamma^2 + 176461824 \right) Z_4^0 \\
 & - \frac{99\gamma^4}{1835008} \left(9316125\gamma^{12} - 105405300\gamma^{10} + 481881400\gamma^8 - 1121440320\gamma^6 + 1378080000\gamma^4 - 838548480\gamma^2 \right. \\
 & \left. + 194439168 \right) Z_4^4 \\
 & + \frac{99\gamma^6}{5242880} \left(7245875\gamma^{10} - 74529000\gamma^8 + 302359200\gamma^6 - 598083200\gamma^4 + 570252672\gamma^2 - 207009792 \right) Z_6^0 \\
 & - \frac{99\gamma^6}{524288} \left(1863225\gamma^{10} - 19164600\gamma^8 + 77101024\gamma^6 - 149525376\gamma^4 + 137808000\gamma^2 - 47917056 \right) Z_6^4 \\
 & + \frac{891\gamma^8}{36700160} \left(2786875\gamma^8 - 24843000\gamma^6 + 82461600\gamma^4 - 119616640\gamma^2 + 63361408 \right) Z_8^0 \\
 & - \frac{2673\gamma^8}{18350080} \left(1194375\gamma^8 - 10647000\gamma^6 + 35045920\gamma^4 - 49841792\gamma^2 + 25520000 \right) Z_8^4 \\
 & + \frac{891\gamma^8}{2621440} \left(1126125\gamma^8 - 10038600\gamma^6 + 31805280\gamma^4 - 41019264\gamma^2 + 18719360 \right) Z_8^8 \\
 & + \frac{14157\gamma^{10}}{3670016} \left(6125\gamma^6 - 44100\gamma^4 + 105720\gamma^2 - 83648 \right) Z_{10}^0 \\
 & - \frac{14157\gamma^{10}}{1310720} \left(5625\gamma^6 - 40500\gamma^4 + 96280\gamma^2 - 74688 \right) Z_{10}^4 \\
 & + \frac{42471\gamma^{10}}{1310720} \left(4125\gamma^6 - 29700\gamma^4 + 67960\gamma^2 - 47808 \right) Z_{10}^8 + \frac{6435\gamma^{12}}{3670016} \left(3185\gamma^4 - 16380\gamma^2 + 21144 \right) Z_{12}^0 \\
 & - \frac{1287\gamma^{12}}{1835008} \left(20475\gamma^4 - 105300\gamma^2 + 134792 \right) Z_{12}^4 + \frac{3861\gamma^{12}}{1835008} \left(15015\gamma^4 - 77220\gamma^2 + 95144 \right) Z_{12}^8 \\
 & - \frac{42471\gamma^{12}}{1835008} \left(5915\gamma^4 - 30420\gamma^2 + 29064 \right) Z_{12}^{12} + \frac{96525\gamma^{14}}{4194304} \left(35\gamma^2 - 96 \right) Z_{14}^0 - \frac{868725\gamma^{14}}{14680064} \left(35\gamma^2 - 96 \right) Z_{14}^4 \\
 & + \frac{1911195\gamma^{14}}{14680064} \left(35\gamma^2 - 96 \right) Z_{14}^8 - \frac{8281845\gamma^{14}}{14680064} \left(35\gamma^2 - 96 \right) Z_{14}^{12} + \frac{225225\gamma^{16}}{4194304} Z_{16}^0 - \frac{289575\gamma^{16}}{2097152} Z_{16}^4 \\
 & + \frac{637065\gamma^{16}}{2097152} Z_{16}^8 - \frac{2760615\gamma^{16}}{2097152} Z_{16}^{12} + \frac{41409225\gamma^{16}}{2097152} Z_{16}^{16}
 \end{aligned} \tag{B.18}$$

Dynamic Analysis

The variational integral of the equivalent mass is

$$M_{\square}(\dot{w}_0, \delta \dot{w}_0; \mathbf{I}_0) = \int_{-1}^1 \int_{-1}^1 \left\{ \left((a/2)^2 I_0 \dot{w}_0 \delta \dot{w}_0 + I_2 (\dot{w}_{0,X} \delta \dot{w}_{0,X} + \dot{w}_{0,Y} \delta \dot{w}_{0,Y}) \right) \right\} dX dY. \quad (C.1)$$

The state space representation of the system above can be written as [55]

$$\dot{\mathbf{x}} = \mathbf{A}\mathbf{x} + \mathbf{B}\mathbf{u} \quad (C.2)$$

$$\mathbf{y} = \mathbf{C}\mathbf{x} + \mathbf{D}\mathbf{u} \quad (C.3)$$

where

$$\mathbf{A} = \begin{bmatrix} \mathbf{0}_{N_G \times N_G} & \mathbf{I}_{N_G \times N_G} \\ -M_{k_1 k_2}^{-1} R_{k_1 k_2} & -M_{k_1 k_2}^{-1} \zeta_{k_1 k_2} \end{bmatrix} \quad (C.4)$$

$$\mathbf{B} = \begin{bmatrix} \mathbf{0}_{N_G \times 1} \\ M_{k_1 k_2}^{-1} F_{k_2} \end{bmatrix} \quad (C.5)$$

$$\mathbf{C} = \mathbf{I}_{2N_G \times 2N_G} \quad (C.6)$$

$$\mathbf{D} = \mathbf{0}_{2N_G \times 1} \quad (C.7)$$

Article 1

Mahmoud A. Farghaly, Muhammad Nadeem Akram, and Einar Halvorsen, "Modeling framework for piezoelectrically actuated MEMS tunable lenses," Opt. Express 24, 28889-28904 (2016).

Article 2

Mahmoud A. Farghaly, Muhammad Nadeem Akram, Einar Halvorsen, "Optical performance of piezoelectrically actuated MEMS tunable lenses with various pupil geometries," *Optical Engineering* 56(3), 035104 (21 March 2017).

Article 3

Mahmoud A. Farghaly, Ulrik Hanke, Muhammad Nadeem Akram, Einar Halvorsen, "Trial functions for reduced-order models of piezoelectrically actuated microelectromechanical systems tunable lenses," *Optical Engineering* 57(9), 095103 (24 September 2018).

Article 4

Mahmoud A. Farghaly, Vladimir Kartashov, Muhammad Nadeem Akram, Einar Halvorsen, "Electromechanical modeling of piezoelectrically actuated MEMS tunable lenses with geometric nonlinearity".

Doctoral dissertation no. 76
2020

—
**Modeling and design of
piezoelectrically actuated MEMS tunable lenses**
—

Mahmoud Ahmed Farghaly Abdelmeguid
—

ISBN 978-82-7860-447-2 (print)
ISBN 978-82-7860-443-4 (online)

usn.no

